Dissertation

Digital Predistortion for High Throughput Satellites: Architectures, Applications and Performance

Ovais Bin Usman

der Bundeswehr Universität München

Faculty of Electrical Engineering and Information Technology
Institute of Information Technology
Chair of Signal Processing

1. Supervisor and first reviewer:	Professor Dr.-Ing. Andreas Knopp, MBA
2. Second reviewer:	Professor Dr. techn. Dr. h.c. Josef A. Nossek

UNIVERSITÄT DER BUNDESWEHR MÜNCHEN

Digital Predistortion for High Throughput Satellites: Architectures, Applications and Performance

Ovais Bin Usman

Vollständiger Abdruck der von der Fakultät für Elektrotechnik und Informationstechnik der Universität der Bundeswehr München zur Erlangung des akademischen Grades eines

Doktor-Ingenieurs

genehmigten Dissertation.

Promotionsausschuss

Vorsitzender:	
1. Prüfer:	Universitätsprofessor Dr.-Ing. Andreas Knopp, MBA
2. Prüfer:	Universitätsprofessor Dr. techn. Dr. h.c. Josef A. Nossek

Die Dissertation wurde am 04.03.2021 bei der Universität der Bundeswehr München eingereicht und durch die Fakultät fur Elektrotechnik und Informationstechnik am 22.09.2021 angenommen. Die mundliche Prüfung fand am 27.10.2021 statt.

Abstract

The future fleets of high throughput satellites (HTS) aim to support a diverse set of applications ranging from "connecting the unconnected" to "video on demand" at ultra-high data rates. However, achieving such ultra-high data rates has pushed for the need of more flexible and efficient payloads. Bandwidth and power efficient transponders require a multicarrier signal excitation of the on-board high power amplifiers (HPAs), and an operating point closer to saturation. However, this leads to severe linear and non-linear distortions due to the increased inter-carrier-interference (ICI) and intermodulation (IMD) noise, resulting in an overall degradation of system performance. The analog linearizers built into the channel amplifiers of the on-board HPAs offer only limited gain and are non-adaptive. In addition, the latest digital video broadcasting (DVB-S2X) standard is pushing for uplink signals with bandwidths that are more or less equal to that of transponder's input multiplexer (IMUX) and output multiplexer (OMUX). This introduces severe linear and non-linear distortions, especially for the carriers at the edges. Equalizers are proposed at the receiver terminal to compensate for the aforementioned distortions, but they increase the complexity of the receiver significantly. Due to the recent advancements in on-board processors (OBPs), the distortions caused by the HPAs and transponder filters can be mitigated on-board the satellite by employing linearization techniques such as digital predistortion (DPD) while maintaining a high degree of power and bandwidth efficiency. Therefore, this work focuses on the on-board predistortion methods and proposes the "**on-board, adaptive, bandlimited, signal, memory polynomial**"-based DPD as the best suited predistortion method for HTS. Bandlimited DPD allows for the use of low sampling rate converters in OBPs resulting in low power consumption. This work presents a novel iterative direct learning architecture (DLA)-based bandlimited memory polynomial (MP) DPD, and compares its performance against a state-of-the-art in-direct learning architecture (IDLA)-based bandlimited MP DPD. The novel DLA-based DPD approach outperforms the IDLA-based DPD, especially under severe bandlimitation constraints. More importantly, using the proposed DPD methods, this thesis also presents the results of a thorough investigation made to identify the system parameters which should be optimized for the best DPD performance. In addition, the presented system parameter identification analysis also highlights the scenarios where it is feasible to implement DPD. Lastly, the thesis also discusses and presents the gains of implementing the proposed novel DLA-based DPD in multiport amplifiers (MPA) and 5G waveforms.

Supervisor: Professor Dr.-Ing. Andreas Knopp, MBA

Kurzfassung

Zukünftige High-Throughput-Satelliten (HTS) Systeme zielen darauf ab, eine Vielzahl von Anwendungen zu unterstützen, die von Breitbandausbau in ländlichen Regionen bis hin zu "Video on Demand" bei ultrahohen Datenraten reichen. Um derartig hohe Datenraten zu ermöglichen, sind jedoch flexiblere und effizientere Nutzlasten erforderlich. Bandbreiten- und leistungseffiziente Transponder verlangen eine Mehrträgersignalanregung der Hochleistungsverstärker (HPAs) des Telekommunkations Satelliten und einen Arbeitspunkt nahe der Sättigung. Dies führt jedoch zu schwerwiegenden linearen und nichtlinearen Verzerrungen aufgrund der erhöhten Inter-Carrier-Interferenz (ICI) und des Intermodulationsrauschens (IMD), wodurch sich die Systemleistung insgesamt verschlechtert. Die in den Kanalverstärkern der On-Board-HPAs eingebauten analogen Linearisatoren bieten nur eine begrenzte Verstärkung und sind nicht adaptiv. Außerdem erwartet der neueste Standard für digitales Video-Broadcasting (DVB-S2X) Uplink-Signale mit Bandbreiten, die in etwa der Bandbreite des Eingangsmultiplexers (IMUX) und des Ausgangsmultiplexers (OMUX) des Transponders entsprechen. Dies führt zu starken linearen und nichtlinearen Verzerrungen, insbesondere für die Trägersignale an den Randbereichen. Zur Kompensation der genannten Verzerrungen werden Entzerrer am Empfängerterminal in Betracht gezogen, die jedoch die Komplexität des Empfängers deutlich erhöhen. Angesichts jüngster Fortschritte bei On-Board-Prozessoren (OBPs) können die von den HPAs und Transponderfiltern verursachten Verzerrungen an Bord des Satelliten durch den Einsatz von Linearisierungstechniken wie der digitalen Vorverzerrung (DPD) reduziert werden, während gleichzeitig ein hohes Maß an Leistungs- und Bandbreiteneffizienz erhalten bleibt. Die vorliegende Arbeit konzentriert sich deshalb auf Vorverzerrungsmethoden an Bord des Satelliten und schlägt die „adaptive, gedächtnisbehaftete polynombasierte“ DPD für bandbegrenzte Signale als die am besten geeignete Vorverzerrungsmethode für HTS vor. Die bandbegrenzte DPD ermöglicht die Verwendung von Wandlern mit niedriger Abtastrate in OBPs, woraus eine geringe Leistungsaufnahme resultiert. Diese Arbeit stellt eine neuartige, iterative und auf der direct learning Architektur (DLA) basierende, bandbegrenzte, gedächtnisbehaftete polynombasierte (MP) DPD vor und vergleicht ihre Leistung mit einer auf dem Stand der Technik befindlichen, in-direct learning Architektur (IDLA) basierenden, bandbegrenzten MP-DPD. Der neuartige DLA-basierte DPD-Ansatz übertrifft den IDLA-basierten DPD-Ansatz, insbesondere unter strengen Bandbeschränkungen. Darüber hinaus werden in dieser Arbeit die Ergebnisse einer umfassenden Untersuchung zur Identifizierung und Optimierung der Systemparameter für die beste DPD-Leistung vorgestellt. Außerdem hebt die Analyse zur Identifizierung der Systemparameter auch die Szenarien hervor, in denen die Implementierung von DPD möglich ist. Abschließend werden in dieser Arbeit die Vorteile einer Implementierung des vorgeschlagenen neuartigen DLA-basierten DPD in Multi-port-Verstärkern (MPA) und 5G-Wellenformen diskutiert und vorgestellt.

Betreuer: Universitätsprofessor Dr.-Ing. Andreas Knopp, MBA

Acknowledgments

First and foremost, all the praises belong to Allah, the greatest and the exalted, on whom ultimately, we depend for sustenance and guidance. I thank Him for bestowing upon me the opportunity, strength and faculties to undertake this research work.

Next, I owe a great debt of deep and sincere gratitude to my Ph.D. supervisor, Prof. Dr. Andreas Knopp for his invaluable guidance, consideration and unfailing support. He is a man of excellent qualities of head and heart. This vividly makes me to acknowledge that probably, I could not have imagined for having a better supervisor and mentor than him. Besides, I also profoundly thank the second reviewer on my thesis committee: Prof. J. A. Nossek for his insightful comments, particularly the hard ones which impelled me to widen my research from various perspectives. His encouragement also warrants a special mention. My sincere thanks also goes promptly to Dr. Thomas Delamotte, Dr. Christian Hofmann, and Dr. Robert Schwarz who supported my research work immensely and co-authored many research publications. Without their support, it would not have been possible to conduct this research. I am also deeply grateful to my all fellow teammates for their help, cooperation and numerous stimulating discussions which benefited my research work greatly. Amongst them, I always felt at home.

Last but not the least, my family to whom I owe everything. They stood with me at every step of my life and longed to see this achievement come true. I dedicate this work to them, in particular to my affectionate father and loving mother.

Ovais Bin Usman

Contents

List of Figures

List of Tables

Acronyms

5G fifth generation.

ACI adjacent channel interference.

ACPR adjacent channel power ratio.

ADC analog-to-digital converter.

ALC automatic level control.

AM-PM amplitude-phase.

AM-AM amplitude-amplitude.

BER bit error rate.

BPF bandpass filter.

CAMP channel amplifier.

CLBs configurable logic blocks.

CNR carrier to noise ratio.

CR code rate.

DAC digital-to-analog converter.

DBF digital beam forming.

DLA direct learning architecture.

DPD digital predistortion.

DSP digital signal processor.

DVB-S2X digital video broadcasting.

EIRP equivalent isotropic radiated power.

FBMC filter bank multicarrier.

f-OFDM filtered orthogonal frequency division multiplexing.

FEC forward error correction.

FPA fixed-point-arithmetic.

FPGA field programmable gate array.

GMP generalized memory polynomial.

HPA high power amplifier.

HTS high throughput satellites.

IBO input back-off.

IDLA in-direct learning architecture.

IF intermediate frequency.

IIR infinite impulse response.

IMD inter-modulation.

IMUX input multiplexer.

INET input-hybrid-matrix.

ISI inter-symbol interference.

LDPC low density partiy check.

LNA low noise amplifier.

LO local oscilator.

LS least-squares.

LUT Look-up table.

MMSE minimum mean squared error.

ModCod modulation order and code rate.

MP memory polynomial.

MPA multiport amplifier.

MPAs multiport amplifiers.

MSE mean squared error.

NMSE normalized mean squared error.

NN neural network.

NR new radio.

OBO output back-off.

OBP on-board processor.

OMUX output multiplexer.

ONET output-hybrid-matrix.

OOB out-of-band.

PAPR peak to average power ratio.

RAM random access memory.

RF radio frequency.

SIC successive interference cancellation.

SSPA solid state power amplifier.

TD total degradation.

TID total ionizing dose.

TWTA traveling wave tube amplifier.

UFMC universal filtered multicarrier.

W-OFDM windowed orthogonal frequency division multiplexing.

Nomenclature

Symbols

R_n^2	n^{th}-order elliptical rational function
T_n^2	n^{th}-order Chebychev rational function
G	Power amplifier (PA) gain in Volts
g_{AM}	Gain compression or expansion of the PA, AM-AM characteristics
Φ_{PM}	Phase shift of PA, AM-PM characteristics
K	Non-linearity order of PA or digital predistorter
Q	Memory depth of PA or digital predistorter
$\mathbf{w}$	PA model coefficients
$\mathbf{c}$	Predistorter coefficients
α_{AM}	Saleh model AM-AM coefficient
β_{AM}	Saleh model AM-AM coefficient
α_{PM}	Saleh model AM-PM coefficient
β_{AP}	Saleh model AM-PM coefficient
$h_k[*]$	Volterra kernal of the k-th order
N_p	Number of input and output ports of the multiport amplifier (MPA)
$\mathcal{C}$	A matrix with complex entries
$\mathbf{1}$	A column vector with the first row entry equal to 1, rest of the entries are 0
I_{max}	Maximum number of iterations
γ	Clipping parameter
E_s	Energy per symbol
E_b	Energy per bit
N_o	Noise power density
$\mathcal{N}(0, \sigma_d^2)$	A normal distribution with mean 0, and standard deviation σ_d
$a >> b$	The scalar a is much greater than the scalar b

Operators

$(\cdot)^H$	Conjugate transpose (Hermitian) of a complex matrix
$\|\cdot\|$	Absolute value
$(\cdot)^T$	Transpose of matrix
$\angle x(n)$	Phase of $x(n)$ in radians

Chapter 1

Introduction

The future of satellites lies in the deployment of high throughput satellites (HTS). Today the satellite industry is moving from a broadcast to a unicast paradigm which has led to an extensive use of HTS. A HTS system splits the service area in to a multi-spot area and exploits a high level of frequency reuse to provide higher data rates at lower costs. Moreover, HTS will also play an important role in the coming fifth generation (5G) of mobile communications, providing services like mobile enterprise, disaster relief, remote location automation, and maritime services [1–3]. Over the past years, efforts have been made to converge the satellite systems towards the terrestrial systems, especially in the context of physical layer [4, 5]. A satellite communication system interfacing with the terrestrial entities is illustrated in Fig. 1-1. A satellite communication system is composed of a space, ground and control segment. The space segment contains the constellation of satellites, while the ground segment consists of all the earth stations such as gateways, mobile handsets and small service stations. The control segment performs services like tracking and managing of the traffic and resources on-board the satellite. While the ground and control segments play a vital role in a successful operation of a satellite-terrestrial communication system, this work focuses on the space segment, especially on the satellite's payload. The payload consists of the receiving and transmitting antennas along with all the electronic equipment (e.g. filters, amplifiers, on-board processors etc.) which support the transmission of the received data back to earth. The two types of payloads

architectures, namely regenerative and transparent, which are typically employed in satellites are illustrated in Fig. 1-2.

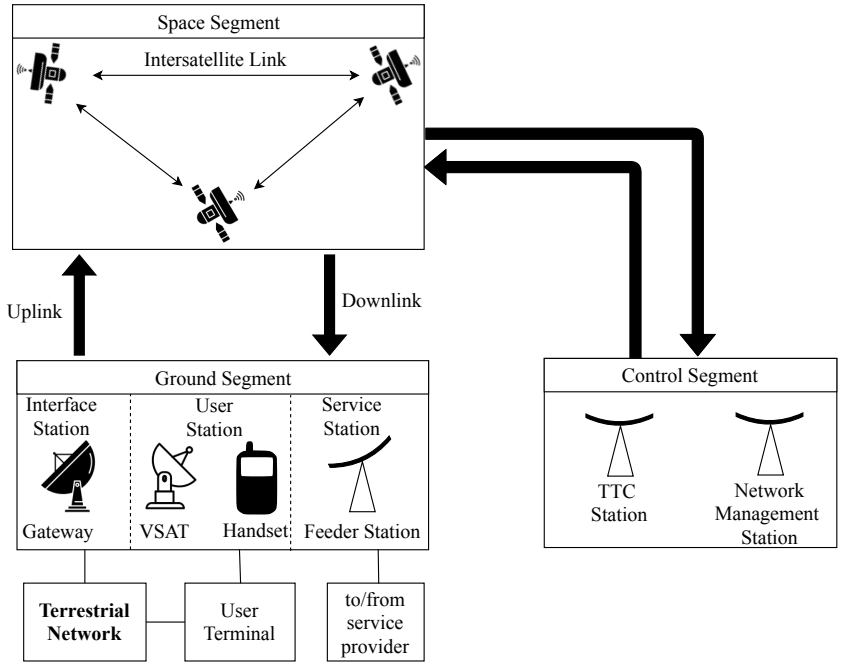

Figure 1-1: A satellite communication system interfacing with terrestrial networks.

1.1 Regenerative Vs. transparent payloads

In current satellite payloads, the over all payload bandwidth is split into several sub-bands due to power constraints. Moreover, the carriers in each sub-band are amplified by a different amplifier [6]. The payload chain responsible for the amplification of a single sub-band is called a transponder. The splitting of the payload bandwidth is achieved by a set of bandpass filters called the input multiplexer (IMUX). Fig. 1-2a presents a simplified regenerative payload architecture. The splitted carriers in regenerative payloads are demodulated and pulse-shaped again by a on-board processor (OBP) before amplification. The output multiplexer (OMUX) combines the amplified carriers before they are transmitted back to earth. Nowadays, the transparent payload architectures are being increasingly considered for HTS. In transparent payloads, the splitted carriers are merely amplified and frequency shifted. Fig. 1-2b presents such an architecture.

TTC: tracking telemetry and command

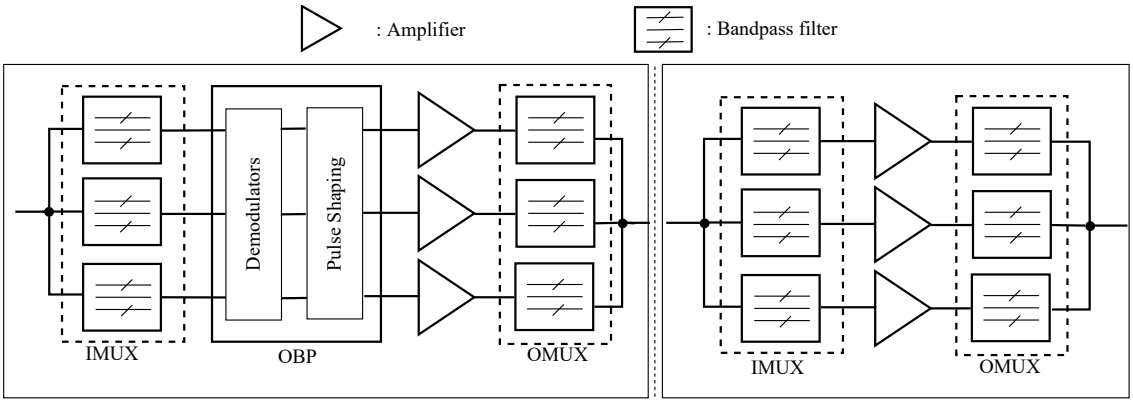

(a) Regenerative (b) Transparent

Figure 1-2: Regenerative and transparent payload architectures.

The future HTS also consider employing on-board processors in the transparent payload architectures to obtain higher flexibility and accurate routing/switching capabilities, especially in multi-beam satellites [7]. Furthermore, the contemporary OBPs can accurately implement adaptive algorithms to counteract distortions present in the satellite communication chain directly on-board the satellite, without first demodulating the uplinked signal. Lately, the regenerative payloads have become less popular due to their intrinsic rigidity with respect to the physical layer interface [8]. Therefore, this work considers a transparent payload architecture with an OBP to implement adaptive solutions for compensating the linear and non-linear distortions that exist in a satellite communication chain. Such architectures will be discussed at length in the upcoming chapters. An example of such an architecture is illustrated by Fig. 2-1 in Chapter 2.

1.2 Distortions in the satellite communication chain

Different sources of distortions exist in a satellite communication chain such as the thermal noise of transmit/receive antennas, interference from nearby sources, weather etc [6,8,9]. However, this work primarily focuses on the distortions caused by the physical components on-board the satellites, especially the non-linear distortions caused by the transponder's high power amplifier (HPA) and the memory effects introduced by the payload's IMUX and OMUX filters.

Non-linear distortions: HPAs are inherently non-linear and power hungry devices. They can consume up to 70% of the system energy [10]. Power is a limited resource in satellites, therefore, it should be utilized efficiently. A common way to increase the power efficiency of the on-board HPAs is to operate them closer to the saturation point [11–13]. However, an operation close to saturation introduces severe non-linear distortions in the amplified signal. On the contrary, the ground station amplifiers have a much higher saturation power, and are driven deep in the linear region. A high power efficiency is not a vital performance metric in the ground station amplifiers as it is in the case of on-board amplifiers.

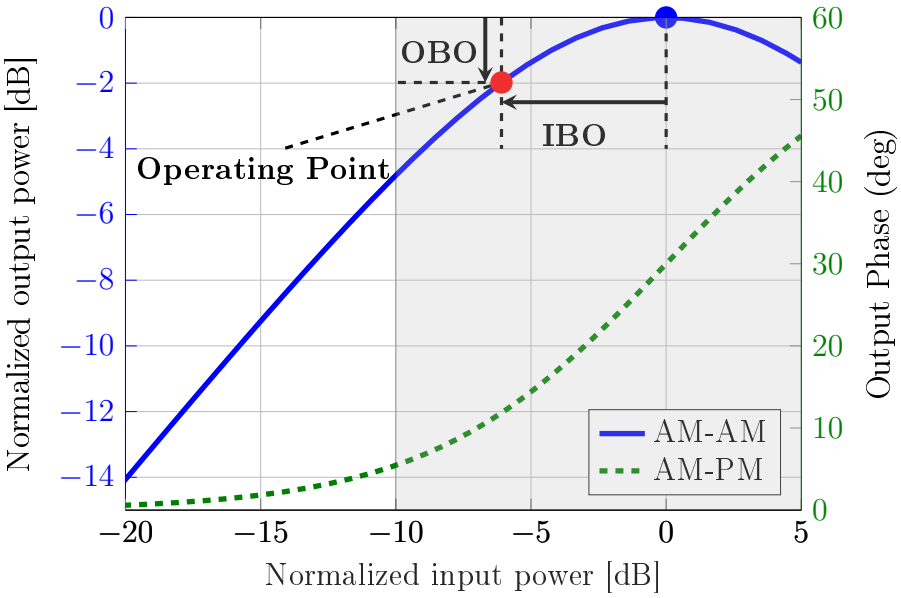

Figure 1-3: AM-AM and AM-PM curves for a typical TWTA in a satellite payload.

Fig. 1-3 presents the normalized amplitude-amplitude (AM-AM) and amplitude-phase (AM-PM) transfer characteristics of a typical traveling wave tube amplifier (TWTA), where the input back-off (IBO) and output back-off (OBO) are defined as the input (P_{in}) and output power (P_{out}) divided by the saturation power (P_{sat}), respectively. The HPA operation in the non-linear region (highlighted in grey) results in significant amplitude and phase distortions in the amplified signal. Moreover, operating near saturation (i.e., a higher IBO in Fig. 1-3) results in increased intermodulation (IMD) noise and out-of-band (OOB) radiation at the HPA output, which can be observed in Fig. 1-4. A higher OOB radiation leads to a larger adjacent channel

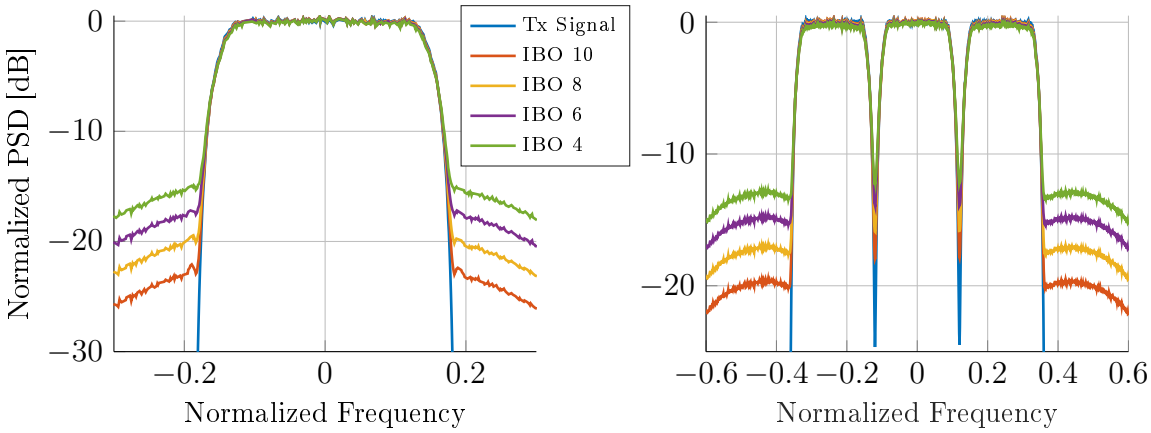

(a) Single carrier excitation of HPA.

(b) Multicarrier excitation of HPA.

Figure 1-4: A spectral regrowth comparison between a single and multicarrier excitation of HPAs.

power ratio (ACPR), and a higher IMD noise leads to the clustering and warping of the signal constellation causing a high bit error rate (BER) [13, 14]. The aforementioned non-linear effects and their definitions are detailed in Chapter 2 Section 2.4.3.

Lately, the multicarrier operation of the on-board HPAs is becoming more common as the satellite operators seek to extract the maximum efficiency from the satellite's resources by re-using the on-board HPAs to serve multiple transponders. This also keeps the total number of HPAs in the payload low [15], leading to a lower dry launch mass and reduced power consumption. In addition, the multicarrier mode also increases the bandwidth efficiency of the HPAs. However, it also leads to server inter-carrier-interferences (ICI) especially when the HPAs are operated close to saturation. From Fig. 1-4, it can be observed that operating HPAs in the multicarrier mode results in higher adjacent channel interference (ACI) and OOB when compared to the single carrier operation. Furthermore, the non-linearities introduced by the HPA become more significant when higher order modulation schemes are employed [16].

Linear distortions and memory effects: Apart from the distortions caused by the non-linear operation of the HPAs, memory effects introduced by the payload's IMUX and OMUX filters, especially in wideband applications account for a large portion of the overall distortion observed in a satellite channel [17]. The latest DVB-S2X standard is pushing for signals with bandwidths that are more or less equal to

that of the IMUX and OMUX. This introduces severe linear and non-linear distortions such as inter-symbol-interference, especially for the carriers at the edges. The effects of IMUX and OMUX on system performance are detailed in Chapter 2 Section 2.2.3.

1.3 Compensating the linear and non-linear distortions

Future HTS push for very power and bandwidth efficient transponders to cope up with the demand of extremely high data rate transmission [18, 19]. However, as discussed in the previous section that operating the transponder's HPA closer to saturation and in multicarrier mode to achieve higher power and bandwidth efficiency results in severe linear and non-linear distortions in the payload's output. Therefore, these distortions have to be compensated for.

Analog Vs. digital solutions: To reduce the non-linear distortions in the HPA output, an analog linearizer is typically built in the channel amplifier (CAMP) (see Chapter 2 Section 2.4.1) of the HPA [6]. The analog linearizer (or the analog predistorter) is a circuit having transfer characteristics opposite to that of the main power amplifier's transfer characteristics. An analog linearizer can achieve a sound linearization performance [20, 21] and is a cost effective solution, especially at high bandwidths [22]. However, it is not a practical solution for HTS where flexibility, performance accuracy and adaptivity are of the utmost concern. Moreover, analog linearizers over time suffer from a degradation in performance due to the variation in the HPA's non linear characteristics induced by changes in temperature and aging effects [23]. In addition, flexible payloads require dynamic carrier placement which in turn affects the non-linear behavior of HPAs (See Chapter 3 Section 3.3.6). Furthermore, analog linearizers are only an approximate inverse of the power amplifier characteristics, and do not cater for the memory effects. Therefore, their non-adaptive and memoryless nature makes them an impractical standalone solution for HTS. This pushes for the need of more accurate digital solutions to invert the non-linear HPA characteristics. In addition, according to [22, 24], the trends in linearization methods

for terrestrial and satellite communications have shifted from analog to digital. With the advent of bandwidth-efficient and high data rate digital modulation schemes (e.g., 32-APSK, 64-QAM etc.), the need of higher linearity and adaptive predistortion in HPAs has led to the beginning of digital linearization. When such digital solutions are applied either on-ground before transmission or in the satellite before amplification, they are called digital predistortion (DPD) [6, 10]. In addition, Beidas et al. in [25, 26] and Kelly et al. in [17] advocate for adaptive DPD solutions over the analog counterparts. Moreover, the non-linearities added by the wideband HPAs are not only dependent on the IBO, but also on the signal characteristics such as the number of carriers, modulation order, bandwidth etc. Therefore, adaptive predistortion algorithms should be considered for future HTS to linearize the HPAs and to track the changes in signal characteristics.

On-ground Vs. on-board solutions: Digital predistortion (DPD) can be either implemented on-ground at the gateway or on-board the satellite. In a typical HTS application scenario involving multiple gateways, implementing on-ground DPD would require the knowledge of all the symbols or carriers, which are to be amplified by a single on-board HPA, at a centralized location on earth which is not possible all the time. Hence, it is more feasible to implement DPD on-board the satellite. Moreover, implementing adaptive predistortion solutions on-board the satellite would also be more efficient. This is because the HPA input and output are readily available without any delay or additional noise (e.g. AWGN). DPD can be implemented at symbol or waveform level, referred to as data or signal predistortion, respectively. Apart from DPD, equalization-based solutions at the receiver are also widely present in the literature for compensating the non-linear channel effects. References [27] and [28] present the Volterra-based equalizers which can mitigate the non-linear ISI and IMD present in a satellite communication chain. However, the advantage of DPD, especially on-board the satellite, lies in the fact that only a single system is needed to cancel the HPA non-linearity compared to using an equalizer at each user terminal [10]. Therefore, it makes sense to employ predistortion especially on-board the satellites since OBPs will be a part of the payload in the future HTS.

On-board processors and DPD: As discussed in Section 1.1, the future HTS incorporate transparent transponders with on-board processing capabilities [29]. The OBPs enable the accurate implementation of signal processing algorithms such as beam-forming and predistortion directly on-board the satellite. Many of the state-of-the-art signal DPD algorithms implemented in terrestrial communications [11, 12, 23] can be easily extended to satellite specific scenarios, and can be applied directly on-board the satellite using OBPs. However due to limitations like weight, power and the radiation hardening requirements of the hardware in satellites, less powerful OBPs are generally employed. An OBP consists of radiation hardened digital signal processors (DSPs), analog to digital (ADCs), and digital to analog converters (DACs). Typically, the radiation hardened components lack the processing and sampling capabilities of their counterparts employed on-ground (See Chapter 2 Section 2.3). In order to implement on-board adaptive signal DPD algorithms, a feedback loop is required, i.e., the HPA output needs to be fed back to the OBP. Conventionally, the bandwidth of the HPA output reaches about five times that of the input signal bandwidth due to the spectral regrowth [12,30]. Moreover, for HTS scenarios where the input bandwidth per transponder can reach up to 500 MHz, capturing the complete HPA output bandwidth in the feedback path is not possible or practical. Sampling such high bandwidth signals in the feedback path would imply using ADCs and DSPs with ultra high sampling rates which currently is not possible, and would consume a lot of power. Apart from the DSPs, the ADCs, and DACs also consume a large chuck of the total power available to the satellite. Furthermore, the power consumption of ADCs/DACs scales linearly with the sampling rates [31]. In fact, one ADC can consume up to 9.7 Watts and one DAC can utilize up to 3 Watts when operating at ultra high sampling frequencies [29]. Therefore, in order to implement practical DPD algorithms, a constraint is put on the sampling rate requirements (or sampling bandwidths) to reduce the power consumption.

Bandlimitation and DPD: To perform adaptive DPD for HTS, the bandwidth of the feedback path is often restricted by an analog bandpass filter to allow the use of low sampling rate ADCs and DSPs [32]. This leads to reduced power consumption

requirements, and to low complexity payloads [12]. Moreover, predistortion itself is a non-linear operation which results in the bandwidth expansion of the input signal (See Fig. 3-8). The entire bandwidth of the predistorted output cannot be sampled back to an analog signal due to the lack of space grade DACs with very high sampling rates. As a result, a bandlimitation is also introduced in the forward path through a digital bandpass filter. Therefore, this work focuses on bandlimited DPD for HTS. As discussed in Section 1.1, a satellite transponder is equipped with an OMUX for filtering out the OOB. However, the very tight guardband of the OMUX introduces linear and non-linear distortions in the HPA output. Complex equalizers are needed in the receivers to remove these distortions. However, this would significantly increase the cost and complexity of the receivers. On the other hand, if the feedback signal for the adaptive on-board DPD is taken from the output of OMUX, then with appropriate modeling, the predistorter can also mitigate these distortions. Thus removing the need of complex equalizers. The upcoming chapters will detail the considered bandlimited DPD techniques in this work and will provide a detailed analysis of the gains observed when the feedback loop is started from the output of the OMUX.

DPD methods for HTS: Different classes and types of DPD methods are detailed in Chapter 3 Section 3.2 and 3.3. Moreover, Chapter 3 Section 3.3.6 proposes the Volterra-based memory polynomial (MP) DPD solution as the most suitable DPD method for HTS. The lookup table (LUT) [33, 34], neural network (NN) [35–37], and p-th order inverse-based [38–40] DPD methods are not practical for HTS as they exhibit high computational complexity, especially in wideband applications (See Table 3.1). These approaches require an extremely large number of DPD coefficients in wideband operation on the account of higher memory effects [37]. This makes their on-board implementation very expensive since higher computational complexities lead to larger computing delays and increased power consumption. The successive interference cancellation (SIC)-based DPD methods [25, 41] are non-bandlimited in nature, require a large number of internal iterations, and their open loop structure is sensitive to loop maladjustments [42]. On the other hand, MPs are extensively used in the literature to implement signal DPD for both in-direct (IDLA) [11], [43] and

direct learning architectures (DLA) [12], [44]. The low computational complexity and linear parameterization of MPs makes them well suited for on-board DPD. Therefore, the IDLA and DLA-based MP bandlimited DPD approaches are the main focus of this work.

1.4 Main contributions

Previous sections highlighted the linear and non-linear distortions associated with the payload's HPAs and transponder filters, and suggested the IDLA and DLA-based MP bandlimited DPD as a solution to compensate these distortions. This section discusses some novel aspects in the field of DPD for HTS studied in this thesis.

1.4.1 System parameters identification analysis

The DPD performance is dependent on several parameters e.g. uplink signal, DPD algorithm-specific and transponder parameters. Most of the research present in the literature presents the gain of a particular DPD algorithm for a fixed set of parameters. On the other hand, this work focuses on identifying the key system parameters which effect the DPD performance. To this end, the performance of the proposed DPD methods is thoroughly analyzed for different uplink signal, transponder and predistortion algorithm specific parameters. Moreover, the presented work provides a set of system parameters and scenarios where it is feasible to implement DPD. In author's opinion, identifying the key parameters which effect the DPD performance can serve as a basis for the optimization of DPD algorithms to maximize their gain, and to facilitate their implementation in hardware platforms.

1.4.2 Bandlimitation analysis

Section 1.3 introduced adaptive DPD, and the concept of bandlimitation in the forward and feedback path to reduce the power consumption of the digital architecture on-board the satellite. The bandlimitation is achieved via bandlimiting feedback and forward path filters. This work analyzes the effect of bandlimitation on the DPD performance. It is vital to study the effects of varying the bandwidth of the bandlimiting filters, as their bandwidth directly influences the required sampling rates for

ADCs and DACs (See Figure 3-7). Table 2.2 presents the typical bit-resolution, maximum supported sampling rates and power consumption for a few radiation-hardened space grade ADCs. It is clear from Table 2.2 that the higher sampling rate ADCs are only available for low bit-resolutions. In addition, the ADCs consume more power at higher sampling rates. Note that reducing the bandwidth of the bandlimiting filters would lead to a requirement of lower sampling rates for the ADC and DAC in Figure 3-7. This in turn would lead to a reduced power consumption, and a higher bit-resolution conversion. A higher bit-resolution in converters introduces smaller quantization noise. Therefore, it is important to analyze the effects of changing the bandwidth of the bandlimiting filters on the DPD performance. Moreover in this work, extensive simulations are performed to find out how low the forward and feedback path filter's bandwidth can be with respect to the transmitted signal bandwidth to still achieve a gain when DPD is implemented. Furthermore, this work also studies the recovered gain in performance when a novel iterative DLA-based DPD algorithm (See Chapter 3 Section 3.3.5) is applied under the bandlimitation constraints. The system parameter identification analysis and bandlimitation analysis is presented in Chapter 4.

1.4.3 DPD for multiport amplifiers

Future HTS require not only power efficient but also flexible payloads to optimize their performance for different operational conditions [45]. One of the most important payload flexibility means is the capability of sharing radio frequency (RF) output power among different service beams in order to handle unexpected traffic unbalances and variations over time [46]. Multiport amplifiers (MPAs) offer a practical solution for the payload's power flexibility requirements and have been studied as an effective approach in multi-beam systems [47]. A MPA is an implementation of the transponder's power amplification section that allows the sharing of the payload RF power among several beams/ports, and guarantees a highly efficient exploitation of the available satellite power [48].

Implementation issues:

A MPA consists of hardware components like the input/output 3 dB couplers referred to as input-hybrid-matrix (INET)/output-hybrid-matrix (ONET), and stacked power amplifiers (PAs). For MPAs to operate ideally, the magnitude and phase relations at the output of the INET and ONET should be balanced, and the stacked PAs must have equal linear gains. Otherwise, the inputs signals cannot be recombined optimally to their respective output ports of the MPA [49]. However, due to aging and hardware imperfections, the operation of INET and ONET is often compromised, and the PAs exhibit unequal and non-linear gains, ultimately leading to port isolation problems [50] and unwanted power losses.

Solution for hardware imperfections in MPAs:

This work details a two-step adaptive method which describes a novel technique to effectively compensate the effects of an imperfect INET/ONET in its first step, and performs bandlimited DPD [11,12] for the stacked non-linear HPAs in the second step. The novel iterative DLA-based DPD is applied in the second step. It should be noted that no such technique exists in the literature which utilizes the OBP to digitally compensate for the INET/ONET imperfections.

1.4.4 DPD for 5G waveforms

As mentioned earlier, the HTS will also play a crucial role in providing different 5G services. Moreover, in order for satellite and terrestrial networks to co-exist, a shared spectrum would be preferred. Therefore, it is also important to study and analyze the performance of the new radio (NR) 5G waveform for HTS. The NR and other 5G candidate waveforms suffer from high peak to average power ratio (PAPR) which saturates the HPA leading to severe non-linear effects in the transponder's output. The later chapters of this thesis briefly summarize different PAPR reduction techniques, and propose the on-board signal clipping [51,52] to reduce the PAPR of the uplinked 5G waveform. Even though signal clipping is non-linear and introduces in-band and OOB non-linear effects, it offers minimal computational complexity and can be applied directly to the uplinked signal in the transponder's OBP. This work proposes

a novel joint implementation of PAPR reduction and adaptive bandlimited DPD as another application of the novel iterative DLA-based DPD. It is shown that DPD not only mitigates the IMD and spectral regrowth from non-linear HPA operation, but also reduces the non-linear effects introduced by the signal clipping.

The developed DLA-based DPD in Chapter 3, and the system parameter and bandlimitation analysis presented in Chapter 4 have been published in conference proceedings and in a journal article, respectively. The references of these works are listed below.

Journal

- O.B. Usman, A. Knopp: "Digital Predistortion in High Throughput Satellites: Architectures and Performance" in IEEE Access

Conferences

- O. B. Usman, G. Staude and A. Knopp, "Onboard Compensation of Linear and Non-Linear Hardware Imperfections in Multiport Amplifiers," 2018 IEEE Global Communications Conference (GLOBECOM), Abu Dhabi, United Arab Emirates, 2018, pp. 1-6

- O. B. Usman, G. Staude and A. Knopp, "Adaptive onboard compensation of non-linear HPAs and imperfect butler matrices in multiport amplifiers for high throughput satellites," 36th International Communications Satellite Systems Conference (ICSSC 2018), Niagara Falls, ON, Canada, 2018, pp. 1-8

- O. Bin Usman, T. Delamotte and A. Knopp, "On the Complexity of Sample Vs. Block-Based Predistortion for High Throughput Satellites," 2018 IEEE International Conference on Communications (ICC), Kansas City, MO, 2018, pp. 1-6

- O. B. Usman, A. Knopp and S. Dimitrov, "Onboard PAPR Reduction and Digital Predistortion for 5G waveforms in High Throughput Satellites," 2020 IEEE 3rd 5G World Forum (5GWF), Bangalore, India, 2020, pp. 174-179

To summarize

This work focuses on the applications of OBPs in HTS. The author utilizes the OBPs to implement on-board bandlimited DPD to mitigate the linear and non-linear distortions caused by the transponder's HPAs and multiplexing filters. More importantly, this work helps identify the key parameters which effect the DPD performance. The thesis also presents a novel iterative DLA-based DPD which outperforms the state-of-the-art IDLA-based DPD, especially under severe bandlimitation constraints. The proposed DPD finds applications in many systems. The author discuses its application to 5G waveforms and MPAs.

1.5 Thesis organization

From this point on, this thesis is comprised of 4 more chapters. Chapter 2 presents a transparent HTS transponder in detail. The effects of the IMUX/OMUX filtering and the non-linear operation of the HPAs are also presented with the help of BER, PSD and constellation plots. Chapter 2 also provides the mathematical models for HPAs and MPAs which serve as base for developing DPD algorithms. Predistortion theory is detailed in Chapter 3. Different classes and types of predistortion methods, and relevant mathematical models are provided. Moreover, the chapter also presents the type and class of predistortion which in the author's opinion is best suited for HTS. In addition, the author presents the novel iterative DLA-based DPD solution along with the state-of-the-art IDLA-based DPD. Chapter 3 also discusses two applications of the proposed DLA-based DPD. Firstly, a novel two-step method for compensating the imperfect INET/ONET and non-linear HPAs in MPAs. Secondly, joint PAPR reduction and DPD for 5G waveforms. The performance gains of the novel DLA-based DPD for the discussed applications are also presented in Chapter 3. Chapter 4 presents the numerical analysis for the proposed novel DLA-based DPD and compares its performance with the state-of-the-art IDLA-based DPD in terms of BERs, PSDs, and TD. Most significantly, the chapter provides the simulation results of a thorough investigation made to identify the key parameters which effect the DPD performance. In addition, Chapter 4 also presents the the novel bandlimitation analysis, and a power

and hardware implementation analysis for the proposed DPD methods. Finally, the conclusions are drawn in Chapter 5. The chapter also summarizes the thesis, and discusses the possible research topics which can be derived from this work.

Chapter 2

Satellite transponder for HTS

The previous chapter highlighted the two different payload architectures employed in the current satellites systems, i.e., the transparent and regenerative payloads architectures. Chapter 1 also emphasized on the fact that the future HTS systems will employ transparent payload architecture with on-board processing capabilities. This chapter details such a transponder model for the HTS. Alongside, the conventional HPAs employed in transparent payloads, the chapter will also present the application of multiport amplifiers in HTS. Typically, the exact model of the satellite transponder is determined by the mission specifications and technological constraints. However, a higher-level system model of a satellite transponder for HTS is presented in Fig. 2-1. The details of each blocks are discussed in the following.

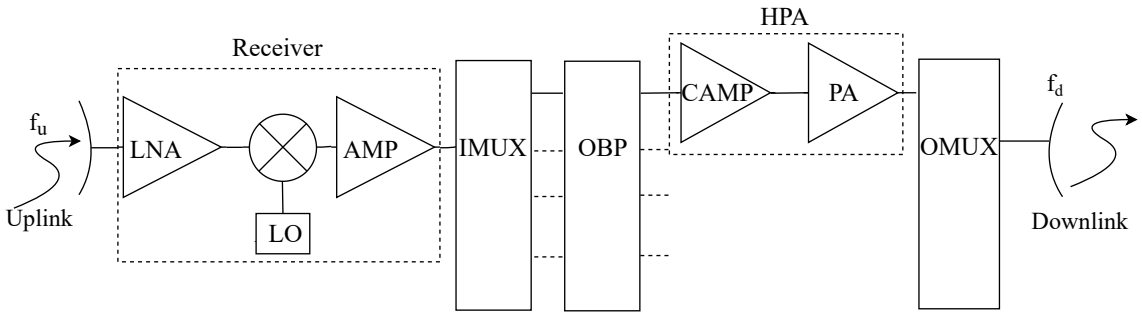

Figure 2-1: A transparent payload with OBP for HTS.

f_u: uplink frequency, f_u: downlink frequency

2.1 Receiver: low noise amplification and frequency conversion

The receiver is a section of the transponder which operates over the entire system bandwidth. A simplified structure of the receiver is also drawn in Fig. 2-1. In the receiver, frequency conversion by the mixers is one of the first steps to be performed on the received carriers. However, a direct frequency conversion of the received carriers does not satisfy the required system noise temperature specification due to the high noise figures of the typically employed mixers [53]. Therefore, most of the receivers are equipped with a low noise amplifier (LNA) [54] which provides the required value of the effective input noise temperature at the uplink frequency. LNAs have a low noise temperature, and they can provide a high gain (20-40 dB) to limit the noise contribution of the subsequent stages, especially the mixing stage. After the low noise amplification, frequency down-conversion is performed by the mixers using a local oscilator (LO). Down-conversion to lower intermediate frequencies (IFs) makes the operations like filtering and signal processing much simpler and faster [6]. The frequency conversion between the uplink and downlink also ensures the decoupling between the input and output of the transponder.

2.2 Input and output multiplexing filters

The receiver is typically followed by the IMUX. The IMUX defines the beginning of channelized section of the satellite transponder. The receiver stage of the transponder operates on the complete bandwidth (hundreds of MHz). Many carriers share this bandwidth, and as these carriers pass through the amplification stages of the receiver, they gives rise to a large number of IMD products. To limit the amount of IMD noise entering the following stages, channelization of the carriers is performed via the IMUX. This limits the number of carriers passing through the amplifiers in the coming stages. Essentially, multiplexers are passive devices which can either split a signal from a single source to different outputs, or they can combine signals at different frequencies from different sources onto a single output. Multiplexers in satellites are basically highly selective branching/combing bandpass filters (BPFs).

2.2.1 Input multiplexer (IMUX) filter

The IMUX filter channelizes the complete system bandwidth into different sub-bands. The bandwidth of different channels is defined by a set of BPFs [55]. These BPFs select the desired frequency bands on which a single power amplifier will operate. Typical narrowband designs of the IMUX filters can achieve a channelized bandwidth of as low as 16 MHz. While, the wideband designs can obtain a channelized bandwidth of up to 500 MHz in Ku-Band. In general, the IMUX filter is designed to handle low power signals, since it comes before the transponder's HPA in the payload [17]. For modeling purposes, the IMUX filter can be realized as an elliptical or Chebychev infinite impulse response (IIR) filter. The magnitude responses for the n^{th}-order elliptical and Chebychev filter as a function of angular frequency are given below.

$$G_n^{\text{Elip}}(w) = \frac{1}{\sqrt{1+\epsilon^2 R_n^2(\xi, w/w_o)}} \text{ (a)}, \qquad G_n^{\text{Cheb}}(w) = \frac{1}{\sqrt{1+\epsilon^2 T_n^2(w/w_o)}} \text{ (b)}, \quad (2.1)$$

where w_o is the cut-off angular frequency, ϵ is the ripple factor and ξ is the selectivity factor. R_n^2 and T_n^2 are the n^{th}-order elliptical and Chebychev rational functions [56], respectively. Fig.2-2a presents the group delay and attenuation characteristics of a typical IMUX filter as implemented in the DVB-S2X standard [57].

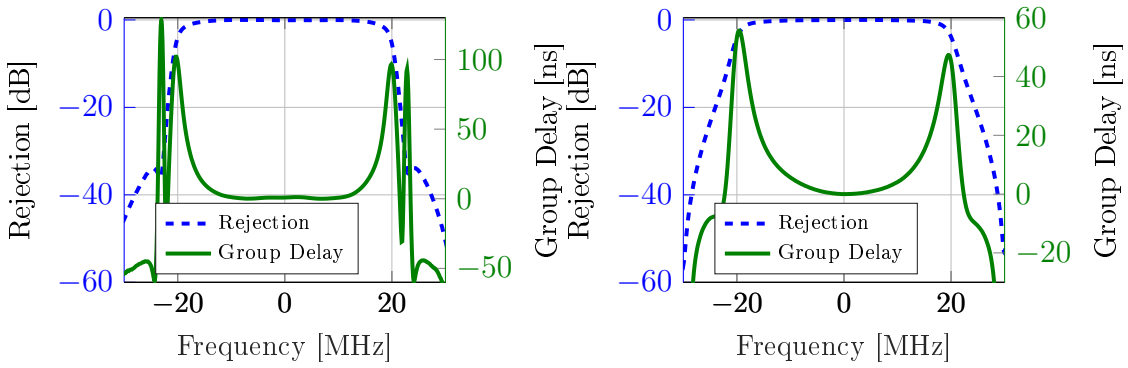

(a) IMUX. (b) OMUX.

Figure 2-2: IMUX and OMUX magnitude and group delay response. Filter BW: 36 MHz.

IMUX/OMUX filter BW is defined as the 3dB bandwidth [57].

2.2.2 Output multiplexer (OMUX) filter

The OMUX filter marks the end of the channelized section of the payload. The OMUX filter recombines the channels after the power amplification stage. Moreover, the OMUX also filters the downlink signal to remove the OOB components which are generated during the non-linear power amplification. However, this leads to a reduction in radiated power too. Unlike the IMUX, which handles signals with relatively low power, the OMUX operates on the high powered output of transponder's power amplifier. Therefore, the OMUX characteristics are different from the IMUX characteristics, and are depicted in Fig.2-2b. The OMUX bandpass filters can also be modeled by an elliptical or Chebychev IIR filter with several poles (four to eight). Moreover, unlike the IMUX where the losses are compensated by the channel amplification, the losses in the OMUX are critical since they lead to a direct reduction in the radiated power [6]. To avoid significant power loss, the coupling of the bandpass filters in the OMUX is accomplished by mounting the filters on a common wave guide instead of the bulky microwave circulators. Furthermore, to maximize the utilization of transponder bandwidth and minimize the OOB, the OMUX bandpass filters are often designed with a much tighter guardband compared to the IMUX. However, a tighter guard band leads to distortions in the downlink signal. These distortions are summarized in the following.

2.2.3 Filter channel impairments

The IMUX and OMUX are analog filters which are built in hardware. As a result, ideal filter characteristics such as constant group delay and equal rejection across the passband cannot be assumed. The IMUX and OMUX filters introduce linear distortion in the form of memory effects due to frequency selectivity at high baud rates, which also corrupts the matched filtering at the receiver and amplifies the AWGN [41]. Other effects of non-ideal filtering include inter-symbol interference (ISI) and clustering of constellation points (see Fig. 2-7b). Furthermore, these effects are enhanced for weaker forward error correction (FEC) code rates, higher baud rates and larger modulation orders [41]. Additionally, due to tighter guardband requirements,

the in-band characteristics of the OMUX, especially the group delay characteristics vary significantly when compared to the group delay characteristics of the IMUX (see Fig. 2-2). Severe fluctuations in the group delay across the in-band leads to a phase shift in the spectral components of the wideband downlink signal. This causes distortions, and ultimately reduction in the system performance. As a solution, an average group delay of the OMUX can be computed and applied at the ground station's receiver to compensate for such distortions. However, the average group delay can only be applied across the entire signal bandwidth, i.e., some frequency components will be still misaligned, leading to a decline in signal quality [17].

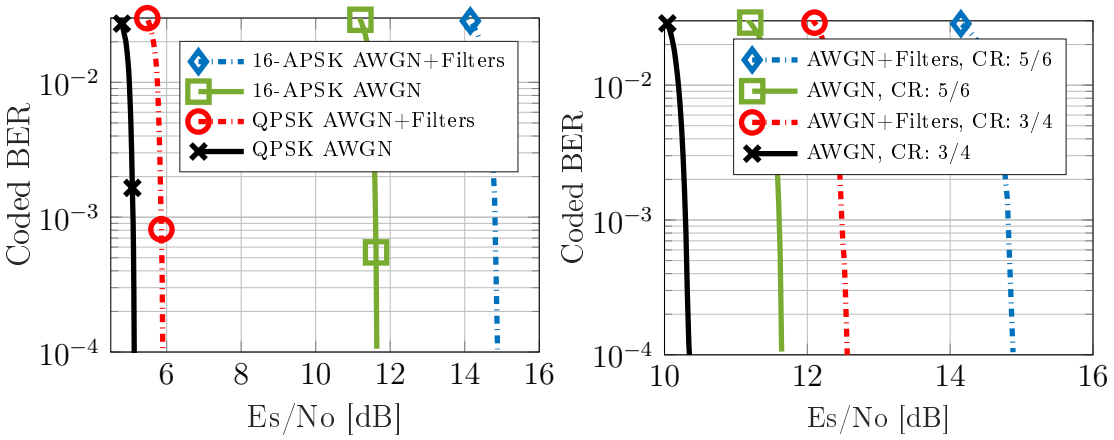

(a) Modulation: QPSK, 16-APSK, CR:5/6 (b) Modulation: 16-APSK, CR:3/4, 5/6

Figure 2-3: IMUX and OMUX filtering Vs. ModCods, Baud Rate: 27.5 MHz, Roll-off:0.2, IMUX/OMUX BW: 36 MHz.

Linear distortions Vs. ModCods

Fig. 2-3 presents the simulated BER performance with respect to (w.r.t) modulation order and code rates (ModCods) in the presence of IMUX/OMUX filtering. A single carrier signal with a 33 MHz bandwidth is uplinked. The satellite transponder has a 36 MHz IMUX and OMUX with rejection and group delay characteristics depicted in Fig. 2-2. The simulated transponder's HPA is operated deep in the linear region to study only the effects of IMUX/OMUX filtering. Fig. 2-3a contains the curves for QPSK and 16-APSK modulation schemes with FEC coding implemented in the form of the low density partiy check (LDPC) codes with a code rate (CR) of

$\frac{5}{6}$. It is observed from the figure that the BER performance suffers in presence of the IMUX/OMUX when compared to the AWGN case only. Furthermore, the loss in BER performance is more significant for the higher order modulation scheme (16-APSK) when compared to the lower order modulation scheme(QPSK). Furthermore, Fig. 2-3b presents the effect on system BER performance when a stronger LDPC code is employed under non-ideal filtering conditions. From Fig. 2-3b, it is clear that the signal with a stronger code rate, i.e., $\frac{3}{4}$ has a smaller loss in BER performance when filtering is introduced. Stronger FEC codes create a constellation which is more robust to the clustering effects. However, a stronger code rate reduces the throughput and does not solve the underlying problem of linear distortions due to non-ideal filtering.

Linear distortions Vs. baud rate

Fig. 2-4 provides the simulated BER curves w.r.t different baud rates in the presence of IMUX and OMUX filtering. Same transponder characteristics are assumed as in the Fig. 2-3a. It is clear from the Fig. 2-4 that the loss in BER performance is larger for higher baud rates. A higher baud rate leaves a minimal guardband for the carrier, thus leading to severe linear distortions. The demand of a higher throughput

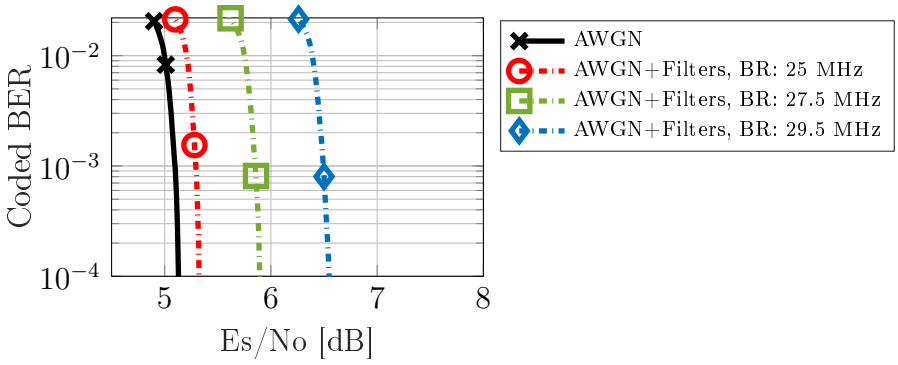

Figure 2-4: Linear distortions Vs. baud rates, Modulation: QPSK, Code rate:5/6, Carriers:1, Roll-off:0.2, IMUX/OMUX BW: 36 MHz.

in satellites has pushed for the need of higher ModCods and larger baud rates in the upcoming communication standards. However, Fig. 2-3 and Fig. 2-4 highlighted the fact that increasing the modulation order, code rate and baud rate magnifies the introduced linear distortions. A stronger FEC code can be applied to reduce these

distortions (see Fig. 2-3b), however this decreases the throughput. As a solution, the DVB-S2X standard [58] proposes a fractionally spaced equalizer to mitigate the distortions caused by the non-ideal filtering. But, the equalizer in [58] has 42 complex taps which leads to an increased receiver design complexity. However, with the developments in OBPs, on-board DPD with appropriate modeling can be applied to not only remove the non-linear but the linear distortions as well. Modeling of predistorters to remove the aforementioned linear effects will be discussed in the coming chapters.

2.3 On-board processor (OBP)

The performance and efficiency of the satellite payloads can be enhanced by employing OBPs. Contemporary OBPs offer reliable RF switching/routing [59]. Moreover, they also support baseband signal processing capabilities for implementing algorithms like digital beam forming (DBF) and predistortion. Thus, the payloads equipped with OBPs are a significant improvement over the analog counterparts. Furthermore, the state-of-the-art OBPs can be reconfigured from earth, thus allowing flexible adaptation to the new communication standards or changed environmental conditions. The OBP is installed in the channelized section of the payload right after the IMUX as depicted in Fig. 2-1. A higher-level zoomed-in picture of an OBP is drawn in Fig. 2-5.

2.3.1 Digital signal processors (DSPs)

At the core of the OBP is digital signal processing, a computational process reduced to solid-state electronics (see Fig. 2-5). The on-board DSPs are designed using the radiation-resistant field programmable gate arrays (FPGAs). The natural space environment is a highly charged environment where the satellite electronics is subjected to high amounts of radiation which ultimately leads to a loss of circuit functionality [60]. Therefore, for microelectronics circuits to function properly in space, they must be hardened to withstand the effects of the absorbed radiation. Even though significant developments have been made in OBP technologies, the radiation

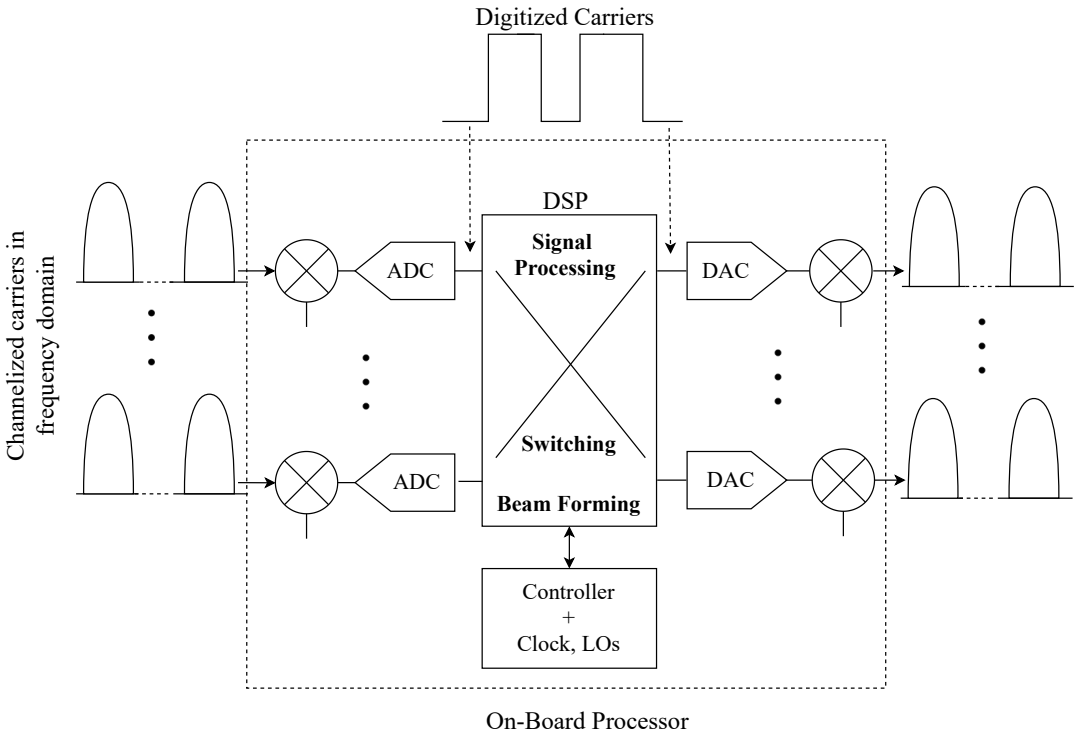

Figure 2-5: A higher-level diagram for an on-board processor (OBP).

hardened devices tend to lag behind their counterparts employed in the terrestrial systems. Table 2.1 summarizes a comparison between a state-of-the-art on-ground and an on-board FPGA in terms of the transceiver and DSP characteristics [61, 62]. It is clear from the table that the on-board FPGA is much slower and less powerful compared to the on-ground counterpart. Therefore, the baseband signal processing algorithms which are to be implemented on the on-board FPGAs e.g. predistortion or beamforming, should be low-effort and computationally less demanding.

Table 2.1: State-of-the-art on-ground and on-board FPGAs.

	Ground FPGA Xilinx Virtex-7	On-Board FPGA Xilinx Virtex-5QV
No. of transceivers	48	18
Max transceiver baud rates	11.3 Gb/s	4.25 Gb/s
No. of DSP slices	3600	320
Block RAM	54 Mb	10.7 Mb
Max. operational bandwidth	741 MHz	360 MHz

*Each DSP slice contains a 28x18 twos-compliment multiplier and a 48-bit accumulator.

LOs: local oscillators

2.3.2 Analog-to-digital converters (ADCs)

ADCs are also an integral part of the OBPs as depicted in Fig. 2-5. The first operation at the input of the OBP is the conversion of the channelized carriers into a digital data stream. This is accomplished by ADCs. The converted samples are represented by a specified number of bits which is determined by the acceptable amount of the quantization error and the dynamic range of signals [63]. A higher bit resolution of the digitized samples leads to a lower quantization noise, but also results in an increased design complexity and power consumption [31]. Practical HTS transponders are typically operating at several hundreds of megahertz of bandwidth. This means that the required sampling rates for the on-board ADCs can reach up to 1 GHz or higher [31,64]. Moreover, like the on-board FPGAs, the developments made in the on-board radiation hardened ADCs are also slow compared to the advancements made in the terrestrial counterparts.

Table 2.2: Typical characteristics of radiation hardened ADCs.

ADC Type	**No. of Bits**	**Max. Sampling Frequency/MHz**	**Power Consumption/mW**	**TID/ Krad**
ADC08D1000/NS	8	1000	1600	300
STS8388B/AT	8	1000	3400	1500
SPP/AU	12	5	500	100
AD9042/AD	12	41	545	300
AD6645/AD	14	105	1500	100
92040LP/MX	14	10	355	100
AD977A/AD	16+	0.2	100	100
7809LP/MX	16+	0.1	132	100

Table 2.2 presents the typical bit resolution, sampling rates, power consumption and total ionizing dose (TID) [60] values for some of the available radiation hardened ADCs. From the table, it can be seen that very high sampling rates are only supported for low resolution ADCs. Furthermore, as the bit resolution rises, the maximum achievable sampling rates become lower. This means that for HTS, high bit resolution ADCs (14+) cannot be yet envisioned. Table 2.2 also highlights the fact that for higher sampling frequencies and TID, the power consumption rises. Furthermore, the space-grade DACs also lag in performance, just like the on-board ADCs. Limitations

on the bit resolution, power consumption and supported maximum sampling rates affect the performance of the baseband signal processing algorithms implemented in the FPGAs. These effects will be discussed in the coming chapters.

2.4 High power amplification

HPA is one of the most critical active component of the payload [65, 66], and it follows the digitized section of the transponder (See Fig. 2-1). A typical RF HPA comprises of four key components: the main amplification module labeled as the power amplifier (PA) on Fig. 2-1 which provides the majority of the gain and RF output power, a low-level CAMP or driver amplifier to bring the total gain up in order to meet the over all HPA gain requirement, tuning and bias circuitry, and lastly a power supply to drive the required voltages and currents [66]. The details of the CAMP, technologies used to build the PAs, and the non-linear PA models are presented in the following.

2.4.1 Channel amplifier (CAMP)

A CAMP is installed in the transponder's HPA. It precedes the main power amplifier as shown in the Fig. 2-1. Losses incurred in the IMUX reduce the power level of the signal entering the channelized section of the transponder. This power level is generally insufficient to drive the channel output of the HPA. The CAMP provides the required power gain (20 to 50 dB). Fig. 2-6 presents a more detailed architecture of a CAMP. The CAMP contains an attenuator which allows adjustable gains. This helps compensate for the subsequent HPA gain variations over the satellite's life. Moreover, the attenuator also controls the IBO of the transponder's HPA. An automatic level control (ALC) is also embedded in the CAMP. ALC maintains a constant power level regardless of input power variations [67]. In addition, to keep the level of IMD noise low in the input and the output of the main PA, an analog linearizer [20] is also installed in the CAMP. The analog linearizer contains a circuit with a transfer function opposite to that of the main PA characteristics. For a given level of IMD noise, the linearizers can help reduce the operating IBO, i.e., increasing the overall

power efficiency of the payload.

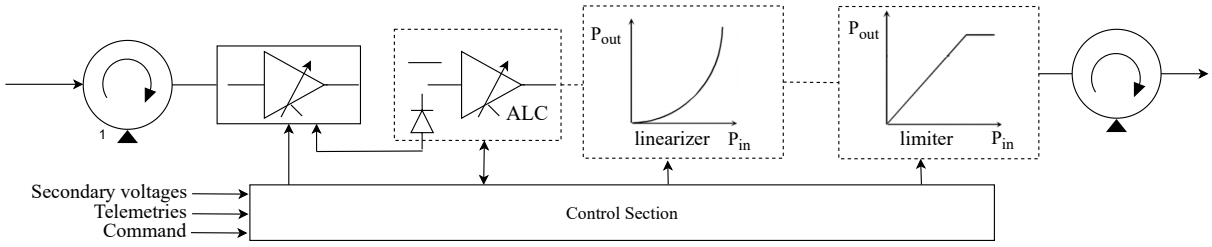

Figure 2-6: Channel amplifier (CAMP)(Thales Alenia Space).

2.4.2 Power amplifier module

The PA module is the main component of the HPA, and it provides the maximum gain which in turn determines the equivalent isotropic radiated power (EIRP). The operating point of the PA, i.e., IBO is set in the CAMP which in turn governs the resulting output power delivered to the carriers and the level of IMD noise. Two types of power amplifiers are employed in satellites: TWTAs and solid state power amplifiers (SSPAs) [66]. Typical characteristics of TWTAs and SSPAs are provided in Table 2.3.

Table 2.3: A summary of TWTA and SSPA characteristics.

Characteristic	TWTA	SSPA
Operating band (GHz)	L through Ka	L through Ka
Saturated power output (W)	20-250	20-50
Gain at saturation (dB)	55	70-90
DC to RF efficiency (%)	40-65	24-40
Mass (Kg)	1.5-5.5	0.5-2.0
Linearity:		
· Carrier to IMD ratio C/IMD (dB)	10-12	14-18
· AM/PM conversion (°/dB)(near saturation)	4.5-5	2-2.5

TWTAs have maintained an edge over the SSPAs in satellite payloads due to their higher DC-to-RF conversion efficiency. TWTAs can offer a DC-to-RF efficiency of 70% in Ku-band. On the other hand, SSPAs have become popular for power

[1] Isolator (a circulator with matched load).

requirements of up to 50W. Furthermore, SSPAs offer longer life times and lower mass compared to TWTAs [63]. In addition, when compared to TWTAs, SSPAs tend to be more linear, but TWTAs can exhibit similar linear characteristics through an addition of a linearizer embedded in the CAMP. Even though TWTAs and SSPAs offer some advantages and disadvantages, the final choice for a specific type of an amplifier is made based on the mission requirements and the total costs. But, due to their higher output power and efficiency, TWTAs are more popular in satellite payloads. This work does not focus on the technology employed in HPAs, but rather on the non-linear effects associated with their operation.

2.4.3 High power amplifier: non-linear effects

HPAs are non-linear in nature, and they consume a large amount of power [6,68]. Therefore, they should be operated as efficiently as possible. Although operating HPAs at a lower IBO leads to a higher power efficiency, but this also introduces non-linear distortions in the amplified signal. Chapter 1 already highlighted these non-linear effects. These effects can be divided in two categories.

1: The in-band distortions in the form of clustering and warping of the signal constellation [14, 26] . The non-linear ISI results in spreading of the received constellation into small clusters instead of discrete constellation points at the receiver. This effect is known as clustering, and it is depicted in Fig. 2-7b. In addition to clustering, the non-linear phase (AM-PM) characteristics of the HPA cause the received constellation to no longer lie on the original constellation lattice. This effect is called warping, and it can also be seen in Fig. 2-7b. Both clustering and warping are detrimental and severely degrade the system BER performance. In addition, both effects become significantly stronger for multicarrier signals and higher order modulation schemes [16].

2: The out-band distortions such as spectral regrowth lead to ACI and IMD noise. Fig. 2-7a explains and provides the mathematical expressions for the IMD ratio and ACPR. IMD ratio is a measure of the effect of non-linearity on a multicarrier signal, and it is defined as the ratio between the wanted tone power (P_{Sig}) and the

highest inter-modulation tone power (P_{IMD}) just outside the in-band. The ACPR is a measure of the degree of signal spreading into the adjacent channels. It is defined as the ratio of the signal power contained in the adjacent channel (P_{Adj}) to the signal power in the in-band (P_{Main}). Furthermore, the IMD products also cause a degradation in the antenna amplitude and phase weightings, leading to a deterioration in the antenna beam pattern and null depth [69].

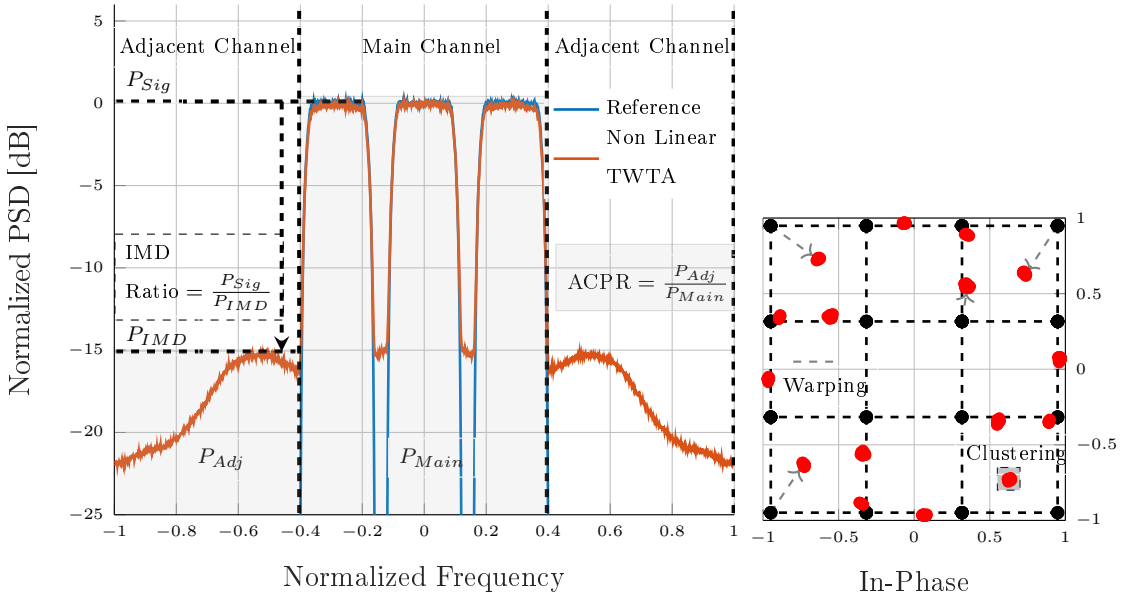

(a) Out-band distortions.

(b) In-band distortions.

Figure 2-7: The non-linear effect of HPAs, i.e., the in-band and out-band distortions.

2.5 HPA models

HPA models are required to analyze and compensate the non-linear HPA effects. Two approaches exist in modeling of HPAs, namely the physical modeling and behavioral modeling. First approach considers specific electronic elements to model the HPA, while the second approach performs modeling based on the HPA's response to different inputs [10]. This thesis focuses on behavioral models. They can be further classified into memoryless models or models with memory. To begin with, a model for an ideal amplifier is provided below.

$$y(t) = Gx(t), \tag{2.2}$$

where G is the desired gain in Volts, and $x(t)$ and $y(t)$ are the input and output of the amplifier, respectively (see Fig. 2-8). Note that the ideal amplification by the HPA implies that its output is a perfect replica of the input multiplied by a scalar gain value.

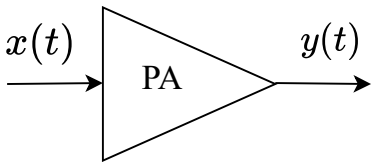

Figure 2-8: Input and output for PA.

2.5.1 Memoryless models

Since a practical HPA cannot behave ideally, non-linear models are needed. Non-linear memoryless models are applicable when HPAs are operated in narrowband. The parameters for these models are easy to estimate. However, memoryless models are frequency independent. Note that the input of the HPA $x(t)$ can also be written in polar coordinate system as $x(t) = A(t)\dot{e}^{j\varphi(t)}$, where $A(t)$ and $\varphi(t)$ are the amplitude and the phase of the input signal, respectively. A well-known method for PA characterization is the single-tone test [6,68,70], where the amplitude (AM-AM) and phase (AM-PM) distortions are measured with respect to different input power levels [68]. The output of a PA for the single-tone test can be written as

$$y\left(t\right) = g_{AM}\left(\left|x\left(t\right)\right|\right) \cdot e^{j\{\varphi(t)+\Phi_{PM}(|x(t)|)\}}, \tag{2.3}$$

where $g_{AM}\left(x\right)$ and $\Phi_{PM}\left(x\right)$ are the non-linear functions representing the AM-AM and AM-PM characteristics of the PA. $g_{AM}\left(x\right)$ characterizes the gain compression or expansion of the PA, while the $\Phi_{PM}\left(x\right)$ depicts the phase shift in the output signal. For memoryless models, AM-AM and AM-PM distortions are dependent only on the input's envelope, i.e., $\left|x\left(t\right)\right|$.

2.5.1.1 Polynomial model

A memoryless polynomial model can be used to model HPAs. The input-output relationship of the HPA using a memoryless polynomial is described as follows

$$y(t) = \sum_{k=1}^{K} w_k \cdot x(t) \cdot |x(t)|^{k-1}, \tag{2.4}$$

where w_k and K denote the complex-valued polynomial coefficients and the maximum polynomial order, respectively. The AM-AM and AM-PM characteristics can be modeled with a polynomial as well.

$$g_{AM}(|x(t)|) = \sum_{n=1}^{N_g} a_n |x(t)|^n \quad \text{(a)} \qquad \Phi_{PM}(|x(t)|) = \sum_{n=1}^{N_\Phi} b_n |x(t)|^n \quad \text{(b)}. \tag{2.5}$$

a_n and b_n are complex-valued. N_g and N_Φ are maximum polynomial degrees. The coefficients w_k, a_n and b_n are typically estimated by applying least-squares (LS), based on the applied input to the PA and the measured output of the PA. The polynomial model is linearly parameterized. This makes the estimation of the model coefficients low-effort and robust.

2.5.1.2 Saleh model

The memoryless Saleh model [71] is extensively used in literature to model PAs [72–74]. The following equations describe the AM-AM and AM-PM characteristics of the Saleh model.

$$g_{AM}(|x(t)|) = \frac{\alpha_{AM}|x(t)|}{1+\beta_{AM}|x(t)|^2} \quad \text{(a)} \qquad \Phi_{PM}(|x(t)|) = \frac{\alpha_{PM}|x(t)|^2}{1+\beta_{PM}|x(t)|^2} \quad \text{(b)}. \tag{2.6}$$

α_{AM}, α_{PM}, β_{AM} and β_{PM} are the four Saleh model coefficients. $g_{AM}(x)$ and $\Phi_{PM}(x)$ are the non-linear functions representing the AM-AM and AM-PM characteristics of the PA. The resulting output of the PA for the Saleh model is given by Eq. 2.3. The Saleh model can be used to represent a realistic TWTA in the forward path in a computer simulation, while the polynomial model can model the TWTA in the feedback path for implementing predistortion algorithms, when frequency independent behavior of the PA is considered.

2.5.1.3 Other memoryless PA models

Saleh model fits extremely well to model TWTAs, especially when the TWTAs are operated in narrowband. However, the Saleh model is not well suited to model SSPAs. SSPAs have a much smaller phase distortion. The Ghorbani model [75, 76] is often utilized to model SSPAs. The White model presented in [77] can model Ka-band (20-60 GHz) SSPAs.

2.5.2 Models with memory

When HPAs are operated in wideband applications, they exhibit memory effects, i.e., the HPA output not only depends on the current input, but also on the history of the input signal. The HPA models presented in Section 2.5.1 are unable to describe the frequency dependent behavior of HPAs, especially when the HPAs are operated in wideband. HTS utilize the wideband applications of HPAs. Extensive studies have been made to model the memory effects of power amplifiers [78–82]. The commonly used models are provided in the following.

2.5.2.1 Volterra model

One of the most accurate HPA model including the memory effects is the Volterra model [83, 84]. The following equation describe the discretized Volterra model in terms of the input and output of the PA.

$$y(n) = h_0 + \sum_{q_1=0}^{Q-1} h_1(n) \cdot x(n-q_1) \cdots + \sum_{k=2}^{K} \sum_{q_1=0}^{Q-1} \cdots \sum_{q_k=0}^{Q-1} h_k(q_1, \cdots, q_k) \cdot x(n-q_1) \cdots x(n-q_k). \quad (2.7)$$

$h_k[*]$ are the Volterra kernels of the k^{th} order and Q represents the maximum memory depth. Even though the Volterra series is an infinite series, for practical modeling purposes, it is truncated to a maximum non-linearity order (K) and memory depth (Q). Note that the number of kernels to be estimated rise exponentially with Q and K. This increases the computational complexity of the Volterra model, and makes it unattractive for HPA modeling. However, simplified versions of the Volterra model are often employed in practice where only selected kernels are used to model the HPAs.

A simplified Volterra model referred to as the memory polynomial (MP) model [85] is detailed in the next subsection.

2.5.2.2 Memory polynomial (MP) model

Memory polynomial (MP) model is a special case of the Volterra model, and it is composed of the diagonal Volterra kernels [81]. MPs are often utilized for HPA modeling [11, 12, 32]. Eq. 2.8 provides the input-output relationship.

$$y(n) = \sum_{q=0}^{Q-1} \sum_{k=1}^{K} w_{k,q} \cdot x(n-q) \cdot |x(n-q)|^{k-1}. \tag{2.8}$$

$w_{k,q}$ are the MP coefficients. The number of coefficients (KQ) in the MP model are significantly lower than in the truncated Volterra model given in Eq. 2.7. In order to improve the performance of the MP model, it is often implemented in conjunction with other cross terms (Volterra kernels) [81]. Taking both, the positive and negative cross terms, and combining them with Eq. 2.8 results in the generalized memory polynomial (GMP) model [85]. An advantage of the GMP model over the MP model is that it is more accurate, but GMP model is also computationally more complex. Moreover, estimating a larger set of coefficients, e.g., in Volterra or GMP model can lead to numerical stability issues [85]. Therefore, due to their low computational complexity and linearly parameterized coefficients, MPs will be extensively used to model PAs and predistorters in this work.

2.5.3 Summary: HPA models

Table 2.4 provides a summary of the discussed HPA models in terms of the number of coefficients, and their applicability in narrowband or wideband operation. As mentioned earlier, future HTS will mostly employ TWTAs due to their higher power levels and DC-to-RF efficiency. Therefore, depending on the narrowband or wideband operation of the HPAs, the Saleh model and MP model serve as the suitable candidates for HPA modeling due to their low computational complexity and wide popularity.

Q_nKM_n and Q_pKM_p represent the number of coefficients for the lagging and leading envelope in the GMP model.

Table 2.4: A computational complexity comparison of PA models: memoryless Vs. memory models.

	Number of Coefficients	Applicability
Memoryless Models		NarrowBand
Saleh	4	TWTA
Polynomial	K	TWTA/SSPA
Ghorbani	6	SSPA
White	4	SSPA
Memory Models		WideBand
Generalized Polynomial	$KQ + Q_nKM_n + Q_pKM_p$	TWTA/SSPA
Polynomial	KQ	TWTA/SSPA
Volterra	$>> KQ + Q_nKM_n + Q_pKM_p$	TWTA/SSPA

2.6 Multiport amplifiers (MPAs) in HTS

As discussed in Chapter 1, flexibility is another key requirement of the future HTS. MPA serves as an important flexible payload technology which provides an efficient use and allocation of the RF power. Apart from flexibility in power, MPAs also offer lower HPA design burden, reduced number of the redundant HPAs, and better DC power consumption [86]. Fig. 2-9 presents a single beam transparent payload architecture incorporating a MPA.

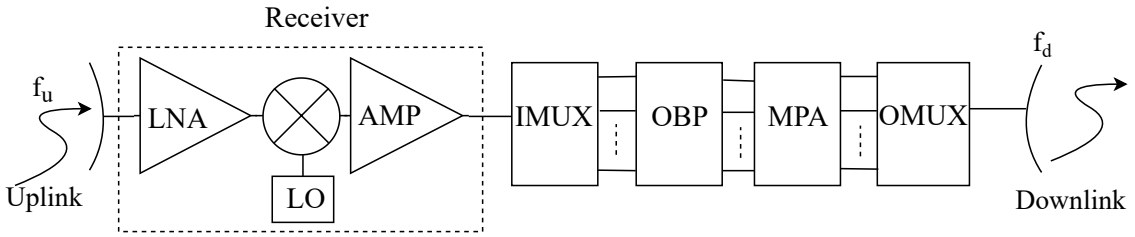

Figure 2-9: A transparent HTS transponder incorporating a multiport amplifier (MPA).

2.6.1 Structure of a MPA

A MPA is composed of three sections, i.e., an INET, a set of PAs, and an ONET. Fig. 2-10 presents a four-port MPA. The INET distributes the power of the input signals $x_i \; \forall i = 1 \cdots N_p$ equally, and with different predetermined phase shifts. N_p is the total number of ports. Then each amplifier operates on all the input signals contained within each of the INET output ports. In the conventional MPA model, the

amplification is linear, and with equal gains. The amplified signals are then fed to the ONET. The ONET phase-shifts and combines the amplified signals in such a way that each of the output port i provides only the amplified version of the input signal x_i after having been amplified by all the PAs [6]. Butler matrices have been widely applied to the INET and ONET. Butler matrices comprise of 3-dB couplers which distribute or combine the input signals at their output ports [87] with equal magnitude, but different phase relations. The amplifiers in MPAs are built with similar technologies presented in Section 2.4.2. As a result, same HPA models presented in Section 2.5 can be applied to model the amplifiers in MPAs. The complete mathematical model for the MPAs is discussed in the following.

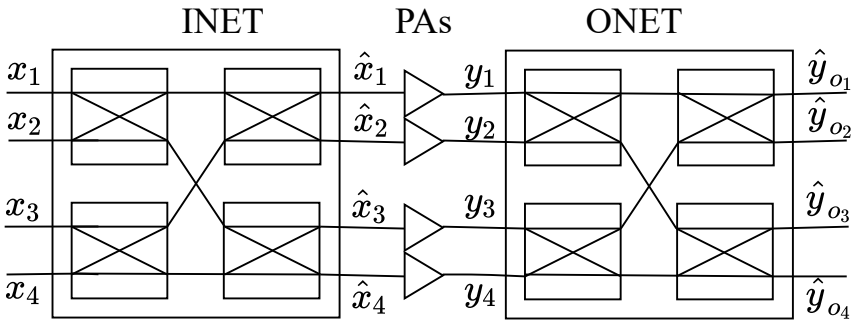

Figure 2-10: A four-port MPA.

2.6.2 Mathematical modeling of MPAs

The input-output relationship of the MPAs is dependent upon the assumptions made while modeling the INET, ONET, and PAs. Let $\mathbf{x} = [x_1\, x_2 \cdots x_{N_p}]^{\mathrm{T}}$ represent the input to the INET. Then the mathematical model for N_p-port MPA can be written as follows.

$$\hat{\mathbf{x}} = \mathbf{I}\mathbf{x}, \tag{2.9a}$$

$$\mathbf{y} = \mathbf{G}\hat{\mathbf{x}} = \mathbf{G}\mathbf{I}\mathbf{x}, \tag{2.9b}$$

$$\hat{\mathbf{y}}_o = \mathbf{O}\mathbf{y} = \mathbf{O}\mathbf{G}\mathbf{I}\mathbf{x}, \tag{2.9c}$$

where $\mathbf{I} \in \mathcal{C}^{N_p \times N_p}$ and $\mathbf{O} \in \mathcal{C}^{N_p \times N_p}$ are the INET and ONET butler matrices, while $\mathbf{G} \in \mathcal{C}^{N_p \times N_p}$ is the diagonal gain matrix for N_p HPAs. For ideal operation of the MPAs, two assumptions are made. First, that the INET and ONET must behave as

ideal phase shifters, i.e., they must be unitary matrices and conjugate transpose of each other. This means $\mathbf{IO} = \mathbf{OI} = I_{Np}$, where I_{Np} is an identity matrix. Second, the matrix $\mathbf{G}$ must not only be diagonal, but its entries g_i must be of the form $g_i = \mathrm{A}e^{j\theta}\,\forall i = 1 \cdots N_p$, i.e., linear and equal. An example of an ideal four-port INET and the gain matrix is given below.

$$\mathbf{I} = \frac{1}{2}\begin{bmatrix} 1 & j & -1 & j \\ j & -1 & j & 1 \\ -1 & j & 1 & j \\ j & 1 & j & -1 \end{bmatrix} \text{ (a)} \qquad \mathbf{G} = \begin{bmatrix} \mathrm{A}e^{j\theta} & 0 & 0 & 0 \\ 0 & \mathrm{A}e^{j\theta} & 0 & 0 \\ 0 & 0 & \mathrm{A}e^{j\theta} & 0 \\ 0 & 0 & 0 & \mathrm{A}e^{j\theta} \end{bmatrix} \text{ (b)} \tag{2.10}$$

If both of the assumptions are met, then the desired output of the MPA is achieved, given as follows.

$$\hat{\mathbf{y}}_d = \mathbf{G}\mathbf{x}. \tag{2.11}$$

2.6.3 MPA implementation issues

To achieve the desired MPA output given in Eq. 2.11, ideal INET and ONET, and linear HPAs with equal gains are required. However, in practice, it is difficult to meet these two assumptions. The problems which arise when these assumptions are not met are addressed below.

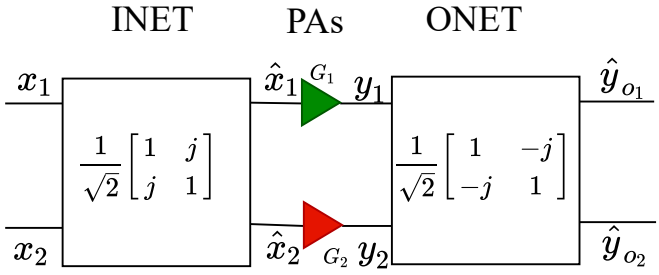

Figure 2-11: A 2-port MPA with unequal PA gains.

2.6.3.1 Unequal and non-linear HPA gains

In practice, HPAs exhibit non-linear gains and outputs. From Eq. 2.3, Eq. 2.6 (Saleh model) or Eq. 2.8 (Memory polynomial model), it is clear that the MPA output cannot be expressed as $\hat{y}_{o_i} = g_i x_i$, since $g_i \neq \mathrm{A}e^{j\theta}$ under non-linear conditions. Therefore making Eq. 2.9b, 2.9c, 2.10b and 2.11 invalid. Furthermore, from different

PA models discussed in Section 2.5, it is observed that often HPA output depends on the envelope of the input signal [30]. This not only leads to non-linear outputs, but unequal gains. Moreover, the resulting spectral regrowth and IMD noise limits the perfect reconstruction of the input signal at the output of the MPA, even if the INET and ONET are implemented accurately in the hardware. The following 2-port MPA example explains the effect of unequal power gains on MPA's output, even if linear operation with accurate INET and ONET is assumed. Fig. 2-11 presents the scenario. Note that the MPA model given in Eq. 2.9 is applicable as gains are assumed to be linear but unequal. The following equations hold for the 2-port MPA depicted in Fig. 2-11.

$$\text{INET Output} \quad \begin{bmatrix} \hat{x}_1 \\ \hat{x}_2 \end{bmatrix} = \frac{1}{\sqrt{2}} \begin{bmatrix} 1 & j \\ j & 1 \end{bmatrix} \begin{bmatrix} x_1 \\ x_2 \end{bmatrix} = \frac{1}{\sqrt{2}} \begin{bmatrix} x_1 + jx_2 \\ x_2 + jx_1 \end{bmatrix}, \tag{2.12a}$$

$$\text{HPA Output} \quad \begin{bmatrix} y_1 \\ y_2 \end{bmatrix} = \begin{bmatrix} G_1 & 0 \\ 0 & G_2 \end{bmatrix} \begin{bmatrix} \hat{x}_1 \\ \hat{x}_2 \end{bmatrix} = \frac{1}{\sqrt{2}} \begin{bmatrix} G_1 (x_1 + jx_2) \\ G_2 (x_2 + jx_1) \end{bmatrix}, \tag{2.12b}$$

$$\text{ONET Output} \quad \begin{bmatrix} \hat{y}_{o_1} \\ \hat{y}_{o_2} \end{bmatrix} = \frac{1}{\sqrt{2}} \begin{bmatrix} 1 & -j \\ -j & 1 \end{bmatrix} \begin{bmatrix} y_1 \\ y_2 \end{bmatrix} = \frac{1}{2} \begin{bmatrix} x_1 (G_1 + G_2) + jx_2 (G_1 - G_2) \\ x_2 (G_1 + G_2) + jx_1 (G_2 - G_1) \end{bmatrix}. \tag{2.12c}$$

From Eq. 2.12c, it is clear that when unequal HPA gains exist, the desired MPA output (Eq. 2.11) cannot be achieved due to the interference from all the other ports. Moreover, in this scenario, if $G_1 = G_2$, Eq. 2.12c becomes equal to Eq. 2.11, i.e., the desired MPA output.

2.6.3.2 Hardware imperfections in INET and ONET

Since the INET and the ONET are analog devices, they suffer from hardware imperfections, leading to ineffective Butler matrix operations. This causes port isolation problems [50], leakages to adjacent ports, unwanted power losses [88] and cross-talk between the MPA output signals. Moreover, 3-dB couplers used to implement the INET/ONET also suffer from insertion losses [6] which impact the over all MPA

power efficiency. Typically, several 2×2 3-dB couplers are connected together to implement larger INETs or ONETs e.g. 4×4 or 8×8. However, as the size of INETs and ONETs grows, so does the insertion losses and port leakages. The following presents a simple example of how the non-ideal behavior of a 2-port ONET leads to cross-talk between MPA output ports. Fig. 2-12 presents the scenario. A perfect INET and a linear HPA with equal gains is assumed. The two assumptions keep Eq. 2.9a and Eq. 2.9b valid for the scenario presented in Fig. 2-12. The output of ONET reads

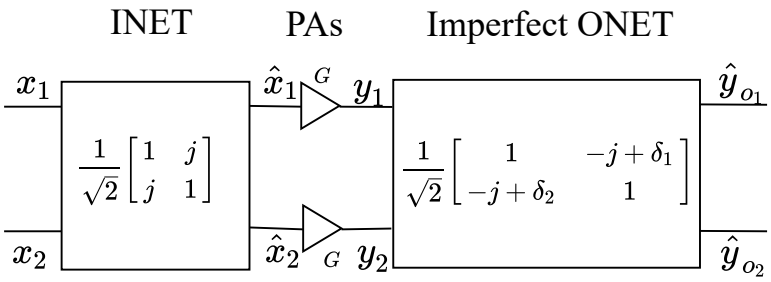

Figure 2-12: A 2-port MPA with an imperfect ONET.

$$\begin{aligned}\begin{bmatrix}\hat{y}_{o_1}\\ \hat{y}_{o_2}\end{bmatrix} &= \frac{1}{\sqrt{2}}\begin{bmatrix}1 & -j+\delta_1\\ -j+\delta_2 & 1\end{bmatrix}\frac{1}{\sqrt{2}}\begin{bmatrix}G\left(x_1+jx_2\right)\\ G\left(x_2+jx_1\right)\end{bmatrix}\\ &= G\begin{bmatrix}x_1\\ x_2\end{bmatrix}+\frac{G}{2}\begin{bmatrix}\delta_1(x_1+jx_2)\\ \delta_2(x_2+jx_1)\end{bmatrix}\end{aligned} \tag{2.13}$$

Eq. 2.13 shows that along side the desired MPA output, i.e., $\hat{y}_{o_i} = G_i x_i \forall i = 1 \cdots N_p$, cross-talk terms are also observed at the output ports. Note that in Eq. 2.13, the cross-talk terms are observed by modeling the imperfections in the ONET through additive distortion terms (δ_1,δ_2). However, cross-talk will still occur for other models (e.g. multiplicative) of an imperfect ONET as well. A novel two-step solution to overcome the non-linear effects of the PAs, and the imperfect INET and ONET will be detailed in the next chapter.

2.7 Summary

This chapter presented a transparent HTS payload architecture including an OBP. Different sections of the HTS payload including the receiver, multiplexing filters (IMUX and OMUX), OBPs, and HPAs were discussed in detail, and the technologies

used to build these components were also summarized. Moreover, the linear distortions introduced by the IMUX and OMUX filters in the form of memory effects were also presented. Furthermore, the non-linearities such as spectral regrowth, IMD noise and ACI introduced by the on-board HPA were discussed in detail too. In addition, different HPA models were also presented to analyze the non-linear HPA effects. In the coming chapters, these models will be applied in predistortion schemes to compensate for the distortions introduced by the on-board HPAs and the multiplexing filters. Lastly, in comparison to a single HPA per transponder, to improve the flexibility in terms of power, a HTS payload equipped with a multiport amplifier was presented as well. The next chapter details predistortion as a concept, and presents different kind of predistortion methods which can be used to compensate the non-linearities present in the system.

Chapter 3

Distortion compensation: predistortion

The previous chapter detailed the distortions associated with the non-ideal filters and non-linear HPAs employed in HTS payloads. This chapter discusses the different techniques for mitigating the presented linear and non-linear distortions. Equalization and predistortion are the two extensively researched and widely applied distortion compensation methods. This chapter focuses on the later approach, and will detail the different classes and methods of predistortion. Moreover, the class and type of predistortion best suited for HTS is also presented. The chapter also details a novel iterative direct learning architecture-based DPD technique. The proposed novel technique is also incorporated in a joint PAPR reduction and DPD scheme for 5G waveforms, and in a novel two-step scheme to overcome the non-linear effects of the HPAs, and imperfect INET/ONET in multiport amplifiers.

3.1 What is predistortion?

Predistortion (PD) aims at generating a distortion block whose transfer characteristics are an inverse to that of the transponder's HPA characteristics. As a result, the response of the cascaded predistortion and the HPA block is linear or close to being linear. Fig. 3-1 depicts the principle of predistortion. The predistorter is a non-linear block [89, 90], as a result, the spectrum of the complex-valued input signal $x(t)$ is

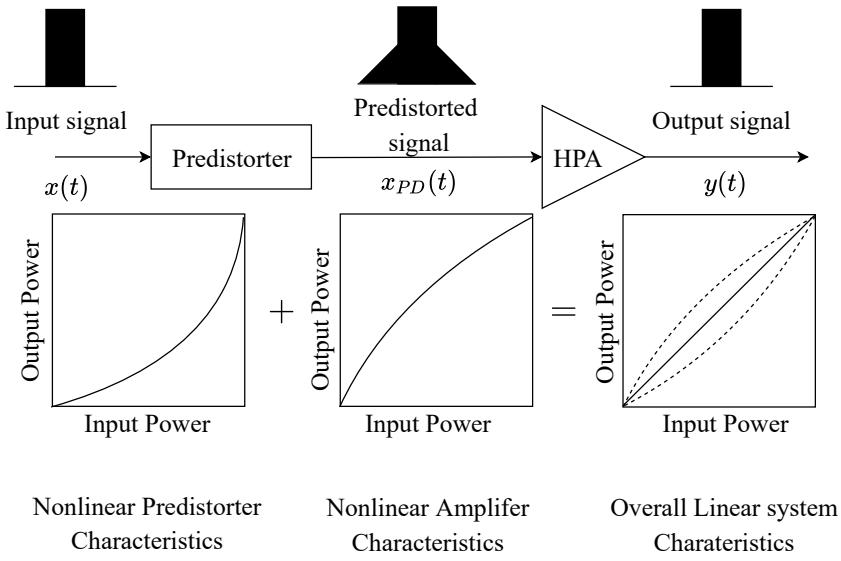

Figure 3-1: Linearization through predistortion.

expanded (see Fig. 3-1). The predistorter and HPA output for an ideal predistorter can be expressed as

$$x_{PD}(t) = p(x(t)) \tag{3.1}$$

$$y(t) = f(x_{PD}(t)) = f(p(x(t))) = \mathrm{G}x(t), \tag{3.2}$$

where G, $p(x(t))$, $f(x(t))$ are the desired HPA gain, and the non-linear transfer function of the predistorter and HPA, respectively. From Eq. 3.2, it clear that for an ideal predistorter, the resultant relationship between the normalized transfer characteristics of a predistorter and a HPA is given by

$$p(x(t)) = f^{-1}(x(t)). \tag{3.3}$$

3.2 Classes of predistorters

Predistortion can be classified according to two main criteria [91]. The type of signal which is modified before transmission (data or signal predistorters) and the applied technology (digital or analog predistorters).

3.2.1 Signal predistortion

Signal predistortion manipulates the pulse-shaped signal without accessing the underlying original constellation and data symbols [10]. Fig. 3-2a presents a sig-

nal predistorter. Signal predistorters can be employed either on-ground or on-board the satellite, and are typically placed just before the HPA. If signal predistorters are operated at baseband or an intermediate frequency (IF), then digital and adaptive implementations are also possible. Moreover, the CAMP of the payload's HPA normally contains an analog signal predistorter [20]. Some references for adaptive and non-adaptive signal predistorters are [11, 12, 20, 30, 92].

3.2.2 Data predistortion

Data predistortion manipulates the baseband data symbols, and it is only applicable in the digital domain. Fig. 3-2b presents a data predistorter. It modifies the baseband constellation symbols to mitigate the non-ideal filtering and non-linear amplification effects. Data predistortion is typically applied in on-ground stations. However, it can also be envisioned on-board the satellites in regenerative payloads, where the symbols are first recovered from the received RF signal using OBPs. Data predistortion can be adaptive or non-adaptive. Some references for data predistorters are [25, 33, 57, 93, 94].

3.2.3 Analog predistortion

Analog predistorters perform signal predistortion. They are built using analog components and are commonly placed just before the power amplifier [95]. Typically, analog predistorters invert the third or fifth order polynomial approximation of the HPA characteristics [10]. A frequently employed analog signal predistorter is a cubic predistorter [20]. It is composed of a pair of diodes, and a linear impedance. In addition, the analog predistorters have on-board applications, and are normally built in the CAMP of the payload's HPA [6]. However, analog predistorters are typically non-adaptive in nature.

3.2.4 Digital predistortion (DPD)

Digital data or signal predistortion is implemented using DSPs introduced in Chapter 2 Section 2.3.1. Unlike the analog predistortion, DPD offers accuracy and

Tx: transmit, Rx: receive.

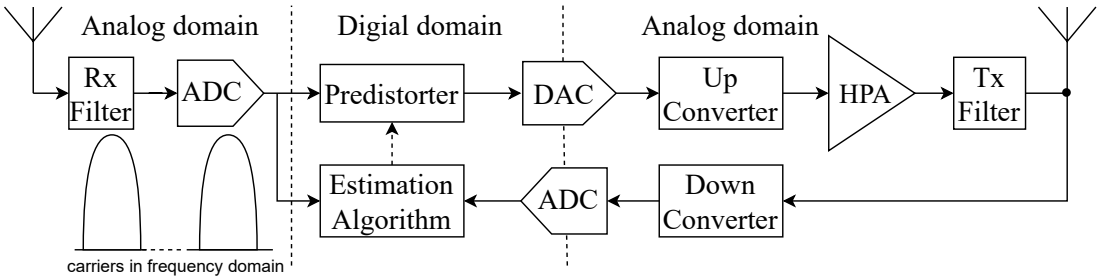

(a) Signal predistorter.

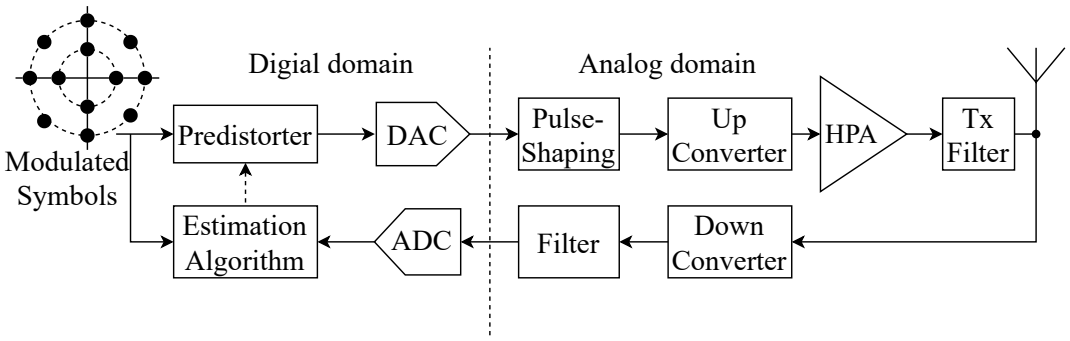

(b) Data predistorter.

Figure 3-2: The typical configurations of data and signal predistorters.

adaptive compensation designs. DPD is applicable either in on-ground stations [17,25] or in transponder's OBPs [30,96]. For DPD implementations, the sampling rates and resolution of the converters are of utmost importance, and they are usually selected based on the bandwidth of the signals and the acceptable amount of quantization noise allowed in the payload, respectively. Furthermore, the constraints on sampling rates and on the resolution of the converters are much stricter when on-board signal DPD is considered. This is because the less powerful on-board DSPs and converters available in the payload. Fig. 3-3 summarizes the technology used and the placement of the data and signal predistorters in a typical transmission chain.

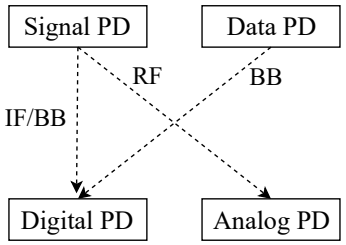

Figure 3-3: Classes of predistorters and their placement along the transmission chain (baseband (BB), intermediate frequency (IF), radio frequency (RF)).

Table 3.1: State-of-the-art predistortion techniques, and their suitability for HTS.

Technique	**Class**	**Employment**	**Complexity**	**Features**	**Performance**	**References**	**Suited for HTS**
Analog Cubic PD	Signal	on-ground on-board	Very low complexity: 2 to 3 coefficients	Non-adaptive Memoryless	degrades with time	[20]	on-ground: wideband narrowband **on-board: wideband narrowband**
Look-up tables (LUT)	Signal Data	on-ground on-board	High complexity: size of LUT grows exponentially with memory depth and modulation order.	Adaptive Memory Memoryless	increases with the size of LUT	Data: [33] Signal: [34]	on-ground: wideband narrowband on-board: narrowband
Neural networks	Signal Data	on-ground on-board	Very high complexity: extremely large number of DPD coefficients	Adaptive Memory Memoryless	depends on the activation function	Signal: [35] [36], [37]	on-ground: wideband narrowband on-board: narrowband
Successive interference cancellation	Signal Data	on-ground on-board	Medium-high complexity, iteration dependent, HPA/OMUX model required, feed-forward approach	Adaptive Memory Memoryless Near optimal gain	increases with number of internal iterations	Data: [25] [41]	on-ground: wideband narrowband
Volterra: pth-order inverse	Signal	on-ground on-board	High complexity: number of coefficients grow exponentially with order/memory, HPA model required	Adaptive Memory Memoryless	increases with memory and order	[38] [39] [40]	on-ground: wideband narrowband on-board: narrowband
Volterra: memory polynomials	Signal	on-ground on-board	Low-medium complexity MP: simplified form of Volterra, Direct and In-direct learning-based implementations	Adaptive Memory Memoryless	increases with optimal memory and order setting	In-direct: [11], [17] Direct: [97], [44]	on-ground: wideband narrowband **on-board: wideband narrowband**

3.3 Predistortion techniques

Last section summarized the different classes of predistorters. This section summarizes the different kinds of predistortion techniques which exist with in these classes. Table 3.1 presents the state-of-the-art predistortion techniques, and their suitability for HTS. The listed techniques are detailed in the following.

3.3.1 Analog cubic predistorter

Analog linearizer e.g., a cubic predistorter [20] is a solid solution for linearization, and is typically employed for linearizing TWTAs [22, 98] in satellite transponders. It provides a sound linearization gain in static operational conditions, i.e., fixed uplink signal characteristics. However, analog predistortion is not a practical solution for HTS where flexibility, performance accuracy, and adaptivity are of the utmost concern. In addition, the cubic predistorter is memoryless. Moreover, nowadays Doherty and envelope tracking [99] (ET) PAs dominate telecommunications. Systems employing these PAs almost universally employ DPD to maintain satisfactory linearity [22, 99]. Although, analog predistorters offers a cost effective solution, especially at very high bandwidths [22], but their non-adaptive and memoryless nature make them an impractical standalone solution for HTS. Fig. 3-5 details the need of adaptive DPD.

3.3.2 Look up table (LUT)-based approaches

A Look-up table (LUT) can be used to perform adaptive digital data or signal predistortion. A data DPD technique detailed in [33] utilizes LUTs to compensate for non-linear HPAs including the memory effects for QAM-based signals. In addition, LUTs can also be applied for signal DPD as suggested in [34]. Even though the LUT-based techniques can offer significant linearization performance [33, 34], but the size of LUTs grows exponentially with memory depth and modulation order [100]. This severely increases the computational load, power consumption and memory requirements, especially in OBPs where the computational power is limited. LUT based-DPD methods only offer practical solutions in narrowband operation of the

HPAs, i.e., when the memory effects can be ignored. Since the practical HTS systems implement wideband operation of HPA, LUT-based predistortion methods are not considered in this work.

3.3.3 Neural network (NN)-based approaches

Neural network (NN) is a parallel distributed information system which can be applied to approximate predistorters. A low-effort digital signal NN-based predistorter was presented in [35] which reported a linearity gain of up to 25 dB. However, the technique in [35] only considered memoryless non-linearities and zero loop delay, which is not ideal. The NN-based DPD techniques which compensate for the memory effects of HPAs are detailed in [36,37] and references within. [37] also presented a comparison between a truncated Volterra model-based DPD [101], a deep NN-based DPD [37], and a static NN-based DPD [36]. The proposed DNN-based approach in [37] achieves a very low adjacent channel power ratio (ACPR) of approximately -52 dBc. However, the DNN-based DPD requires 81,002 coefficients, while the implemented Volterra-based DPD method in [37] only needs 50 coefficients to achieve a similar ACPR performance [37, Table 2, Table 3]. [102] implements a bandlimited NN-based DPD for a signal with 40 MHz bandwidth. To achieve a low normalized mean squared error (NMSE) of -37 dB, 2217 to 3252 coefficients are needed [102, Table 1, Table 2]. [36] considers a memory of $Q = 3$ to maximize the gain while exhibiting a high computational complexity and power consumption. Due to the severe computational complexity and high power consumption exhibited by the NN-based approaches, they are impractical for on-board implementation where the processing power is limited due to radiation hardening requirements. In addition, the referenced NN-based DPD approaches do not cater for the memory effects introduced by the IMUX/OMUX. The Volterra-based predistorters are discussed in the coming Section 3.3.5.

3.3.4 Successive interference cancellation-based approaches

Successive interference cancellation (SIC) is also a compensation technique which mitigates the non-linear distortions and non-ideal filtering effects. The SIC-based

DPD (data or signal) is a feed-forward [103] approach with an open loop structure. State-of-the-art SIC-based digital data predistorters implemented at the gateway are detailed in [25, 41]. The DPD algorithm in [25, 41] can easily be extended to a signal-based DPD. Even though the SIC can offer low computational complexity and near optimal performance, but they are also not feasible for HTS as they are typically implemented as data (symbol) predistorters [25, 41]. Data DPD can either be implemented on-ground in gateways, or on-board in regenerative payloads. As discussed earlier, both scenarios are not in the scope of future HTS. In addition, SIC-based DPD methods are non-bandlimited in nature, require a large number of internal iterations, and their open loop structure is sensitive to loop maladjustments [42]. Thus rendering the approach impractical.

3.3.5 Volterra model-based approaches

The Volterra series [84] introduced in Chapter 2 Section 2.5 can also be used to implement signal and data DPD techniques. The two main architectures which are extensively utilized in the literature for Volterra model-based predistortion are the feedback loop-based direct learning architecture (DLA) and in-direct learning architecture (IDLA) [104]. In the feedback loop-based DPD approaches, a small portion of the HPA output is feedback to a DSP to adaptively compute the DPD coefficients. Although a feedback loop reduces the radiated power of the payload, however, this power loss can be minimized by using the state-of-the-art 40-50 dB couplers. Such couplers ensure that the power in the feedback signal is 40-50 dB below the radiated power. Fig. 3-4 presents the two different architectures. The IDLA-based DPD methods first adaptively identifies the post-inverse filter coefficients which are then copied to work as a predistorter. References [11] and [43] employ IDLA to implement DPD. On the other hand, the DLA-based DPD approaches first compute the HPA model adaptively. Then based on this digital HPA model, the DPD coefficients are computed. References [97] and [44] incorporate DLA for DPD. The DLA-based DPD methods are computationally more expensive and slower when compared to the IDLA-based DPD methods. However, a big draw back of the IDLA-based DPD

approaches is that the non-linear blocks are not permutable theoretically, i.e., computing a post-inverse and using it as a pre-inverse is not the optimal solution. Some of the widely researched Volterra series-based DPD methods are discussed below.

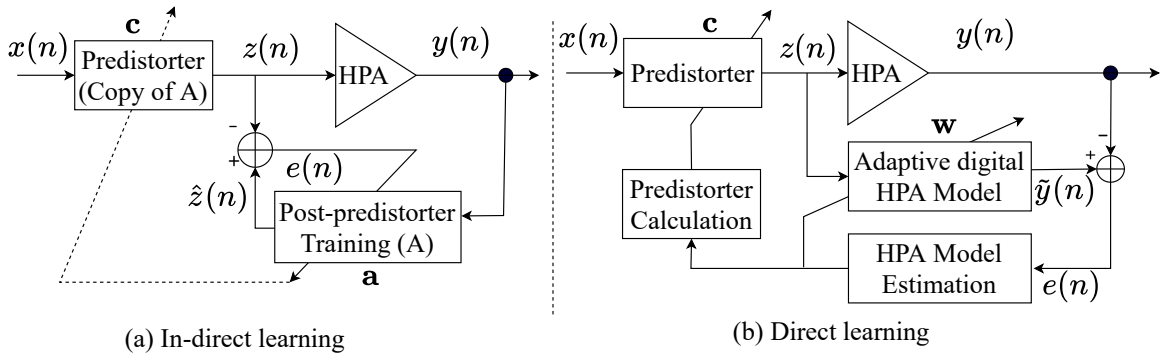

Figure 3-4: The direct and in-direct learning architectures for DPD.

3.3.5.1 *P*th-Order inverse predistortion

The *p*th-order inverse method [38, 39] implements a predistorter as a Volterra-system of a finite order P. These methods incorporate a DLA. Typically, the DPD methods involving the *p*th-order inverses require an estimation of a large number of coefficients (kernels), especially at higher orders and memory depths. For narrow-band operation of the transponder's HPAs and filters, i.e., when the memory effects can be ignored, this approach is feasible and can provide a significant gain in performance [40]. The number of the estimated DPD coefficients is low when memoryless DPD is implemented. However, HTS scenarios consider much larger bandwidths and a wideband operation of the HPAs, i.e., the transponder will exhibit memory effects. In terms of DPD this means computation of large number of DPD coefficients which can lead to computing delays. This makes the *p*th-order inverse approach impractical for implementation in OBPs. On the other hand, the IDLA and DLA-based polynomial approaches can outperform the *p*-th order inverse method as suggested in [26]. Furthermore, an exact inverse of a Volterra system is difficult to construct, and the *p*-th order inverse is only an approximation [11] [105]. The polynomial based approaches are introduced in the next subsection.

3.3.5.2 Memory polynomial (MP)-based predistortion

MPs were introduced in Chapter 2 Section 2.5.2 as a reduced complexity variation of the Volterra series. MPs are extensively used in the literature to implement signal DPD for the IDLA-based [11, 43] and DLA-based [44, 97] DPD methods. MPs are commonly applied in ground stations to implement signal DPD [17]. However, due to their low computational complexity and linear parametrization, MP-based DPD methods are also well suited for on-board DPD, especially in the wideband application of the transponders. Therefore, MP-based DPD is the main focus of this work.

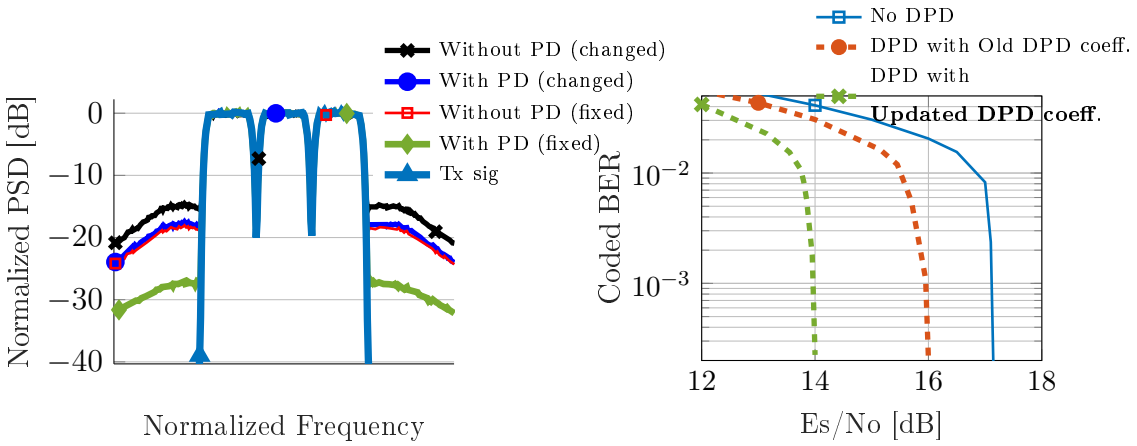

(a) Non-Adaptive analog linearizer.

(b) Analog PD: changed HPA.

Figure 3-5: The need for adaptive DPD with varying HPA and uplink signal characteristics.

3.3.6 Proposed predistortion techniques for HTS

Section 3.2 and 3.3 presented different classes and many different types of predistorters, ranging from analog to digital, on-ground to on-board, and non-adaptive to adaptive. This section proposes the class and type of the predistorter best suited for the HTS in author's opinion. Since future HTS will employ OBPs, only **on-board digital** predistortion schemes are suggested for implementation by the author in this work. Note that the complete information about all the carriers accessing the transponder is available on-board, and a single on-board digital predistorter can linearize the entire bandwidth of the HPA. In addition, since the future HTS employ transparent architectures, only **signal** DPD is considered by the author. It should be

noted that the on-board data DPD can only be implemented in regenerative payloads. Furthermore, the author only proposes **adaptive** on-board signal DPD implementations for HTS. Fig. 3-5 highlights the need and advantages of adaptive predistortion. Fig. 3-5a provides the linearization gain for a non-adaptive analog linearizer (the cubic predistorter [20]) when cascaded with a TWTA. Moreover, Fig. 3-5a also presents the linearization gain for the same analog linearizer when applied to a TWTA with slightly changed AM-AM/AM-PM characteristics. Note that a loss in linearization gain is observed when the analog linearizer is not updated adaptively according to the changed TWTA model. In addition to the HPA characteristics, the signal characteristics such as the ModCods, signal bandwidth, and number of carriers also determine the severity of the non-linear distortions added to the HPA output. Therefore, it is vital to also track changes in signal characteristics for optimal mitigation of the added distortions. Fig. 3-5b presents the BER curves for the middle carrier of a 16-APSK modulated 3-carrier signal for a system with an on-board DPD implementation. From Fig. 3-5b, a gain of 1.1 dB in Es/No is observed when an older set of DPD coefficients from a system of $N = 2$ carriers are applied to the new system of $N = 3$ carriers. However, when an updated set of DPD coefficients are applied (green curve), the gain is almost 3.1 dB. Thus indicating the need for adaptive DPD. Typically, a feedback loop architecture is required to implement adaptive DPD, where the HPA output is sampled and fed to the OBP. However, due to the constraints like power consumption and radiation hardening requirements, the bandwidth of the feedback path needs to be restricted. This allows the use of low sampling rate ADCs and FPGAs. Therefore, the author only proposes the more practical **bandlimited** DPD for HTS in this work. Fig. 3-6 summarizes the different traits of predistortion which should be considered for HTS. The Volterra-based MP DPD solutions meet all the criteria presented in Fig. 3-6, i.e, a **digital, signal, on-board, adaptive** and **bandlimited** implementation with **low computational complexity**. The next section details the mathematical framework for bandlimited MP DPD.

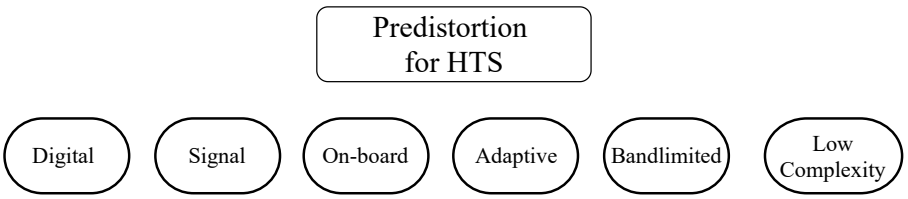

Figure 3-6: Predistortion for HTS: Algorithm characteristics.

3.4 Mathematical framework

Among the different DPD techniques presented in Section 3.3, the on-board MP-based bandlimited DPD was chosen by the author as the most suitable DPD approach for HTS. This section provides the mathematical framework for the state-of-the-art IDLA-based and a novel DLA-based MP DPD method implemented in this work. Fig. 3-4 depicts the two architectures.

3.4.1 In-direct learning architecture (IDLA)-based DPD

A MP-based DPD incorporating an IDLA is detailed in [11]. The mathematical description to compute the DPD coefficients is summarized in the following. Using MPs, the complex-valued DPD output (Predistorter block) in Fig. 3-4a reads

$$z\left(n\right)=\sum_{k=1}^{K}\sum_{q=0}^{Q}c_{kq}\left[x\left(n-q\right)\left|x\left(n-q\right)\right|^{k-1}\right], \tag{3.4}$$

where $x(n)$ and $z(n)$ are the DPD input and output, respectively. K and Q are the non-linearity order and the maximum memory depth of the predistorter, respectively. $c_{kq}\ \forall k=1\cdots K,\ \forall q=0\cdots Q$ are the MP model coefficients for the DPD. Let

$$\hat{x}(n,k,q)=x(n-q)\left|x(n-q)\right|^{k-1}, \tag{3.5a}$$

$$\hat{\mathbf{x}}_n=[\hat{x}(n,1,0)\ \ \hat{x}(n,1,1)\ \ \cdots\hat{x}(n,1,Q)\ \ \cdots\hat{x}(n,K,Q)]^{\mathrm{T}}, \tag{3.5b}$$

then the MP DPD model in Eq. 3.4 can be written compactly as

$$z\left(n\right)=\hat{\mathbf{x}}_n^{\mathrm{T}}\mathbf{c}. \tag{3.6}$$

For an input block with N samples, i.e., $\mathbf{x}=[x(0)\quad x(1)\ \cdots\ x(N-1)]^{\mathrm{T}}$, the MP model for the DPD output $\mathbf{z}=[z(0)\quad z(1)\ \cdots\ z(N-1)]^{\mathrm{T}}$ in matrix form reads

$$\mathbf{z}=\hat{\mathbf{X}}\mathbf{c}\ \ \text{where,}\quad \hat{\mathbf{X}}=[\hat{\mathbf{x}}_0\ \ \hat{\mathbf{x}}_1\ \ \cdots\ \hat{\mathbf{x}}_{N-1}]^{\mathrm{T}}, \tag{3.7}$$

where the entries of the $\hat{\mathbf{X}}$ are defined in Eq. 3.5a. Ideally, for a system presented in Fig. 3-4a $z(n) = \hat{z}(n)$, i.e., $e(n) = 0$, where $\hat{z}(n)$ is the output of the post-presditorter (A). Given the measured output of HPA $y(n)$ and the digitally computed DPD output $z(n)$, the task is to find out the parameters of the post-distorter block (A) which are then copied to the predistorter. It is assumed that the HPA non-linearity is invertible so that $e(n) = 0$. The output of the block (A) is given by

$$\hat{\mathbf{z}} = \hat{\mathbf{Y}}\mathbf{a}, \tag{3.8}$$

where $\hat{\mathbf{Y}}$ is defined the same way as $\hat{\mathbf{X}}$, and $\mathbf{a}$ are the MP coefficients of the post-distorter. At convergence, i.e., when $e(n) = 0$

$$\hat{\mathbf{z}} = \mathbf{z} = \hat{\mathbf{Y}}\mathbf{a} = \hat{\mathbf{X}}\mathbf{c}, \tag{3.9a}$$

$$\mathbf{c} = \mathbf{a}. \tag{3.9b}$$

Since, $\hat{z}(n)$ is linear in the parameters a_{kq}, the coefficients $a_{kq} \forall k = 1 \cdots K, q = 0 \cdots Q$ are computed based on the least-squares (LS), and are given as follows

$$\mathbf{a} = \mathbf{c} = (\hat{\mathbf{Y}}^H \hat{\mathbf{Y}})^{-1} \hat{\mathbf{Y}}^H \hat{\mathbf{z}}. \tag{3.10}$$

In this work, the above described methodology is made iterative to ensure that $e(n) = 0$ or is nearly zero. For the first iteration the DPD coefficients have a trivial solution, i.e., $\mathbf{c} = [1\, 0 \cdots 0]^{\mathrm{T}}$. For each subsequent iteration, the DPD output $z(n)$ is computed based on the updated DPD coefficients, and the respective output of the PA $y(n)$ is measured. Then $z(n)$ and $y(n)$ are used to estimate the DPD coefficients for the next iteration. Table 3.2 describes the algorithm.

3.4.2 Direct learning architecture (DLA)-based DPD

MPs can also be applied to DLAs. A DLA-based DPD method implemented in this work is detailed in the following. For DLA-based DPD, Eq. 3.4 through Eq. 3.7 are still applicable. Like the DPD block, the HPA block can also be modeled using MPs as follows

$$\tilde{y}(n) = \sum_{k=1}^{K} \sum_{q=0}^{Q} w_{kq} \left[z(n-q) \left| z(n-q) \right|^{k-1} \right], \tag{3.11}$$

In-direct learning-based DPD	Direct learning-based DPD
known parameters: $K, Q, I_{max}, \hat{\mathbf{X}}, \mathbf{y}$ **Initialization** $\mathbf{c}_{(0)BL} = \mathbf{1}$, **Iteration** $1 \leq i \leq I_{max}$: $\mathbf{z} = \hat{\mathbf{X}}\mathbf{c}_{(i-1)}$; $\mathbf{c}_{(i)} = (\hat{\mathbf{Y}}^H\hat{\mathbf{Y}})^{-1}\hat{\mathbf{Y}}^H\mathbf{z}$; $i = i + 1$;	known parameters: $K, Q, I_{max}, \hat{\mathbf{X}}_f, \mathbf{y}$ **Initialization** $\mathbf{c}_{(0)} = \mathbf{1}$, $\mathbf{z} = \hat{\mathbf{X}}\mathbf{c}_{(0)}$; $\mathbf{w} = (\hat{\mathbf{Z}}^H\hat{\mathbf{Z}})^{-1}\hat{\mathbf{Z}}^H\mathbf{y}$; $\mathbf{c}_{(1)} = (\hat{\mathbf{Y}}^H\hat{\mathbf{Y}})^{-1}\hat{\mathbf{Y}}^H\mathbf{z}$; **Iteration** $1 \leq i \leq I_{max}$: $\mathbf{z} = \hat{\mathbf{X}}\mathbf{c}_{(i)}$; $\tilde{\mathbf{y}} = \hat{\mathbf{Z}}\mathbf{w}_{BL}$; MSE(i)=MSE($\tilde{\mathbf{y}}, \mathbf{x}$); $\mathbf{c}_{(i+1)} = (\tilde{\mathbf{Y}}^H\tilde{\mathbf{Y}})^{-1}\tilde{\mathbf{Y}}^H\mathbf{z}$; $i = i + 1$; **Afters the Iterations**: [Index MMSE]=min(MSE(i)); $\mathbf{c}_{BL} = \mathbf{c}_{(\text{Index}),\text{BL}}$;

Table 3.2: Iterative solutions for MP-based DPD. MMSE: minimum mean squared error. $\text{MSE}(\tilde{\mathbf{y}}, \mathbf{x}) = \frac{1}{N}\sum_{n=1}^{N}(\tilde{y}(n) - x(n))^2$.

where $\tilde{y}$ is the estimated HPA output based on the HPA MP model coefficients w_{kq} $\forall k = 1 \cdots K$, $\forall q = 0 \cdots Q$. Using Eq. 3.5, the estimated HPA output per sample and for a block of N samples can be written as

$$\tilde{y}(n) = \hat{\mathbf{z}}_n^{\mathrm{T}}\mathbf{w}, \tag{3.12a}$$

$$\tilde{\mathbf{y}} = \hat{\mathbf{Z}}\mathbf{w}, \tag{3.12b}$$

where $\hat{\mathbf{Z}}$ and $\tilde{\mathbf{Y}}$ are defined in the same way as $\hat{\mathbf{X}}$. A simple procedure to obtain an estimate of the HPA model is to apply the DPD input $x(n)$ directly to the HPA input, i.e., by-passing the DPD block. This makes $z(n) = x(n)$. Then the HPA output is measured. The solution to Eq. 3.12b is also obtained through LS given as

$$\mathbf{w} = (\hat{\mathbf{Z}}^H\hat{\mathbf{Z}})^{-1}\hat{\mathbf{Z}}^H\mathbf{y}, \tag{3.13}$$

where $\tilde{\mathbf{y}}$ (estimated PA output) has been replaced by $\mathbf{y}$ (measured PA output) in Eq. 3.13. The HPA model coefficients $\mathbf{w}$ can be applied to compute the estimated HPA output ($\tilde{\mathbf{y}}$) in the OBP using Eq. 3.12b. Then the estimated HPA output ($\tilde{\mathbf{y}}$) along with the trivial DPD output ($\mathbf{z}$) can be used to obtain the first set of DPD coefficients using Eq. 3.10 . Different iterative procedures can be applied to reduce the mean

squared error (MSE) between the DPD input and the HPA output. A novel iterative process for the DLA-based DPD implemented in this work is described in Table 3.2. Sometimes LS-based inversions can be unstable, especially for larger or close to singular matrices. Moreover, at times LS may lead to a local optimum solution instead of a global optimum solution [106]. Therefore, in the proposed DLA algorithm, the computed DPD coefficients in each iteration are stored along with their respective MSE. Once the iterations are complete, the DPD coefficients exhibiting the minimum mean squared error (MMSE) are only copied to the predistorter. This ensures that the optimum DPD coefficients are selected for predistortion. Note that in Table 3.2, $\tilde{\mathbf{Y}}$ represents the estimated HPA output and $\hat{\mathbf{Y}}$ represents the measured HPA output in the feedback path.

3.4.3 Bandlimited predistortion for HTS

Section 3.3.6 emphasized on the need of not only adaptive but also bandlimited DPD algorithms for HTS. Fig. 3-7 presents the transponder architecture considered in this work for implementing the bandlimited MP DPD. Chapter 2 Section 2.2.3 explained the memory effects and the distortions associated with the OMUX filter. If the feedback signal is taken from the output of the OMUX instead of the HPA, then DPD with appropriate modeling can also mitigate the memory effects of the OMUX.

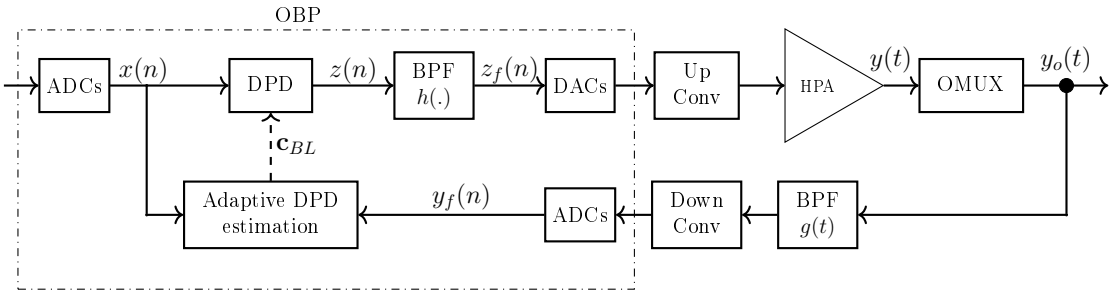

Figure 3-7: The transponder architecture for bandlimited, on-board, adaptive, signal DPD.

The OMUX filters out the spectral regrowth from the HPA output. Therefore, it inherently serves as a bandlimiting filter for the HPA output which is to be fed

Fig. 3-7 Up Conv: up-converter, Down Conv: down-converter

back to the OBP. Moreover, the bandwidth in the feedback path can be further restricted by using an analog BPF $g(t)$ to allow the use of more cheaper and less power consuming ADCs. Furthermore, since DPD is a non-linear operation, it also expands the bandwidth of the input signal (up to 5 times). However, the radiation hardened on-board DACs are not capable of sampling the entire signal bandwidth, especially in HTS scenarios where the sampling rate requirements can reach up to several GHz. As a result, a digital BPF $h(t)$ is employed in the forward path to bandlimit the DPD output as well. The bandwidth of the BPF $h(t)$ determines the band in which predistortion occurs. It is assumed that the ADC and DAC in Fig. 3-7 have sampling rates equal to atleast twice the passband bandwidth of $g(t)$ and $h(t)$, respectively. MP-based DPD solutions presented in Section 3.4.1 and 3.4.2 can be easily extended to incorporate the bandlimitation effects of the forward $h(t)$ and feedback $g(t)$ path filter. Using MPs, the bandlimited DPD output and the estimated HPA output in the OBP reads

$$z_f(n) = \sum_{k=1}^{K} \sum_{q=0}^{Q} c_{kq,BL} \left[\sum_{i=0}^{L} x(n-q-i) \left| x(n-q-i) \right|^{k-1} h(i) \right], \tag{3.14a}$$

$$\tilde{y}_f(n) = \sum_{k=1}^{K} \sum_{q=0}^{Q} w_{kq,BL} \left[\sum_{i=0}^{L_g} z_F(n-q-i) \left| z_F(n-q-i) \right|^{k-1} g(i) \right]. \tag{3.14b}$$

Note $\tilde{y}_f$ is the estimated bandlimited HPA output in the OBP, while y_f is the measured bandlimited HPA output in the feedback path. For compact representation of Eq. 3.14, the definitions in Eq. 3.5 are also updated by including the bandlimiting filters as follows

$$\hat{x}_{BL}(n,k,q) = \sum_{i=1}^{L} x(n-q) \left| x(n-q) \right|^{k-1} h(i), \tag{3.15a}$$

$$\hat{\mathbf{x}}_{n,BL} = [\hat{x}(n,1,0)\ \ \hat{x}(n,1,1)\ \ \cdots \hat{x}(n,1,Q)\ \ \cdots \hat{x}(n,K,Q)]^{\mathrm{T}}, \tag{3.15b}$$

$$\hat{z}_{BL}(n,k,q) = \sum_{i=1}^{L_g} z_f(n-q) \left| z_f(n-q) \right|^{k-1} g(i), \tag{3.15c}$$

$$\hat{\mathbf{z}}_{n,BL} = [\hat{z}(n,1,0)\ \ \hat{z}(n,1,1)\ \ \cdots \hat{z}(n,1,Q)\ \ \cdots \hat{z}(n,K,Q)]^{\mathrm{T}}. \tag{3.15d}$$

$\sum_{i=0}^{L_g} g(i)$ in Eq. 3.14b represents is finite approximation of the IIR filter $g(t)$.

In-direct learning-based DPD	Direct learning-based DPD
known parameters: $K, Q, I_{max}, \hat{\mathbf{X}}_f, \mathbf{y}_f$ **Initialization** $\mathbf{c}_{(0)BL} = \mathbf{1}$, **Iteration** 1≤i≤ I_{max}: $\mathbf{z}_f = \hat{\mathbf{X}}_f \mathbf{c}_{(i-1),BL}$; $\mathbf{c}_{(i),BL} = (\hat{\mathbf{Y}}_f^H \hat{\mathbf{Y}}_f)^{-1} \hat{\mathbf{Y}}^H \mathbf{z}_f$; $i = i + 1$;	known parameters: $K, Q, I_{max}, \hat{\mathbf{X}}_f, \mathbf{y}_f$ **Initialization** $\mathbf{c}_{(0),BL} = \mathbf{1}$, $\mathbf{z}_f = \hat{\mathbf{X}}_f \mathbf{c}_{(0),BL}$; $\mathbf{w}_{BL} = (\hat{\mathbf{Z}}_f^H \hat{\mathbf{Z}}_f)^{-1} \hat{\mathbf{Z}}_f^H \mathbf{y}_f$; $\mathbf{c}_{(1),BL} = (\hat{\mathbf{Y}}_f^H \hat{\mathbf{Y}}_f)^{-1} \hat{\mathbf{Y}}_f^H \mathbf{z}_f$; **Iteration** 1≤i≤ I_{max}: $\mathbf{z}_f = \hat{\mathbf{X}}_f \mathbf{c}_{(i),BL}$; $\tilde{\mathbf{y}}_f = \hat{\mathbf{Z}}_f \mathbf{w}_{BL}$; MSE(i)=MSE($\tilde{\mathbf{y}}_f, \mathbf{x}$); $\mathbf{c}_{(i+1),BL} = (\tilde{\mathbf{Y}}_f^H \tilde{\mathbf{Y}}_f)^{-1} \tilde{\mathbf{Y}}_f^H \mathbf{z}_f$; $i = i + 1$; **Afters the Iterations**: [Index MMSE]=min(MSE(i)); $\mathbf{c}_{BL} = \mathbf{c}_{(\text{Index}),\text{BL}}$;

Table 3.3: Iterative solutions for bandlimited MP-based DPD.

For a set of N observations of the input, the bandlimited DPD output and the bandlimited estimated HPA output in matrix form reads

$$\mathbf{z}_f = \hat{\mathbf{X}}_f \mathbf{c}_{BL} \quad \text{where,} \quad \hat{\mathbf{X}}_f = [\hat{\mathbf{x}}_{0,BL} \;\; \hat{\mathbf{x}}_{1,BL} \;\; \cdots \; \hat{\mathbf{x}}_{N-1,BL}]^{\mathrm{T}}, \tag{3.16a}$$

$$\mathbf{y}_f = \hat{\mathbf{Z}}_f \mathbf{w}_{BL} \quad \text{where,} \quad \hat{\mathbf{Z}}_f = [\hat{\mathbf{z}}_{0,BL} \;\; \hat{\mathbf{z}}_{1,BL} \;\; \cdots \; \hat{\mathbf{z}}_{N-1,BL}]^{\mathrm{T}}, \tag{3.16b}$$

where the entries of the matrices in Eq. 3.16a and 3.16b are defined in Eq. 3.15. The expanded forms of the matrices $\hat{\mathbf{X}}_f$, $\hat{\mathbf{Z}}_f$, $\hat{\mathbf{Y}}_f$ and $\tilde{\mathbf{Y}}_f$ are provided in Appendix A. Applying least squares, the bandlimited DPD and HPA coefficients are as follows

$$\mathbf{c}_{BL} = (\hat{\mathbf{Y}}_f^H \hat{\mathbf{Y}}_f)^{-1} \hat{\mathbf{Y}}_f^H \mathbf{z}_f, \tag{3.17a}$$

$$\mathbf{w}_{BL} = (\hat{\mathbf{Z}}_f^H \hat{\mathbf{Z}}_f)^{-1} \hat{\mathbf{Z}}_f^H \mathbf{y}_f, \tag{3.17b}$$

where $\hat{\mathbf{Y}}_f$ is defined in the same way as $\hat{\mathbf{Z}}_f$. Eq. 3.14-3.17 are applicable to both DLA-based and IDLA-based DPD. With an appropriate change of variables, the iterative procedures presented in Table 3.2 are applicable to bandlimited scenarios too. The updated iterative techniques are presented in Table 3.3. Note that in Table 3.3, $\tilde{\mathbf{Y}}$ represents the estimated HPA output and $\hat{\mathbf{Y}}$ represents the measured HPA

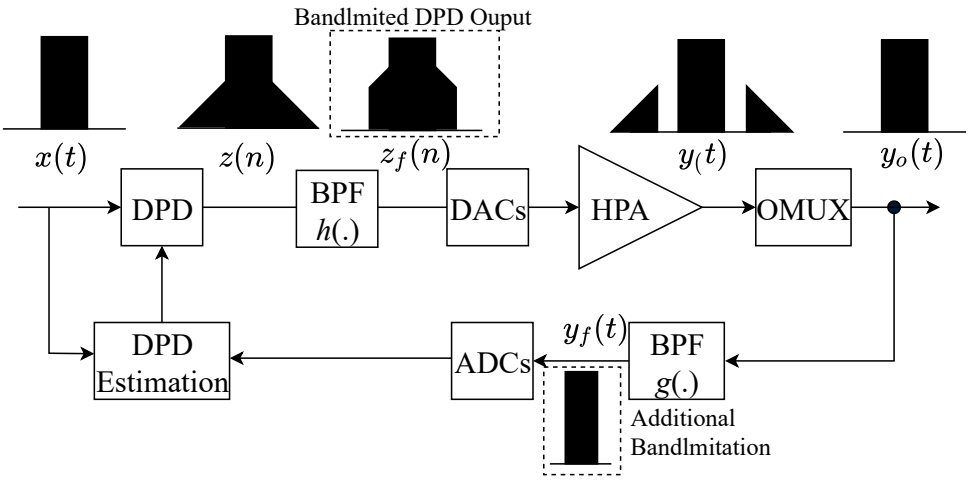

Figure 3-8: A spectral analysis for bandlimited DPD approach.

output in the feedback path. For a more clear understanding of the bandlimiting filters, a pictorial example of PSDs at the output of different blocks is presented in Fig. 3-8. The upcoming chapter will discuss the impact of the bandlimiting filters, i.e., $h(t)$ and $g(t)$ on the linearization performance of the presented DLA-based and ILDA-based predistorters. Moreover, the next chapter will also present the recovered gain in performance when the more complex novel DLA-based DPD is applied under severe bandlimitation constraints.

3.5 Applications of DPD

The presented bandlimited MP DPD methods have many applications. Even though the primary focus of this work is the identification of the parameters which effect the DPD performance. This work also presents two possible applications of DPD in HTS, i.e., DPD for MPAs, and 5G waveforms.

3.5.1 Linear and non-linear compensation for MPAs

MPAs were introduced as a flexible payload technology in Chapter 2 Section 2.6. Section 2.6.3 also highlighted the fact that the unequal and non-linear HPA gains due to the aging effects, and the imperfect INET/ONET due to the hardware imperfections, alter the desired MPA operation. To improve the performance of MPAs, this section details a novel two-step adaptive technique presented in author's origi-

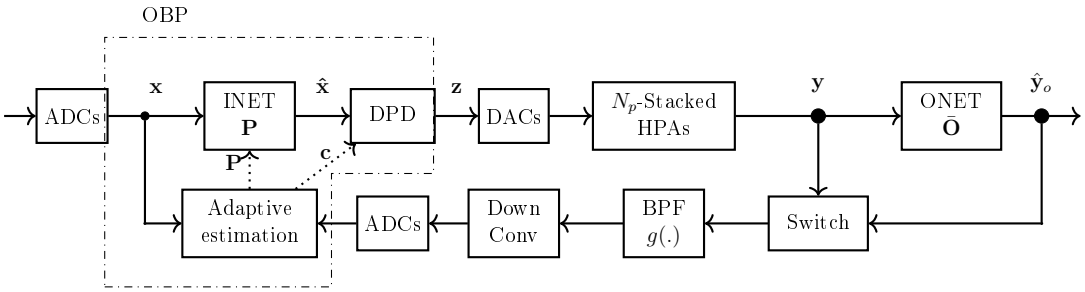

Figure 3-9: The proposed MPA model for the two-step compensation of imperfect INET/ONET and bandlimited DPD for non-linear HPAs.

nal paper [30]. In the first step, a novel on-board compensation technique for the imperfect INET/ONET is employed, and in the second step the novel bandlimited iterative DLA-based DPD is implemented against the non-linear amplification [96]. The transponder architecture implementing the proposed two-step approach is depicted in Fig. 3-9. The DPD block in Fig. 3-9 also includes a digital BPF $h(.)$. The mathematical framework for the two-step approach is detailed in the following.

Step 1: Imperfect ONET Compensation

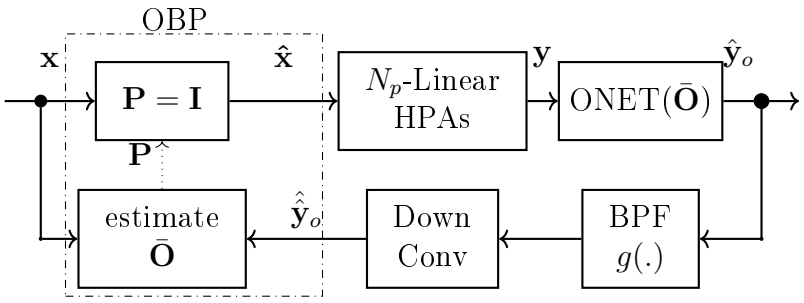

Figure 3-10: Step 1: estimating $\bar{\mathbf{O}}$ to compute the compensatory matrix $\mathbf{P}$.

This subsection details the step 1 which implements a novel digital INET in the form of a matrix $\mathbf{P} \in \mathcal{C}^{N_p \times N_p}$. $\mathbf{P}$ not only implements a perfect INET, but also compensates for the hardware imperfections in the ONET and unequal HPA gains existing in the MPA. The ONET is still built in the analog domain due to the higher power handling requirements. Fig. 3-10 presents the active parts of the proposed MPA model (Fig. 3-9) during the step 1. Note that the coupler, ADCs and DACs have not been drawn for the clarity of the figure (same for Fig. 3-11), but they do exist at their respective positions as indicated in Fig. 3-9. To obtain the compensation

matrix $\mathbf{P}$, it is assumed that the HPAs are operated in the linear region, therefore the DPD block can be bypassed. Operating HPAs linearly allows the basic MPA model of Eq. 2.9 (See Chapter 2 Section 2.6) to remain valid, even when the ONET imperfections exist. The feedback path bandwidth is set equal to the input signal ($\mathbf{x}$) bandwidth using the BPF employed in the feedback loop. The following set of equations hold in the model of Fig. 3-10.

$$\hat{\mathbf{x}} = \mathbf{P}\mathbf{x} \text{ (a)} \quad \mathbf{y} = \mathbf{G}\hat{\mathbf{x}} = \mathbf{G}\mathbf{P}\mathbf{x} \text{ (b)} \quad \hat{\mathbf{y}}_o = \bar{\mathbf{O}}\mathbf{y} = \bar{\mathbf{O}}\mathbf{G}\mathbf{P}\mathbf{x} \text{ (c)}, \tag{3.18}$$

where $\mathbf{G} \in \mathcal{C}^{N_p \times N_p}$ is a diagonal matrix, and the diagonal entries g_i can be unequal. Note that equations in (3.18) are similar to the equations in (2.9) with the analog INET ($\mathbf{I}$) replaced by a digital INET ($\mathbf{P}$), and a perfect ONET ($\mathbf{O}$) replaced by a real degraded ONET ($\bar{\mathbf{O}}$). Given that the matrix $\bar{\mathbf{O}}$ is known, the compensatory matrix $\mathbf{P}$ can be computed as follows. The desired output of the system irrespective of the imperfect ONET is still given by Eq. 2.11, i.e., ($\hat{\mathbf{y}}_d = \mathbf{G}\mathbf{x}$)., while the actual output of the system is $\hat{\mathbf{y}}_o = \bar{\mathbf{O}}\mathbf{G}\mathbf{P}\mathbf{x}$. By equating the actual output of the system (Eq. 3.18c) to the desired output (Eq. 2.11), i.e., $\mathbf{G}\mathbf{x} = \bar{\mathbf{O}}\mathbf{G}\mathbf{P}\mathbf{x}$, the compensatory matrix $\mathbf{P}$ can be computed as

$$\mathbf{P} = (\bar{\mathbf{O}}\mathbf{G})^{-1}\mathbf{G}. \tag{3.19}$$

Eq. 3.19 assumes that $\bar{\mathbf{O}}$ is known. However, since the analog components degrade over time, the imperfections in $\bar{\mathbf{O}}$ need to be computed adaptively. The model presented in Fig. 3-10 is again adopted. To calculate $\bar{\mathbf{O}}$, a feedback loop system is implemented, and the output of the degraded ONET ($\bar{\mathbf{O}}$) is inputted to the OBP, along with the input signal $\mathbf{x}$. However due to the measurement and the quantization noise, the feedback input signal $\hat{\hat{\mathbf{y}}}_o$ to the OBP contains measurement errors and can be expressed in the digital domain as

$$\hat{\hat{\mathbf{y}}}_o = \bar{\mathbf{O}}\mathbf{G}\mathbf{P}\mathbf{x} + \boldsymbol{\eta}_Q, \tag{3.20}$$

$$\hat{\hat{\mathbf{y}}}_o = \bar{\mathbf{O}}\underline{\mathbf{x}} + \boldsymbol{\eta}_Q, \tag{3.21}$$

where the $\boldsymbol{\eta}_Q$ represents the measurement noise and can be modeled as AWGN, and $\underline{\mathbf{x}} = \mathbf{G}\mathbf{P}\mathbf{x}$. Setting $\mathbf{P} = \mathbf{I}$, i.e., the perfect INET, estimating $\bar{\mathbf{O}}$ becomes a system

identification problem in the presence of noise where $\hat{\hat{\mathbf{y}}}_o$ and $\mathbf{x}$ are the measured and input signals, respectively. It should be noted that the system presented by Eq. 3.21 is an under-determined system as the number of unknowns ($N_p \times N_p$), i.e., the entries of $\bar{\mathbf{O}}$ exceeds the number of known variables (N_p the entries of $\underline{\mathbf{x}}$ and $\hat{\hat{\mathbf{y}}}_o$). To solve for $\bar{\mathbf{O}}$, at least N observations of the output are needed. However in the presence of noise, an over-determined system of equations is desirable to yield a more accurate estimate of $\bar{\mathbf{O}}$. Therefore, $M >> N_p$ observations are used to solve for $\bar{\mathbf{O}}$. For an over-determined system the following equation holds

$$\begin{bmatrix} \underline{x}_{1,1} & \underline{x}_{2,1} \cdots & \underline{x}_{i,1} & \underline{x}_{N_p,1} \\ \underline{x}_{1,2} & \underline{x}_{2,2} \cdots & \underline{x}_{i,2} & \underline{x}_{N_p,2} \\ \vdots & \vdots & \vdots & \vdots \\ \underline{x}_{1,M} & \underline{x}_{2,M} \cdots & \underline{x}_{i,M} & \underline{x}_{N_p,M} \end{bmatrix} \begin{bmatrix} \bar{\mathrm{O}}_{i,1} \\ \bar{\mathrm{O}}_{i,2} \\ \vdots \\ \bar{\mathrm{O}}_{i,N_p} \end{bmatrix} = \begin{bmatrix} \hat{\hat{y}}_{o_{i,1}} \\ \hat{\hat{y}}_{o_{i,2}} \\ \vdots \\ \hat{\hat{y}}_{o_{i,M}} \end{bmatrix},$$

$$\underline{\mathbf{X}}\bar{\mathbf{O}}_i = \hat{\hat{\mathbf{y}}}_{o_i}, \tag{3.22}$$

where $\underline{x}_{i,j}$ and $\hat{\hat{y}}_{o_{i,j}}$ represent the j^{th} observation at the i^{th} port, respectively. Furthermore, $\bar{\mathbf{O}}_i^{\mathrm{T}}$ is the i^{th} row vector of the degraded ONET matrix. To make sure that there are enough linear independent equations, the system is excited with an artificial un-correlated input signal $\mathbf{x}$. A least square (LS) solution can be applied to Eq. 3.22 to solve for the i^{th} row of the imperfect $\bar{\mathbf{O}}$. This results in

$$\bar{\mathbf{O}}_i = (\underline{\mathbf{X}}^H \underline{\mathbf{X}})^{-1} \underline{\mathbf{X}}^H \hat{\hat{\mathbf{y}}}_{o_i}, \tag{3.23}$$

where the solution of Eq. 3.23 is a row vector estimate of the respective real degraded ONET matrix row vector. LS-based solutions require pseudo-inverses to be computed. It is proposed to apply the QR decomposition method to obtain the pseudo-inverses as it leads to smaller rounding errors [107]. Note that the ONET ages slowly, therefore $\bar{\mathbf{O}}$ and $\mathbf{P}$ can simply be computed during the routine internet of things (IoT) measurements.

Step 2: Digital predistortion for Non-linear HPAs

The step two of the novel two-step compensation scheme is the implementation of DPD for the stacked PAs. For step two, the architecture depicted in Fig. 3-11

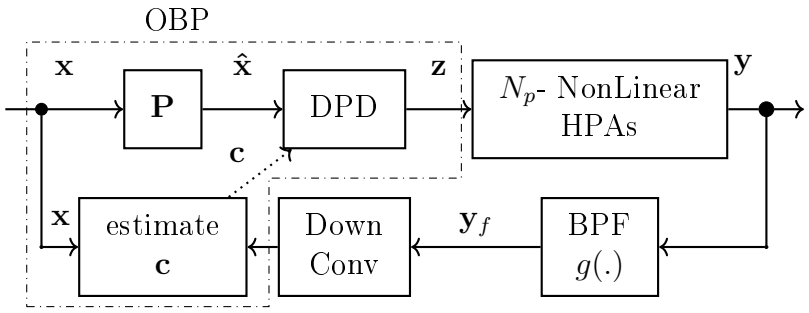

Figure 3-11: Step 2: computing the DPD coefficients with the updated **P**.

is adopted. Note that the coupler, ADCs and DACs have not been drawn for the clarity of the figure, but they do exist at their respective positions as indicated in Fig. 3-9. Once the compensatory INET **P** is updated in the MPA chain, then the DPD coefficients **c** can be updated adaptively during the normal satellite operation. The novel iterative DLA-based DPD technique is implemented in the second step. The DPD is detailed in Section 3.4.3 Table 3.3. For the presented bandlimited DPD approaches in Section 3.4.3, the feedback signal was taken from the output of the OMUX (See Fig. 3-7). Taking the feedback signal from the OMUX output mitigates the filter memory effects, through appropriate modeling of the predistorter. However, in the case of the MPAs, the feedback signal to implement the adaptive DPD has to be taken from the output of the HPA. This is because each output port of the ONET would only contain the amplified signal from a single input port of the INET, while each HPA amplifies a phase shifted combination of signals from all the input ports of the INET. This is depicted in Fig. 3-12 where a pictorial example of PSDs at the output of different blocks is presented for a 2-port MPA. To linearize the complete signal bandwidth accessing the HPA, the feedback back signal is taken from the output of HPA instead of the ONET. The BPF in the Fig. 3-11 serves as the bandlimiting filter. The DPD coefficients are recomputed and updated regularly during the normal operation of the satellite, unlike the compensatory matrix **P** which can just be updated during the service or downtime of the satellite.

Performance: two-step compensation method

The performance of the proposed two-step approach for different simulation configurations is presented in the following. For the provided results, the ONET is always

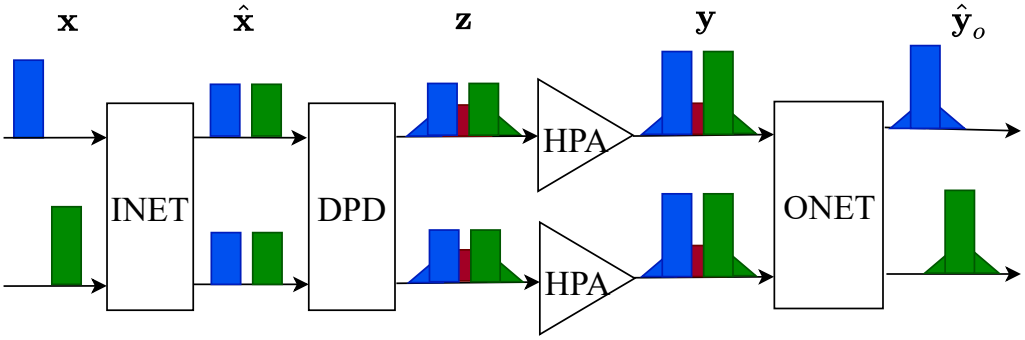

Figure 3-12: A PSD spectrum analysis for a 2-port MPA.

assumed to be imperfect, and the HPAs are always operated non-linearly. Different simulated configurations include: the compensation of both, i.e., the imperfect ONET and the non-linear HPAs, or compensation of only one of them. The simulated MPA transponder architecture is depicted in Fig. 3-9. $L = 8$-carrier signal is transmitted from the gateway to the satellite. A 4×4 MPA is considered ($N_p = 4$). This means $\frac{L}{N_p} = 2$ carriers access a single HPA. The modulation scheme used is QPSK. The feedback bandwidth is set equal to the OMUX BW, and an IBO of 8 dB is used. For the simulation purposes, the imperfections in $\bar{\mathbf{O}}$ are modeled as random deviations from the perfect ONET ($\mathbf{O}$), i.e., $\bar{\mathbf{O}} = \mathbf{O} + \Delta$, where $\Delta_{i,j} \sim \mathcal{N}(0, \sigma_d^2)$ as a worst case scenario. The results are provided for two different ONET distortion levels, i.e., $\sigma_d = \{0.05, 0.2\}$, which correspond to approximately -26 dB and -14 dB of inter-branch/port interference at the output of the MPA, respectively. The Saleh model [71] is used to represent the non-linear effects of the HPAs.

Fig. 3-13 presents the MPA's BER performance for two different σ_d. Depending on the severity of imperfect ONET distortions, different BER performances are achieved for the cases when the digital INET $\mathbf{P}$ is not used. For a higher degree of ONET imperfections, i.e., $\sigma_d = 0.2$, a much higher BER is observed when the compensatory INET $\mathbf{P}$ is not implemented. This means that for higher ONET distortions, DPD alone cannot reduce the BER as it only suppresses the intermodulation noise, while the interference due to the imperfect ONET still remains. However, when lower ONET distortions exist, i.e., $\sigma_d = 0.05$, performing DPD alone is sufficient to achieve near optimal BER performance. Nevertheless, the best BER performance is observed

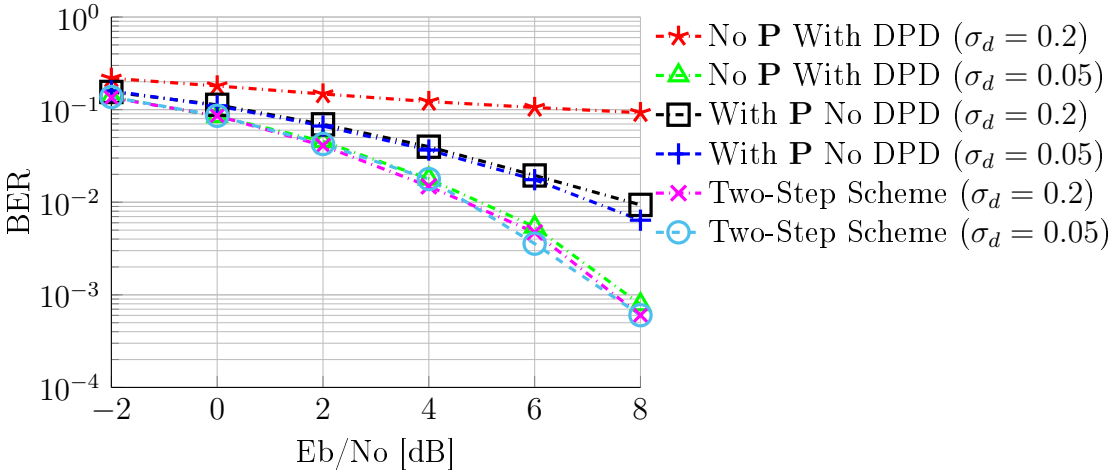

Figure 3-13: The BER performance analysis for two different $\sigma_d = \{0.05, 0.2\}$, i.e., inter-branch/port interference of -26 dB and -14 dB, respectively.

when both **P** and DPD are implemented together, regardless of the severity of ONET distortions. MPAs are a key technology for the future HTS. The proposed novel two-step approach can help achieve a significant improvement in the MPA performance, especially under the practical constraints presented in Chapter 2 Section 2.6.

3.5.2 Predistortion for 5G waveforms

As discussed in the introduction chapter, HTS will play an important role in the coming fifth generation (5G) of mobile communications. Therefore, for a smooth integration of satellite networks into the terrestrial ones, the standardization bodies are pushing for shared spectrum [4, 5]. Thus, the recent developments made in the terrestrial communication systems should also be analyzed for HTS systems. For example, the performance evaluation of the 5G New Radio (NR) waveform in HTS.

5G waveforms and PAPR: Some of the candidate waveforms that have been studied for 5G include the filtered orthogonal frequency division multiplexing (f-OFDM) [108], windowed orthogonal frequency division multiplexing (W-OFDM) [109], filter bank multicarrier (FBMC) [110], and universal filtered multicarrier (UFMC) [111]. These waveforms achieve low OOB emissions which significantly increases the spectral efficiency [112]. Furthermore, the analysis performed in [113] indicates that the f-OFDM is the most promising candidate for 5G NR networks. It is shown that

f-OFDM is a flexible multicarrier waveform which exhibits low OOB radiation while retaining most of the features of the legacy OFDM, and now is a part of the 5G standard. Nonetheless, all the aforementioned multicarrier waveforms including f-OFDM suffer from a high PAPR [114, 115]. This is because the closely packed multicarrier signals overlap, causing severe amplitude fluctuations. A higher PAPR leads to non-linear distortions in the HPA's output as it saturates the HPA. As discussed earlier, near saturation, the HPA output exhibits severe IMD distortions and OOB radiation.

Solution to high PAPR: The easiest way to keep non-linear distortions low is to operate the on-board HPA at a larger IBO. However, this reduces the power efficiency. PAPR reduction schemes can be applied to operate the HPA more efficiently in terms of power. Several PAPR reduction schemes exist in the literature such as selective mapping [116], partial transmit sequencing [117] and linear block coding [118]. However, these schemes increase the complexity of the transmitter and receiver, and require huge LUTs for encoding and decoding purposes [119]. Therefore, this work considers a much simpler and an effective PAPR reduction method known as signal clipping [51, 52] which can be directly applied on-board the satellite's transponder. The high peaks of the multicarrier signal are clipped before the signal passes through the HPA. However, clipping itself is a non-linear operation. It introduces in-band and OOB distortions which lead to a loss in spectral efficiency and BER performance. Filtering after clipping can reduce the OOB radiation, however it may cause some peak growth within the signal bandwidth which can increase the PAPR [120]. To counteract the effects of clipping and the on-board non-linear HPAs, this work proposes a combined on-board PAPR reduction and bandlimited DPD implementation for the aforementioned multicarrier waveforms. DPD not only linearizes the HPA, but also reduces the in-band distortions introduced by the signal clipping. The considered DPD method was presented in Chapter 3 Section 3.3.5, i.e., the novel iterative bandlimited DLA-based DPD approach.

3.5.2.1 Proposed transponder model for PAPR reduction and DPD

This section details the PAPR reduction technique and the DPD method implemented to linearize the HPA and remove the non-linear effects present in the satellite

communication chain. The presented joint PAPR reduction and DPD approach is detailed in author's original paper [121] and is briefly summarized in the following. Fig. 3-14 presents the satellite transponder model considered for PAPR reduction and DPD.

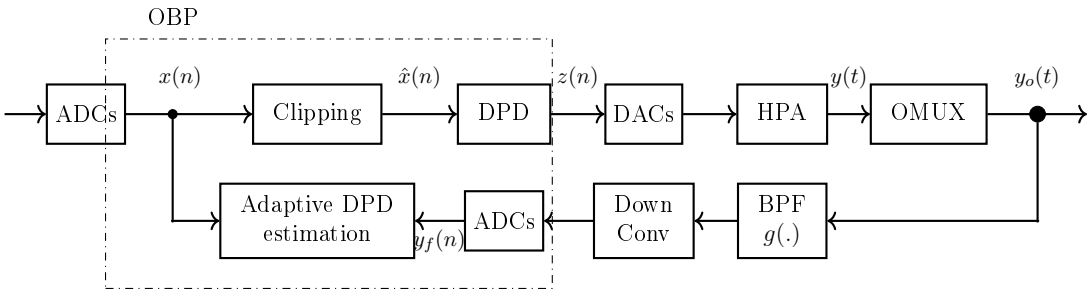

Figure 3-14: The proposed satellite transponder model for PAPR reduction (signal clipping) and DPD.

PAPR Reduction: signal clipping

PAPR is defined as the ratio between the peak power and the average power of the signal. The proposed PAPR reduction method is signal clipping. It is detailed in [52], and is briefly described here as well. The output of the clipping block is given as

$$\hat{x}(n) = \begin{cases} x(n) & \text{if } |x(n)| \leq \gamma^2 \\ \gamma^2 x(n) / |x(n)| & \text{if } |x(n)| > \gamma^2 \end{cases}, \tag{3.24}$$

where γ is the clipping parameter. A smaller value of γ implies a higher PAPR reduction. It should be noted that clipping does not change the phase of the signal, i.e. $\angle\hat{x}(n) = \angle x(n)$.

Predistortion: DLA-based DPD

The novel iterative DLA-based DPD presented in Table 3.3 is implemented to remove the non-linear effects introduced by the HPA and signal clipping. Note that a change of variables is needed in Table 3.3 to implement the DPD on the clipped signal, i.e., from $x(n)$ to $\hat{x}(n)$ in Eq. 3.14a. The updated iterative DLA-based DPD algorithm is presented in author's original paper [121, Table 1].

The DPD block in Fig. 3-14 also includes a BPF $h(.)$.

3.5.2.2 Performance: proposed PAPR reduction and DPD method

The performance results for the proposed PAPR reduction scheme in conjunction with the novel DLA-based DPD are presented in the following. The provided results are for f-OFDM multicarrier waveform. The simulated waveform has 20 MHz bandwidth (around the central carrier) consisting of 64 sub-carriers with a sub-carrier spacing of 312.5 KHz. A Sinc filter with a Hann time window is used as the filter in f-OFDM. Modulation schemes simulated are 4-QAM and 16-QAM. Moreover, no additional bandlimitation is considered in the feedback path, unless stated otherwise.

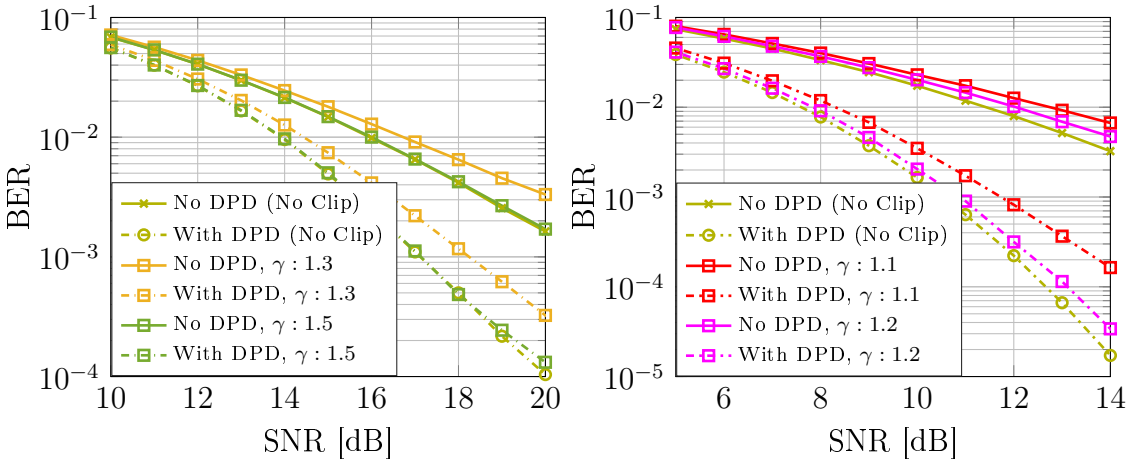

(a) Modulation: 16-QAM, OBO: 10.1 dB.

(b) Modulation: 4-QAM, OBO: 3.5 dB.

γ	**PAPR: No-DPD**	**PAPR-With DPD**
No Clip	10.1	11.8
1.3	4.9	5.4
1.5	7.1	7.9

(c) PAPR analysis, modulation 16-QAM.

γ	**PAPR: No-DPD**	**PAPR-With DPD**
No Clip	10.0	16.5
1.1	2.9	3.2
1.2	3.8	4.6

(d) PAPR analysis, modulation 4-QAM.

Figure 3-15: The BER and PAPR analysis for the proposed PAPR reduction and DPD method when implemented together, waveform: f-OFDM. Note All the values for PAPR are in dB.

Fig. 3-15 and Fig. 3-16 present the BER, PAPR, and PSD performance for the cases when the proposed PAPR reduction and DPD are implemented together using different clipping parameters γ. Fig. 3-15d and Fig. 3-15c provide the PAPR observed

BER results for the FBMC and UFMC waveforms exhibit similar trends, and are presented in the author's paper [121]. PAPR is measearued at the output of HPA, i.e., $y(t)$.

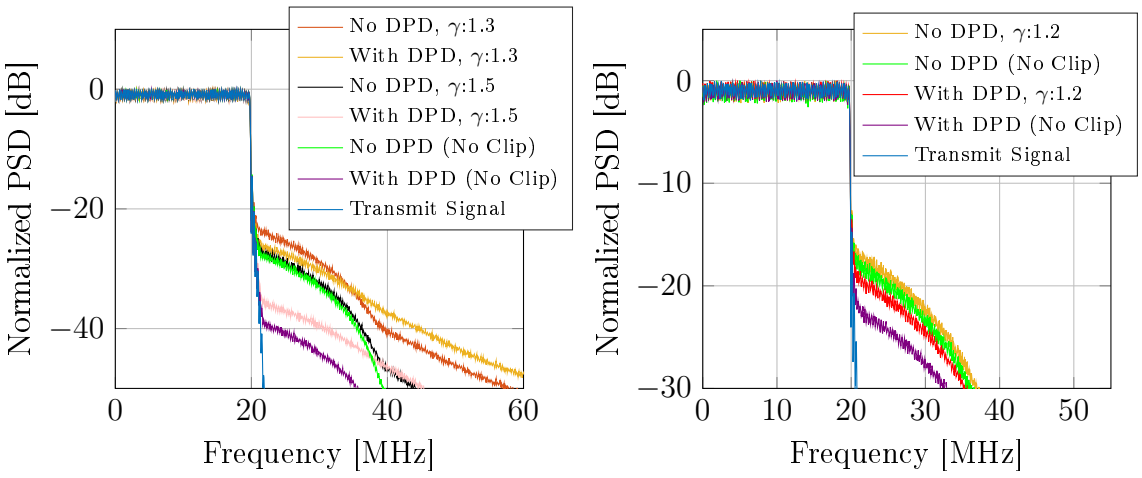

(a) Modulation: 16-QAM, OBO: 10.1 dB.

(b) Modulation: 4-QAM, OBO: 3.5 dB.

Figure 3-16: The PSD analysis for the proposed PAPR reduction and DPD method when implemented together, waveform: f-OFDM.

at different values of γ for the the BER analysis presented in Fig. 3-15, and the PSD analysis presented in Fig. 3-16. The respective OBO and modulation schemes are labeled on the figures. Best BER performance is observed for the case when no clipping is introduced and DPD is performed. DPD removes the non-linearities such as intermodulation noise, in-band and the OOB distortions, to provide a gain in BER. DPD implementation without clipping also implies maximum linearization performance. This can be observed in Fig. 3-16 which provides the PSD curves for the HPA output. However, this is an impracticable scenario, as the PAPR rises even further by 6.5 dB and 1.7 dB for 4-QAM and 16-QAM modulation schemes, respectively (see Fig. 3-15d and Fig. 3-15c). This is because, DPD is a non-linear operation itself. Therefore, clipping is introduced to reduce the PAPR, but this leads to a loss in BER performance. The lower the clipping parameter γ, higher is the PAPR reduction. However, a lower γ worsens the BER more, as more severe in-band and OOB distortions (see Fig. 3-16) are introduced. Nonetheless, when DPD is implemented along with signal clipping, the BER and linearization performance improves significantly and the increase in PAPR is rather minimal. Therefore, clipping can be performed to significantly reduce the PAPR, and DPD can be performed to remove the non-linear effects introduced by the clipping and the HPA.

3.6 Summary

This chapter presented the different classes of predistorters. Furthermore, the chapter also summarized different predistortion techniques existing within these classes e.g., methods based on LUTs, neural networks, successive interference cancellation, and Volterra model. Moreover, the chapter also proposed the class and type of predistorter best suited to HTS in the author's opinion. The adaptive on-board bandlimited signal MP-based DPD was the proposed method. The chapter also presented a novel iterative DLA-based MP DPD along with the state-of-the-art ILDA-based bandlimited MP DPD. The chapter also provided a mathematical framework for implementing DPD for MPAs and 5G waveforms. The novel DLA-based DPD was considered for both applications. Moreover, a significant gain in system performance was observed when the proposed DPD was implemented. The next chapter will present the novel system parameter identification and bandlimitation analysis for the proposed IDLA and DLA-based DPD.

Chapter 4

Numerical analysis

The last chapter presented the theory behind the considered IDLA-based and DLA-based DPD methods under the bandlimitation constraints. This chapter discusses the main findings of this thesis, i.e., the system parameter identification and the bandlimitation analysis. To this end, this chapter presents the simulation results of a thorough investigation made on the parameters which effect the performance of the proposed DPD methods. These parameters include the uplink signal characteristics such as ModCods and number of carriers, the order and memory of the DPD, and most importantly the sampling bandwidths in the forward and feedback path. Apart from identifying the key performance parameters and lowest possible sampling bandwidths, it is equally important to investigate the power consumption and hardware implementation requirements of DPD, especially on-board the satellite where resources are limited. Such an investigation can help fully understand the gains and feasibility of on-board DPD. Therefore, different aspects of DPD especially in terms of power consumption and computational complexity are also discussed in this chapter. The goal of the presented results and analysis is to not only identify the key performance parameters but also to highlight the scenarios where it makes sense to employ on-board DPD. Different performance metrics are utilized including the bit error rates (BERs), power spectral densities (PSDs), and total degradation (TD) [122]. TD serves as a complete metric to analyze the DPD gain achieved over

a given non-linear channel [122]. It is defined as

$$\text{TD[dB]} = \text{OBO[dB]} + \left[\frac{E_s}{N_o}\right]_{req}^{NL}\text{[dB]} - \left[\frac{E_s}{N_o}\right]_{req}^{AWGN}\text{[dB]}, \tag{4.1}$$

where $\left[\frac{E_s}{N_o}\right]_{req}^{NL}$ and $\left[\frac{E_s}{N_o}\right]_{req}^{AWGN}$ represent the symbol energy to noise density ratio required to achieve a target BER for the non-linear and linear (AWGN) channel. OBO is the output back-off, and is defined in Fig. 1-3.

4.1 System parameter identification analysis

Last chapter detailed the predistortion algorithms considered in this work and presented the need of digital adaptive DPD. This section presents some trends which can help identify the key parameters effecting the DPD gain.

4.1.1 Uplink signal parameters Vs. DPD gain

Uplink signal characteristics such as the modulation schemes, the forward error correction (FEC) code rates, and the number of carriers affect the DPD gain, and should be tracked adaptively. To study these effects, the IDLA-based DPD presented in chapter 3 section 3.3.5.2 is implemented without additional bandlimitation in the feedback path. For simulation purposes "no additional bandlimitation" refers to the case when the bandwidth (BW) of the feedback path filter $g(t)$ is set much larger (2 times or more) than the uplink signal BW. The simulated normalized non-linear HPA characteristics are defined in Fig. 1-3 given by the Saleh Model. The quadrature model equations [71] are used to implement the Saleh model. The simulated Saleh model coefficients are listed in [20, Table 3, TWT#1], and were estimated from an actual TWTA (Intelsat IV tube) measurement given in [98]. For the reader's ease, they are provided here too, i.e., $\alpha_p = 1.909$, $\alpha_q = 4.350$, $\beta_p = 1.075$ and $\beta_q = 2.335$. A 15% OMUX guardband is utilized, i.e., the OMUX 3-dB BW is 15% more than the uplink signal BW. The quantization effects of the ADCs/DACs and fixed-point-arithmetic (FPA) design of the digital components have not been considered in the presented results, and is left as a future work. Unless stated otherwise, the bandwidth of the forward-path DPD filter $h(t)$ is set to 1.5 times the uplink signal BW, and all the

carriers have equal power and equal symbol rates. It should be noted that although the HPA is modeled using the memoryless Saleh model, the transponder still exhibits memory due to the presence of IMUX and OMUX. The simulations are performed in Matlab where each block in Fig. 3-7 is modelled as an object-oriented block.

4.1.1.1 Number of carriers

The multicarrier operation of the transponder effects the DPD performance as depicted in Fig. 4-1a. The BER curve labels and OBOs for each scenario are plotted in Fig. 4-1b. It can be observed from Fig. 4-1a that when a multicarrier signal is uplinked to the HTS, the gain in BER performance is higher. This is because the multicarrier signals introduce IMD and ICI, leading to severe clustering and warping effects (see chapter 2 section 2.4.3). Moreover, the higher the number of carriers within the transponder BW, the more significant these effects are, and the more DPD has to compensate for. In addition, the mutlticarrier operation generates IMD products, and the HPA output power is shared between the useful carriers and the IMD noise [10] which effects the overall power efficiency. Moreover, intermodulation-tone power (P_{IMD}) rises with the number of carriers [69, Figure 2.17] which leads to a much higher loss in power. This effect can be observed in Fig. 4-1b, where multicarrier signals exhibit higher OBOs for each IBO, thus reducing the power efficiency.

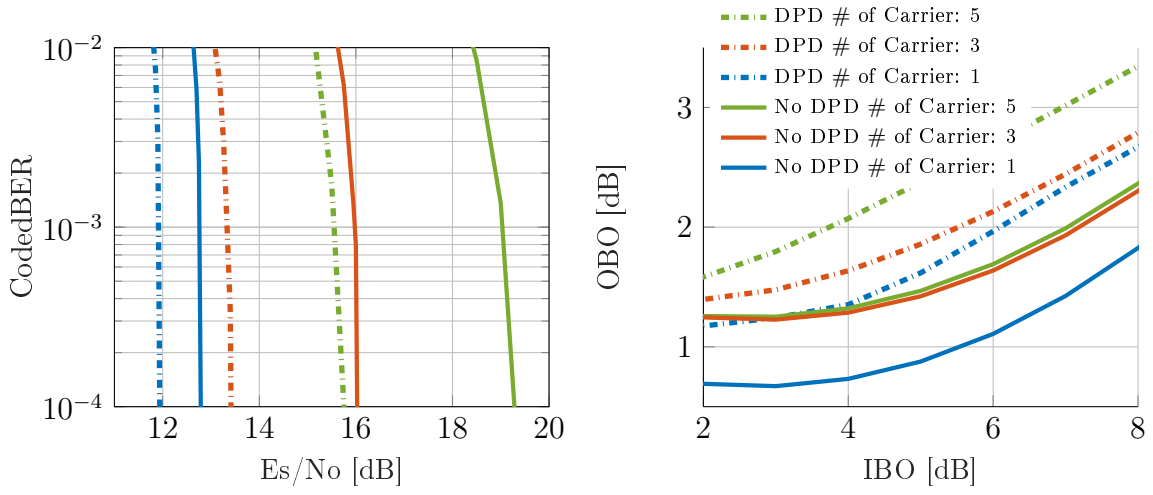

(a) Middle carrier, IBO 6 dB.

(b) Power efficiency.

Figure 4-1: Multicarrier operation Vs. DPD gain, DPD method: IDLA, modulation: 16-APSK, code rate: 5/6, Carriers: 3.

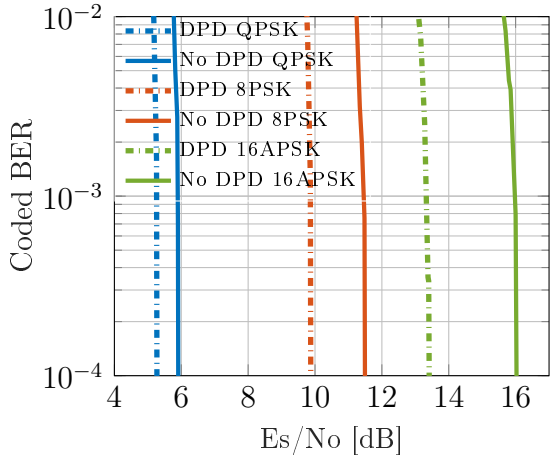

(a) Modulation Vs. DPD gain, **Middle carrier**, code rate (CR): 5/6, IBO: 6 dB.

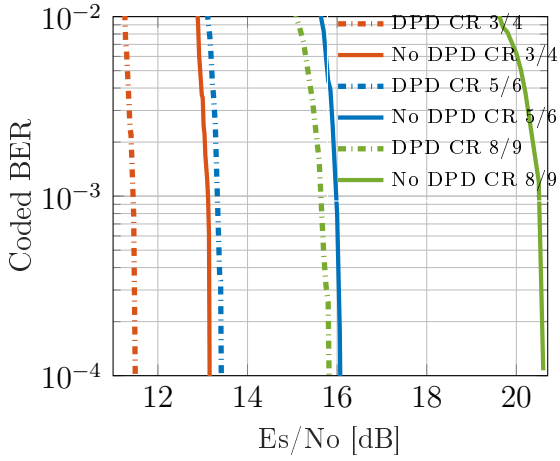

(b) Code rate Vs. DPD gain, **Middle carrier**, Mod: 16APSK, IBO: 6 dB.

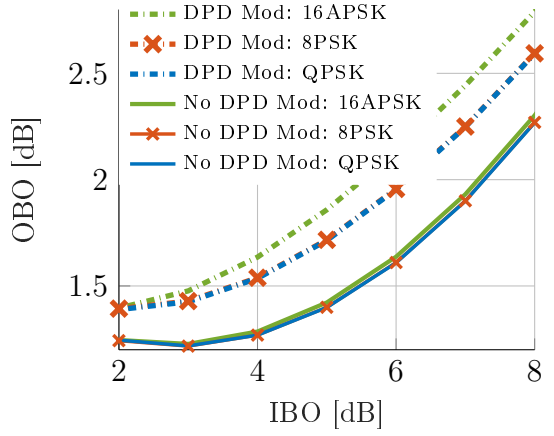

(c) Modulation Vs. power efficiency, code rate (CR): 5/6.

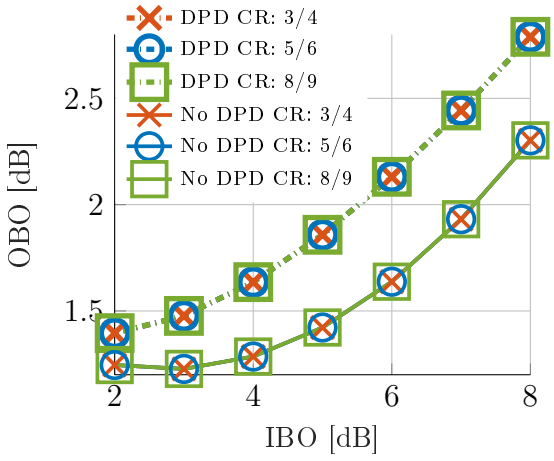

(d) Code rate Vs. power efficiency, Mod: 16-APSK.

Figure 4-2: ModCods Vs. DPD gain and power efficiency (OBO), DPD method: IDLA, Carriers: 3.

4.1.1.2 Modulation and coding rates (ModCods)

Modulation and coding rates (ModCods) also effect the DPD gain as depicted in Fig. 4-2a and Fig. 4-2b, respectively. The BER curves are plotted for an IBO of 6 dB, and the respective OBO for each scenario can be estimated from Fig. 4-2c and Fig. 4-2d. It can be seen from Fig. 4-2a and Fig. 4-2b that when a higher modulation order and a larger code rate is employed, the gain in BER performance is more significant, i.e., a higher DPD gain. The non-linear effects are higher at higher ModCods [16], as a result, the DPD has more to compensate for, thus leading to a

much larger gain. Furthermore, it is clear from Fig. 4-2c and Fig. 4-2d that the OBO is affected by the changes in modulation order but not the code rate. Moreover, the varying DPD gains due to changing uplink signal characteristics suggest the need for adaptive DPD. An example of the BER gain observed due to an adaptive DPD implementation was already discussed in section 3.3.6 (Fig. 3-5b). In addition, it should be noted that DPD leads to a rise in OBO (see Fig. 4-2c and Fig. 4-2d), but also reduces the SNR ($\frac{Es}{No}$) required to achieve a certain target BER. Therefore, for an over all gain in performance, DPD should only be considered for those scenarios where the rise in OBO is smaller than the gain in BER performance. Under these conditions DPD would lead to an overall reduction in TD. From Fig. 4-1 and Fig. 4-2, it is clear that DPD should be considered for higher ModCods and multicarrier scenarios. A multicarrier transmission leads to higher a bandwidth efficiency, and the higher ModCods increase the throughput. In addition, the varying DPD gains due to changing uplink signal characteristics also confirms the need for adaptive DPD.

4.1.2 Transponder parameters Vs. DPD gain

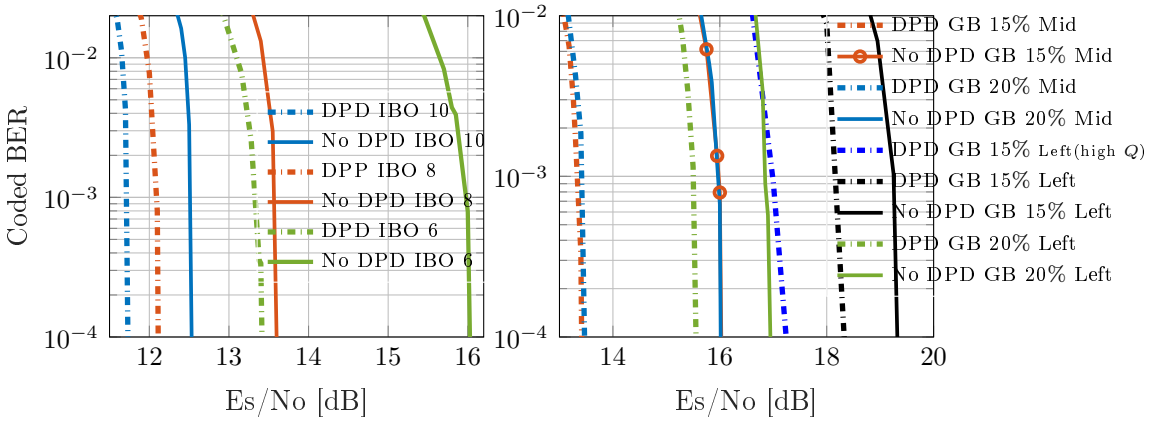

(a) Middle carrier, Operating point Vs. DPD gain.

(b) OMUX guard band (GB) Vs. DPD gain.

Figure 4-3: Transponder parameters Vs. DPD gain, DPD method: IDLA, modulation: 16-APSK, code rate: 5/6, Carriers: 3.

Transponder characteristics such as the transponder BW (OMUX BW) and the HPA's operating point also effect the DPD performance. It is clear from Fig. 4-3a that DPD leads to a higher gain in BER performance for an HPA operation closer

to saturation, i.e., a lower IBO. Note that a lower IBO operation introduces more severe non-linearities in the amplified signal. As a result, there is more for the DPD to compensate for. Thus employing DPD, especially closer to saturation not only provides a larger BER gain but also increases the power efficiency. In addition, the OMUX BW also effect the BER performance [41]. Fig. 4-3b presents the BER performance for two different OMUX BW with a guardband of 15% and 20%. From Fig. 4-3b, it is clear that the smaller OMUX BW (15% more than signal BW) introduces more severe distortions in the downlink signal, especially in the edge carriers, while the middle carriers remain more or less un-affected by the variable OMUX BW. This is because the group delay profile of the OMUX varies extremely at the edges, while it is flat in the middle (See Fig. 2-2). Nonetheless, DPD provides a gain for both the middle and the edge carrier. Note that for a tighter OMUX BW, a higher DPD memory (Q) is needed to achieve a comparable gain to a relaxed (wider) OMUX BW scenario. The effects of memory on DPD performance will be discussed in more detail in the following sections. From Fig. 4-3, it is clear that when implementing DPD, the OMUX BW and the operating point should be kept in mind among the key parameters affecting the DPD performance.

4.1.3 Predistortion algorithm parameters Vs DPD gain

Predistortion algorithm specific parameters such as the memory and order, and the learning architecture also effect the linearization performance. The following presents the simulation results of employing different learning architectures and varying the order and memory for the proposed MP-based DPD methods. Typically, to maximize the DPD gain, the order and memory of the predistorter should match the maximum non-linearity order and memory of the HTS transponder. Table 4.1 lists the fixed parameters for simulation results presented in this section. Unless stated otherwise, no additional bandlimitation in the feedback path is considered. Moreover, the DPD filter in the forward path has a bandwidth of 111 MHz which is 1.5 times more than that of signal BW. This mean that bandlimitation is considered in the forward path. In addition, all the carriers have equal power and symbol rate, the OMUX guardband is 15%.

Table 4.1: The fixed simulation parameters for DPD parameters and bandlimitation analysis.

Parameter	Value
Modulation	16-APSK
Code rate	5/6
Carriers	3
Signal BW	74 MHz
OMUX BW	85.1 MHz

4.1.3.1 Memory

The filter IMUX/OMUX and the HPA introduce memory effects which can lead to a reduced system BER performance. DPD with appropriate modeling can compensate for the memory effects introduced by the transponder filters and the HPA. Fig. 4-4 presents the TD performance of IDLA-based DPD for different memory depths. It can be observed from Fig. 4-4a that when the memory (Q) is increased from 0 to 10 there is a reduction in TD and the optimal OBO for the middle carrier. However, if the memory depth (Q) is increased significantly ($Q = 20$), the TD rises, i.e, DPD performance suffers. This could be due to the fact that at higher memory depths, the larger size of the matrix to be inverted can create numerical problems, leading to in-accurate inversions in Eq. 3.17. For a typical OMUX, the carriers in the middle are least affected by the memory effects, hence large memory depths of DPD are not required. Even a memory $Q = 0$ provides a reduction in TD for the middle carrier. However, the edge carriers suffer from more severe memory effects, hence DPD with $Q = 0$ leads to a poor performance as depicted in Fig. 4-4b. A reduction in TD is also observed for the edge carrier when the memory is increased. In addition, increasing the memory eventually saturates the DPD performance (See Fig. 4-4b). This is because increasing the DPD memory beyond a certain point would only lead to minimal or no gain, as all the memory effects introduced by the HPA and the transponder filters would have already been compensated for. Also note that the reduction in TD is more significant for the middle carrier. This is because the middle carrier suffers from more severe non-linear effects such as ICI or IMD noise which can be greatly reduced when DPD is implemented. Note that memory also influences the computational load on the OBP. A higher memory of DPD implies

larger matrix inversions which requires more computational power and can lead to computing delays.

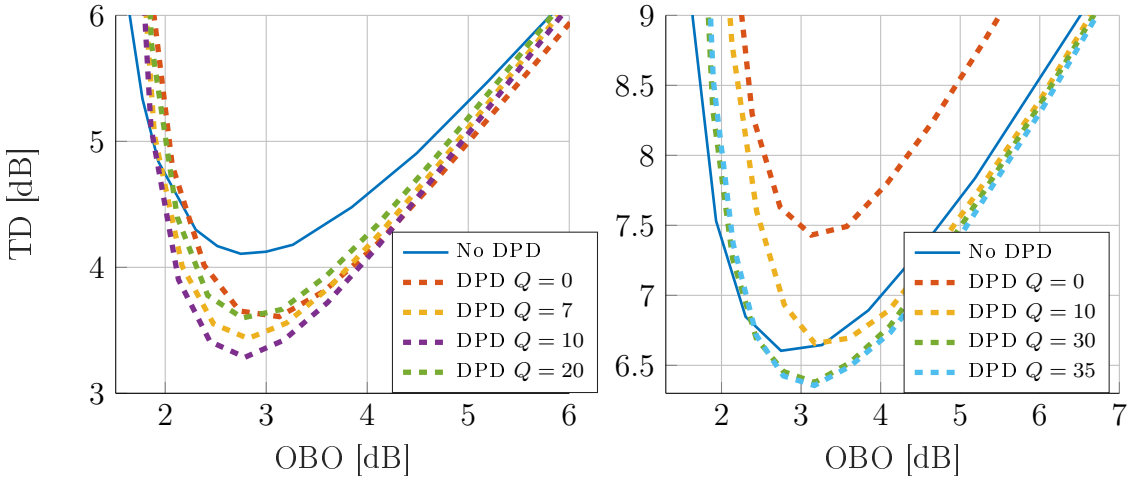

(a) Middle carrier.

(b) Edge (left) carrier.

Figure 4-4: Effect of memory (Q) on DPD performance, DPD method: IDLA. $K = 3$.

4.1.3.2 Order

Along side the memory, the order also effects the DPD gain. Typically, for stronger HPA non-linearities, a higher order (K) of the DPD is required. Fig. 4-5 presents the TD performance of the IDLA-based DPD for different orders (K). Fig. 4-5 exhibits a slight gain in performance when the order of the DPD is increased from 3 to 5 indicating that some 5^{th} order non-linearities are present in the system. Moreover, the performance suffers in terms of power efficiency when the order is increased to 7 (a higher optimal IBO, see Fig. 4-5a). This could be attributed to the fact that the larger size of the matrix to be inverted can create numerical problems, leading to in-accurate inversions in Eq. 3.17. However for the current simulation setup, it is clear that the order $K = 3$ for the DPD is sufficient. Also, a lower order reduces the computational complexity of the DPD which is an added benefit, especially in on-board DPD applications where the computational power is limited. It is clear from Fig. 4-4 and Fig. 4-5 that memory plays a more key role in DPD performance when compared to the order of the predistorter. Nonetheless, both parameters should be kept in mind when implementing and optimizing DPD performance.

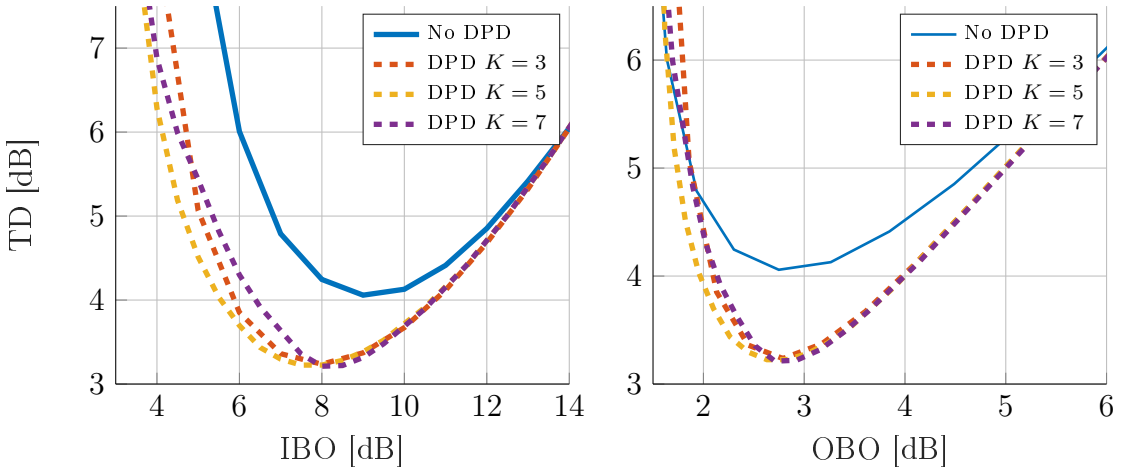

(a) Middle carrier: IBO Vs. TD.

(b) Middle carrier: OBO Vs. TD.

Figure 4-5: Effect of order (K) on DPD performance, DPD method: IDLA. $Q = 10$.

4.1.3.3 DPD learning architecture: direct Vs. in-direct

DPD gain also depends on the learning architecture used to train the DPD coefficients. Fig. 4-6 compares the performance of the proposed IDLA-based and DLA-based DPD methods in terms of TD. The respective DPD order and memory for both learning architectures are labeled on the figure itself. The selected memories exhibit the best performance for each algorithm for the given simulation parameters. Note that the HPA in the OBP is modeled with Q=0. This is because the HPA model used in the forward path is the Saleh model which is memoryless. It can be observed from Fig. 4-6 that the DLA-based DPD slightly outperforms the IDLA-based DPD when no additional bandlimitation is considered. Note that this marginal gain in performance comes at a cost of reduced speed and increased computational complexity. This is because the DLA-based DPD first estimates the HPA model, and then the estimated HPA model is used to obtain the DPD MP model coefficients. Note that the performance of both methods may vary when further bandlimitation would be introduced. This is studied in the next section.

4.2 Bandlimitation analysis

Last section presented the system parameter identification analysis to identify the key parameters effecting the DPD gain. This section covers an equally important

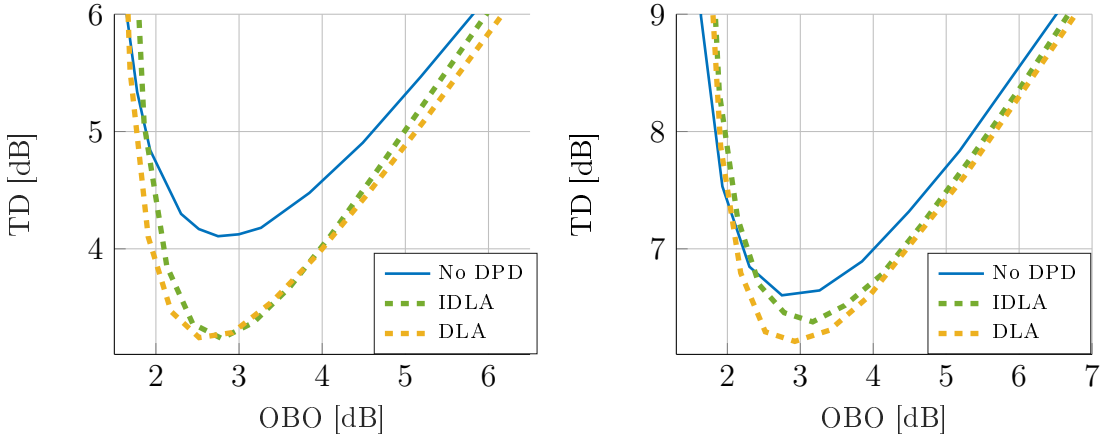

(a) [Middle carrier, DLA: $K = 3$ $Q = 5$, IDLA: $K = 3$ $Q = 10$, HPA: $K = 3$ $Q = 0$.

(b) Edge carrier, DLA: $K = 3$ $Q = 5$, IDLA: $K = 3$ $Q = 30$,HPA: $K = 3$ $Q = 0$.

Figure 4-6: The performance comparison of **(DLA)**-based and **(IDLA)**-based DPD.

aspect of this thesis, i.e., the effect of additional bandlimitation on the DPD performance. More importantly, this section investigates on how low the bandwidths of the feedback filter ($g(t)$) and forward DPD filter ($h(n)$) can be to still achieve a gain when the presented DPD methods are implemented. In addition, the section will also compare the performance of the IDLA-based and DLA-based DPD under the bandlimitation constraint. Unless stated otherwise, the fixed simulation parameters for the results presented in this section are listed in Table 4.1.

4.2.1 Bandlimitation: feedback path

Bandlimitation in the feedback path is introduced via the analog bandpass filter $g(t)$ (See Fig. 3-7). The bandlimitation helps reduce the burden on the sampling and processing rates of the ADCs and DSPs involved in DPD coefficients computation.

4.2.1.1 IDLA-based DPD performance

Middle Carrier: Fig. 4-7 presents the effect of bandlimitation on the performance of the IDLA-based DPD in terms of TD and BER for the middle carrier. It is observed that when the bandwidth of the analog bandpass filter $g(t)$ is reduced, the TD and BER performance suffers. This is because the vital HPA output information needed to estimate the optimal DPD coefficients gets cut due to the bandlimitation. Moreover, since the filter $g(t)$ is an analog bandpass filter, it also exhibits non-ideal

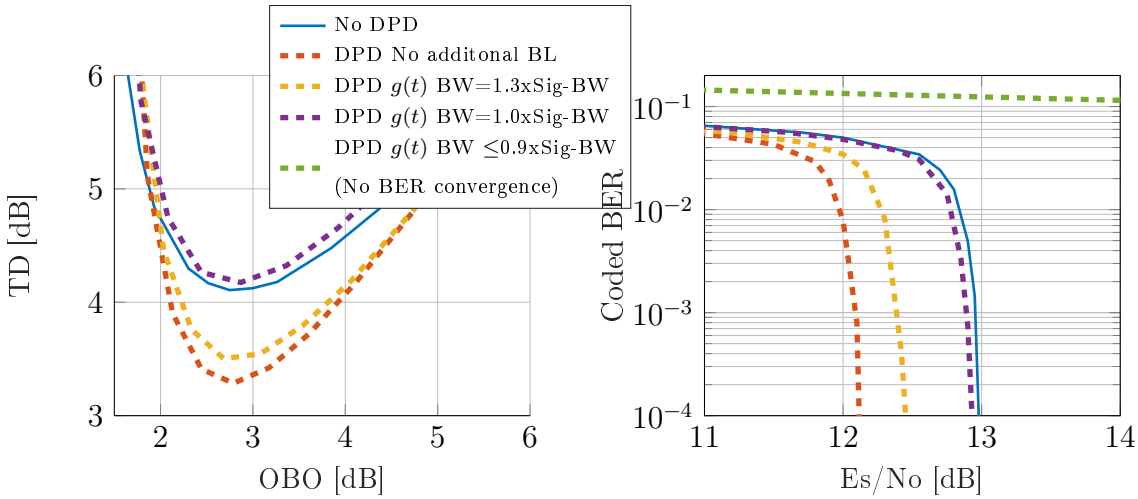

(a) Middle carrier: OBO Vs. TD.

(b) Middle carrier: BER performance.

Figure 4-7: Bandlimitation in the feedback path. Carrier: **middle**, DPD Method: IDLA, $K = 3$, $Q = 10$, DPD filter BW=1.5xSig-BW.

filter characteristics. As a result, $g(t)$ not only cuts the feedback signal but also adds linear and non-linear distortions to it. This also effects the DPD coefficient estimation process. Note that the best performance for the middle carrier is observed for the curve labeled "No additional BL" which inherently includes the bandlimitation from the OMUX. The other dotted curves represent the scenarios where the bandwidth of $g(t)$ is reduced below the "No additional BL" case. From Fig. 4-7, it is clear that while employing the bandlimited IDLA-based DPD, the feedback path bandwidth should not be reduced below the signal BW, as this leads to a performance worse than the "No DPD" case.

Edge Carrier: Fig. 4-8 presents the effect of bandlimitation on the BER performance of the IDLA-based DPD for the edge carrier. It is observed that performing additional bandlimitation leads to a much severe loss in BER performance for the edge carrier when compared to the middle carrier, where the feedback path bandwidth could be reduced to at most the signal bandwidth. The edge carrier suffers more under bandlimitation due to the fact that $g(t)$ adds more severe linear and non-linear to the edge carrier. Note that for all the presented figures, the DPD coefficients are computed for the entire bandwidth of the feedback signal. However, the DPD behavior can be different for each carrier even though a single set of DPD coefficients

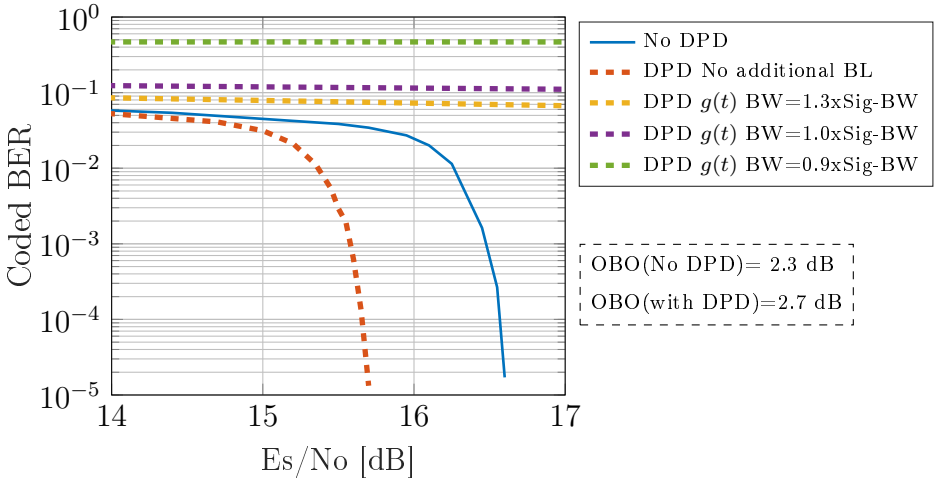

Figure 4-8: Bandlimitation in the feedback path. DPD Method: IDLA, carrier: **Edge**, $K = 3$, $Q = 30$, DPD filter BW=1.5xSig-BW.

are applied to the entire signal in the forward path. Fig. 4-7 and Fig. 4-8 are an example of such behavior under bandlimitation. Moreover, DPD gain can also vary among carriers for no additional bandlimitation cases. This is exhibited in 4-4b where the DPD gain for middle carrier is much larger than the edge carrier.

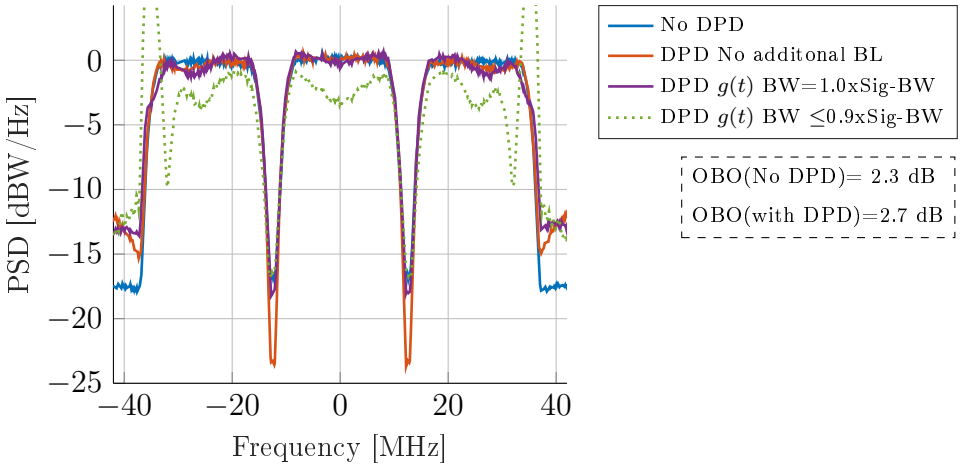

Figure 4-9: PSD analysis, bandlimitation in the feedback path. DPD Method: IDLA, $K = 3$, $Q = 10$, DPD filter BW=111 MHz.

Fig. 4-9 presents the PSD at the HPA output for the bandlimitation scenario presented in Fig. 4-7 and Fig. 4-8. The PSD results are consistent with the presented TD and BER results for the IDLA-based DPD. From Fig. 4-9, it is observed that when no additional bandlimitation is considered, the HPA output signal exhibits the least IMD noise, leading to the best performance. Moreover, when the feedback BW

is limited to the signal BW, the IMD noise and ACPRs rise. In addition, the HPA output is distorted for the edge carriers, hence no BER convergence (see Fig. 4-8). Furthermore, when the bandwidth of $g(t)$ is reduced below the signal BW (e.g. 0.9xSig-BW), the HPA output is completely distorted for all the carriers, making it impossible to recover the transmitted data. Therefore, when the IDLA-based DPD is implemented, no additional bandlimitation should be considered.

4.2.1.2 DLA-based DPD performance

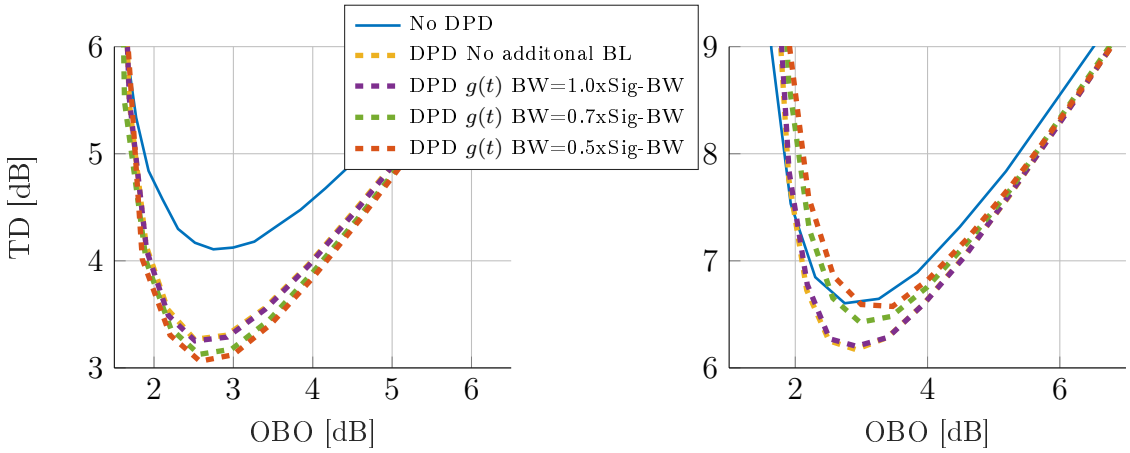

(a) Middle carrier.

(b) Edge carrier.

Figure 4-10: Bandlimitation in the feedback path. DPD Method: DLA, $K = 3$, $Q = 5$, HPA:$K = 3$, $Q = 0$.

Fig. 4-10 presents the TD performance for the DLA-based DPD under the additional bandlimitation constraint. It is clear from Fig. 4-10 that for the DLA-based DPD, the feedback path filter bandwidth can be reduced below the uplink signal BW without a severe loss in performance which was not the case for the IDLA-based DPD. However for this particular scenario, the feedback path bandwidth cannot be reduced below half of the uplink signal BW as the TD performance of the edge carrier worsens and becomes equal to the "No DPD" case. The TD performance is consistent with the PSD analysis provided in Fig. 4-11, where unlike the IDLA-based DPD case, the signal shape is preserved for feedback path filter bandwidths below the uplink signal BW. It is clear that the proposed DLA-based DPD out performs the IDLA-based DPD, as it can support much lower feedback path filter BW leading

to the employment of more practical and less power consuming ADCs. However, this comes at a cost of increased computational complexity and reduced speed. It should be noted that the transponder HPA in the forward path was modeled with the Saleh model. The Saleh model can be easily estimated with a third order polynomial with zero memory, even when the additional bandlimitation is introduced. As a result, the performance of the DLA-based DPD does not deteriorate when the feedback path bandwidth is reduced below the signal bandwidth as in the case of the IDLA-based DPD. For more complex HPA models in the transponder's forward path, the behavior of the DLA-based DPD may be different under severe bandlimitation, and is not covered in this work.

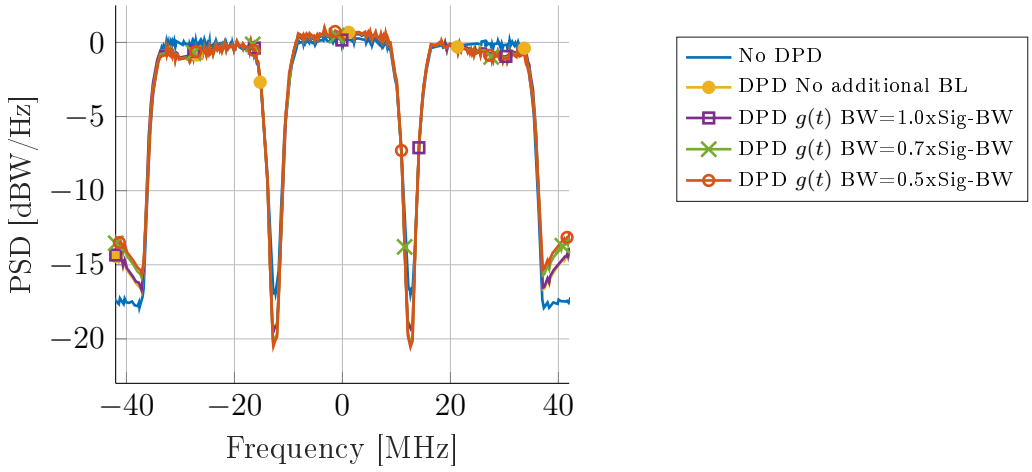

Figure 4-11: PSD analysis, bandlimitation in the feedback path. DPD Method: DLA, $K = 3$, $Q = 5$, HPA:$K = 3$, $Q = 0$.

4.2.2 Bandlimitation: forward path

Bandlimitation in the forward path is introduced by a digital bandpass filter $h(n)$ which allows the use of low speed DACs in the forward path of DPD architecture. The filter $h(n)$ determines the band in which DPD occurs. As a result, the bandwidth of $h(n)$ cannot be reduced below the signal BW, as this would cut the signal itself in the forward path before the amplification. Fig. 4-12 presents the affect of reducing the bandwidth of $h(n)$ on the performance of the two proposed DPD methods in terms of TD. Note that for the simulated scenario, in the case of the middle carrier, the TD performance of the both DPD methods remains more or less the same when the

bandwidth of $h(n)$ is reduced from 1.5 to 1.3 times the uplink signal BW (See Fig. 4-12a). However, the same reduction in bandwidth severely effects the edge carrier TD performance, as depicted in Fig. 4-12b. This is because $h(n)$ is a non-ideal bandpass filter, and tighter $h(n)$ adds more severe linear and non-linear distortions to the input, especially to the edge carriers. Nonetheless, for the given scenario a bandwidth of 1.5xSignal-BW is needed for implementing the proposed DPD methods. It is clear from the presented bandlimitation analysis that the bandwidth of the feedback path filter $g(t)$ and forward path DPD filter $h(n)$ plays a key role in determining the DPD performance. As a result, the two parameters should be kept in mind when designing and implementing bandlimited DPD.

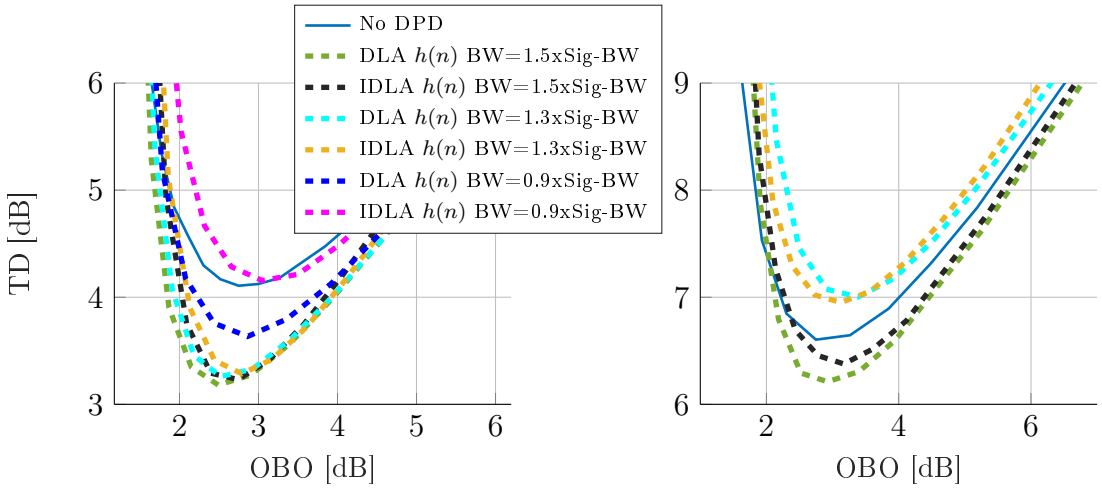

(a) Mid carrier,DLA:$K = 3$ $Q = 5$, IDLA:$K = 3$ $Q = 10$(b) Edge carrier, DLA: $K = 3$ $Q = 5$, IDLA: $K = 3$ $Q = 30$.

Figure 4-12: Bandlimitation in the forward path, no additional bandlimitation in feedback path.

4.3 Power and hardware implementation analysis

Section 4.1 and Section 4.2 presented the main findings of this work, i.e., the system parameter identification and bandlimitation analysis. This section covers another important aspect of DPD, i.e., the practical implementation. To this end, this section discusses different aspects of DPD such as power consumption, carrier fairness, computational complexity and hardware requirements. The presented discussion helps provide a better understanding of the practical aspects related to on-board DPD implementation.

4.3.1 Power consumption

Estimating the power consumption of the ADCs, DACs, and FPGAs involved in DPD implementation is not a trivial task. These estimates depend on on factors like sampling rates, bit-resolutions, word-lengths, bandwidths of the signals involved, etc. Nonetheless, a table has already been provided for the power consumed by some of the space grade ADCs in Section 2.3.2 Table 2.2. In addition, the following presents an estimate for the power consumed by the fullband MP-based DPD in the forward path. The power consumed is dependent on the complexity which in turn depends on the algorithm's mathematical expression. The computational complexity of a fullband MP-based DPD is given in [123, Table 1]. It is to be noted that in these calculations, the effects of the word-lengths as well as data storage and communication are not included as they are highly dependent on the chosen hardware and architecture. The power consumed per sample is given in [123, Equation (4)]. For the reader's ease, it is also provided below.

$$P_{\text{DPD}} = E_{\text{cycle}}(\frac{7}{2} \cdot K \cdot Q + \frac{9}{2}), \tag{4.2}$$

where E_{cycle} is the energy consumption per cycle of a fixed-point DSP. For $K = 3$, $Q = 10$, $N = 64800$, and $E_{\text{cycle}} = 150\frac{\text{pWs}}{\text{cycle}}$, the power consumed by DPD in forward path is 1.1 mW. Note that Eq. 4.2 is valid for a fullband MP model. The bandlimited model includes a few additional operations which will result in slightly higher power consumption. Computational complexity for the proposed DPD methods is derived in Section 4.3.3. Furthermore, Eq. 4.2 only presents the running power of the DPD, i.e., forward path implementation. Power would also be consumed in the feedback path which depends on the identification complexity. Identification of the DPD coefficients requires an inverse. It is difficult to obtain an equation for the power consumed in the identification process, as it is dependent on how the inverse is computed. This task has been left as a future work.

4.3.2 DPD and carrier fairness aspects

In certain scenarios DPD can be unfair. Here unfairness implies that DPD may prefer some carriers over the others, even though the same DPD coefficients are

applied to all the carriers. Fig. 4-13 demonstrates the carrier fairness aspect of DPD, when applied to a 10-carrier signal. The simulated carriers have unequal power and bandwidths. Fig. 4-13 presents the normalized PSD of the received signal. Note that a higher peak of the PSD, and a lower IMD noise implies a larger received carrier to noise ratio (CNR). A higher CNR would lead to a reduced BER. From Fig. 4-13, it is clear that the gain in CNR is different for each carrier when DPD is applied. Especially the powerful carriers are favored, while the carriers nearby the powerful carriers or at the edges are disadvantaged, and they may exhibit a smaller or a reduced CNR gain. Moreover, the PSD performance changes when a different memory depth is considered (See Fig. 4-13a and Fig. 4-13b). Therefore, in scenarios with different carrier powers and bandwidths, the carrier fairness aspect should be kept in mind when developing and implementing DPD algorithms.

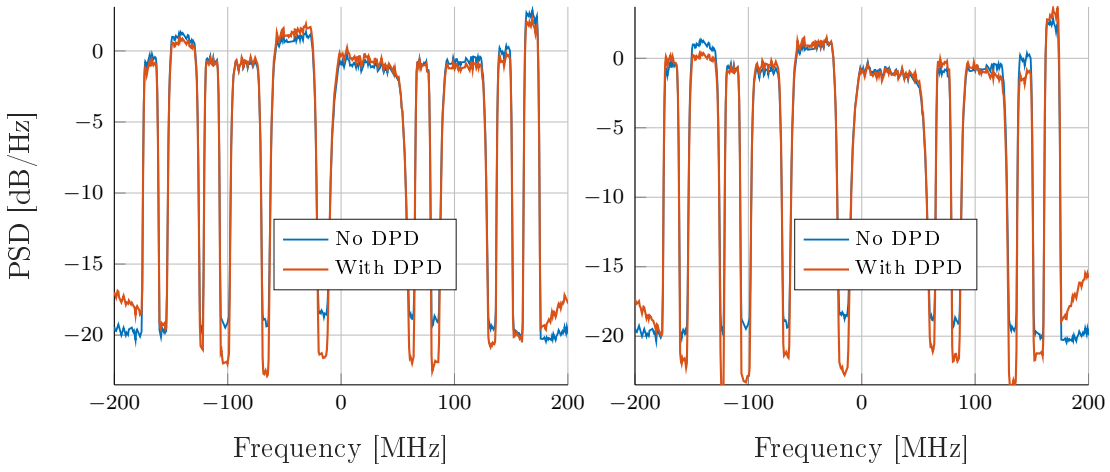

(a) Memory ($Q = 5$). (b) Memory ($Q = 10$).

Figure 4-13: Carrier fairness aspects of DPD, DPD Method: IDLA, $K = 3$, no additional bandlimitation.

4.3.3 Hardware implementation requirements of on-board DPD

As discussed in Chapter 2 Section 2.3, the on-board FPGAs have reduced signal processing capabilities when compared to their terrestrial counterparts. Therefore, it is vital to analyze the possibility and feasibility of implementing the proposed DPD algorithms in the on-board FPGAs. Table 2.1 in Chapter 2 presented a few key features of a state-of-the-art on-board FPGA. The signal processing capabilities of a

FPGA depend on the available number of DSP slices, registers, LUTs, memory and more importantly on the operational bandwidths and sampling rates. The state-of-the-art Virtex-5QV space grade FPGA is equipped with 320 hardwired DSP slices (or multiplier block) which translates to 320 parallel multiplications and additions. The FPGA contains 87,920 LUTs, and 131,072 configurable logic blocks (CLBs) slices which can operate as 32 bit shift registers (or 16-bit x 2 shift registers) or as 64 bit distributed random access memory (RAM). The 10.5 mega bits (MBs) of integrated memory can offer a performance of up to 360 MHz.

4.3.3.1 Computational complexity of the proposed DPD methods

The presented IDLA and DLA-based DPD algorithms perform a memory polynomial based predistorter implementation. A typical way to evaluate the computational complexity of an algorithm is to calculate the number of multiplications and summations needed. Implementing the MP-based DPD essentially involves the addition and multiplication of complex numbers, and more importantly a square ($|x(n)|^2$) or a quartic ($|x(n)|^4$) operation depending on the order (K) of the DPD. This is depicted in Eq. 3.15a. The addition and multiplication of the complex numbers can be implemented within 1 clock cycle in FPGAs. However, the quartic operation of complex numbers is a computationally exhaustive task in FPGAs and may require more than 1 clock cycle. The calculation times can be reduced if pipelining and Vedic mathematics [124] is considered. A novel square and cube operator implementation architecture, based on Vedic mathematics is proposed in [125]. The proposed approach in [125] can achieve a square operation within 18 nano seconds (ns) while using only 63 LUTs for 32-bit operands. Implementing a 5^{th} order predistorter would require a quartic operation which would lead to considerable delays, and should be avoided especially in on-board FPGAs. However, for the given simulation setup, it has been shown that a 3^{rd} order non-linearity compensation is more than sufficient. For block-based signal processing, matrix operations are considered. Eq. 3.16a is implemented to perform DPD on a block of N samples. This gives rise to a matrix operation of the form $\mathbf{z}_f = \hat{\mathbf{X}}_f \mathbf{c}$ where the entries of the matrix $\hat{\mathbf{X}}_f$ are given in Eq.

3.15a. Note that the entries in Eq. 3.15a and Eq. 3.16a are complex. A complex multiplication requires 4 real multiplications and 2 real summations, whereas a complex summation consists of 2 real summations. Table 4.2 provides the number of additions and multiplications needed for implementing the proposed predistorters given by Eq. 3.15a and Eq. 3.16a. The total number of additions and multiplications is the sum of additions and multiplications needed to implement Eq. 3.15a and Eq. 3.16a. It is clear from Table 4.2 that more multiplications are needed than the summations. For a parameter set ($K = 3$, $Q = 5$, $L = 10$, and $N = 10$) 5520 multiplications and 2784 summations are needed.

Table 4.2: Multiplications and summations for DPD implementation.

Equation	Multiplications		Summations	
3.15a $\hat{\mathbf{X}}_f$	$N(Q+1)4L$	$k=1$	$N(Q+1)2L$	$k=1$
	$N(Q+1)(\frac{K-1}{2})\cdot(4L+\sum_{k=3}^{K}\frac{k+5}{2})$	$k\geq 3$	$N(Q+1)(\frac{K-1}{2})\cdot(1+2L)$	$k\geq 3$
3.16a $\hat{\mathbf{X}}_f\mathbf{c}_{BL}$	$4N(Q+1)\frac{K+1}{2}$		$3(N-1)(Q+1)\frac{K+1}{2}$	

K: Max Non-linear order, Q=Max memory depth, N: sample block size, L: DPD filter length

In order to implement the proposed direct or in-direct learning architecture-based predistorters (Eq. 3.16a), the DPD coefficients must be computed first. DPD coefficients are computed through a LS-based approach as depicted in Eq. 3.17a $\mathbf{c}_{BL} = (\hat{\mathbf{Y}}_f^H\hat{\mathbf{Y}}_f)^{-1}\hat{\mathbf{Y}}_f^H\mathbf{z}_f$. Eq. 3.17a requires two matrix multiplications, a matrix and vector multiplication and one matrix inversion. The matrix $\hat{\mathbf{Y}}_f$ is defined in the same way as $\hat{\mathbf{X}}_f$ or $\hat{\mathbf{Z}}_f$. Therefore, computing $\hat{\mathbf{Y}}_f$ exhibits similar computational complexity as Eq. 3.15a. Table 4.3 presents the number of summations and multiplications needed to compute the matrix $\hat{\mathbf{Y}}_f$, and the DPD coefficients given by Eq. 3.17a. Matrix inversion is a computationally exhaustive operation. As a result, the number of summations and multiplications needed to implement Eq. 3.17a are much higher compared to Eq. 3.16a. To compute the DPD coefficients for ($K = 3$, $Q = 5$,

$L = 10$, and $N = 10$), 18072 multiplications and 11764 summations are needed. It is clear that the matrix inversion operation in the proposed IDLA and DLA-based DPD approach is the most time consuming and computationally expensive operation. Thus, the inversion could become a bottle neck in on-board DPD implementation where the computational power is limited and the delays are of concern.

Table 4.3: Multiplications and summations for DPD coefficients estimation.

Equation	Multiplications		Summations	
3.15c $(\hat{\mathbf{Y}}_f)$	$N(Q+1)4L_g$	$k=1$	$N(Q+1)2L_g$	$k=1$
	$N(Q+1)(\frac{K-1}{2})\cdot$ $(4L_g + \sum_{k=3}^{K} \frac{k+5}{2})$	$k \geq 3$	$N(Q+1)(\frac{K-1}{2})\cdot$ $(1+2L_g)$	$k \geq 3$
3.17a $(\hat{\mathbf{Y}}_f^H \hat{\mathbf{Y}}_f)^{-1} \hat{\mathbf{Y}}_f^H \mathbf{z}_f$	$\frac{(K+1)^2(Q+1)^2}{2}[3N+$ $\frac{(K+1)(Q+1)}{2}+3]+$ $3(K+1)(Q+1)$		$\frac{(K+1)(Q+1)}{2}\left[\frac{(K+1)(Q+1)}{2}+1\right]+$ $\frac{(K+1)^2(Q+1)^2}{2}\left[\frac{(K+1)(Q+1)}{2}-1\right]+$ $2N\left[(K+1)(Q+1)-1\right]\cdot$ $\left[\frac{(K+1)(Q+1)}{2}+1\right]$	

K: Max Non-linear order, Q=Max memory depth, N: sample block size, L_g: feedback filter length

4.3.3.2 Proposed DPD methods and space-grade FPGAs

A detailed study on a FPGA-based matrix inversion was presented in [126] where a Xilinx Virtex-5 XC5VLX220T was utilized to implement a novel matrix inversion architecture. The utilized FPGA has similar computational capabilities to that of a state-of-the-art space grade Xilinx Virtex-5QV FPGA. The proposed inversion design in [126] performed a 4×4 matrix inversion with a latency of 12 clock cycles. Meanwhile, the hardware design required only 1474 slice registers, 1458 LUTs, and 52 DSP slices. The method in [126] could also be scaled for a 6×6, 8×8 or 10×10 matrix inversion. Table 4.4 presents the hardware requirements of the matrix inversion architecture in [126] for different sized matrices. It can be seen that a 10×10 matrix inverse requires 36% of the DSP slices, and 40% of the LUTs resources. A 10×10 matrix corresponds to a $K = 3$ and $Q = 4$. As the dimensions of the matrix to be inverted grow, more of the OBP resources would be dedicated to perform the matrix

inversion. It should be noted that the OBP may be needed to perform other tasks e.g., beam forming, switching etc., in parallel with DPD implementation. As a result, the complete resources of the OBP cannot be reserved for DPD alone. This limits the size of the matrices to be multiplied or inverted, which in turn limits the order and memory of the predistorter. As shown in the Section 4-6, the DLA-based DPD provides a sound gain in TD performance for $K = 3$ and $Q = 5$ for the simulated scenario. From a computational perspective, the DLA-based DPD requires a 12×12 matrix inversion, which can possibly be implemented on the FPGA while leaving sufficient resources for the other tasks and operations. From the above discuss, it is clear that the on-board DPD should only be implemented for scenarios which allow practical hardware implementation and minimal processing delays such as lower memory depths and orders.

Table 4.4: Hardware requirements of the matrix inversion architecture for different size matrices.

Size matrix	4x4	6x6	8x8	10x10	Available
Slice Reg.	1474	2901	4788	7135	131072
Slice LUTs	1458	3009	24904	55060	131072
DSP Slices	52	102	112	114	320

Another aspect of implementing signal processing algorithms on FPGAs is memory availability for storing variables. However, the state-of-the-art space grade Xilinx Virtex-5QV FPGA is equipped with 10.5 MBs of RAM which is more than enough to implement the proposed DPD algorithms in terms of the memory requirements. Sampling rates of the embedded ADCs, DACs, and FPGAs also play a vital role in the implementation of signal processing algorithms, especially DPD where the sampling rates and signal bandwidths effect the performance. The state-of-the-art Xilinx Virtex-5QV FPGA can operate on signals with bandwidths ranging between 36 MHz and 450 MHz. The Xilinx Virtex-5QV FPGA has been embedded in the latest Fraunhofer OBP (FOBP) which is to be employed in the Heinrich Hertz research satellite mission coordinated by the German aerospace center (DLR). The satellite is planned for a launch in 2022. The FOBP also contains space grade ADCs and DACs

which can also sample signals with bandwidths ranging between 36 MHz and 450 MHz. This implies that an OBP like the FOBP can implement on-board bandlimited DPD for wideband signals with bandwidth up to 300-400 MHz. For signals with bandwidth ranging between 100-200 MHz, the FOBP can perform on-board DPD with much more relaxed bandlimitation constraints. Although FOBP is equipped with fast DACs and ADCs, but it exhibits the signal processing constraints associated with the space grade on-board FPGAs. Therefore, the computational load of the on-board signal processing algorithms such as DPD or beamforming should be kept in mind when designing the digital satellite payloads.

4.3.3.3 Proposed DPD methods and quantization effects

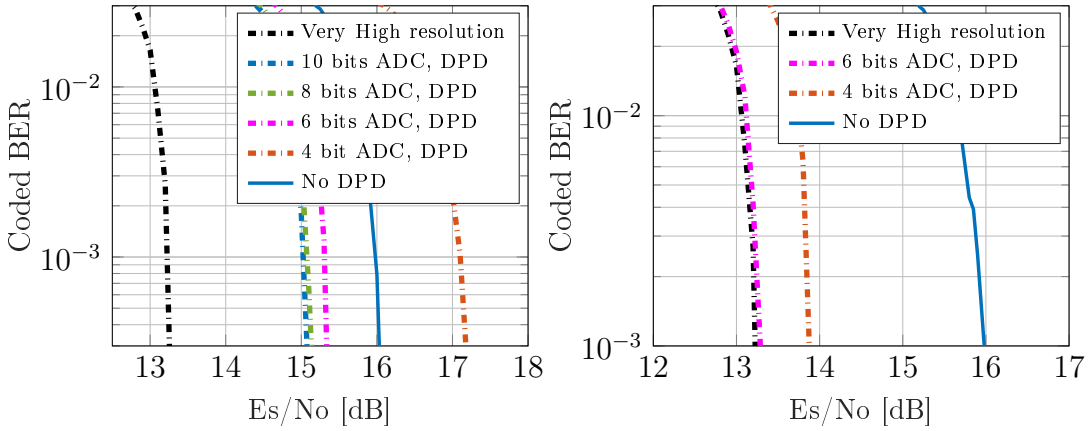

(a) Middle carrier, Max-Level=1

(b) Edge carrier, Max-Level=1.25

Figure 4-14: Quantization effects for the ADCs. DPD method: IDLA, K=3, Q=10, IBO=6 dB, Modulation: 16-APSK, Code rate: 5/6.

As mentioned earlier, the quantization effects of the ADCs/DACs and FPA designs of the digital component were not considered in the presented results. However, the quantization noise does play a critical role in the DPD performance. This section briefly discusses the effects of bit resolution and dynamic-range of converters (Max-Level) on the DPD performance. Figure 4-14 presents the quantization effects of ADCs. The transponder architecture in Fig. 3-7 is simulated where the bit resolution and the maximum quantization level of the ADCs is varied. It is clear from Figure 4-14 that the resolution of the ADC and the maximum level of quantization influences

the DPD performance. A lower bit resolution introduces more quantization noise, leading to inaccurate estimation of DPD coefficients. Moreover, a higher dynamic range (Max-level) ensures that the high peaks of the HPA output are also sampled accurately without any clipping. An important future task would be to identify the lowest possible bit resolution and the Max-Level which leads to a minimum loss in performance while keeping the overall power consumption low.

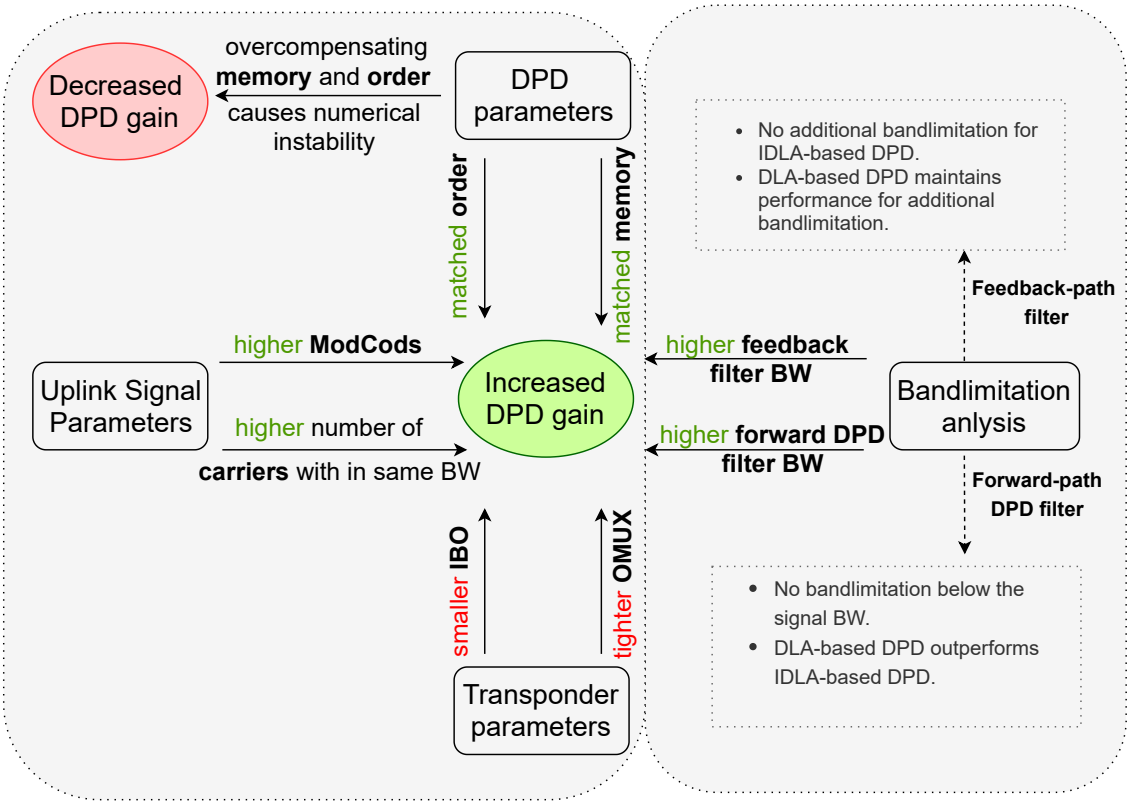

Figure 4-15: Summary: system parameter identification and bandlimitation analysis.

4.4 Summary

This chapter presented the numerical results for the proposed DPD methods. A through analysis of system parameter identification and bandlimitation effects was presented. A summary of the presented analysis is provided in Fig. 4-15. The system parameter identification analysis gave an insight into the scenarios where implementing DPD is practical and leads to larger gains. In addition, a performance comparison between the state-of-the-art IDLA-based DPD and a novel iterative DLA-based DPD

under bandlimitation constraints was also presented. Lastly, the chapter also presented a computational complexity analysis for the considered DPD approaches. It was shown that to keep the hardware requirements low, smaller order and memory-based MP predistorter should be considered for on-board DPD implementation. The next chapter concludes this thesis, and provides the possible future extensions of this work.

Chapter 5

Conclusion

This work focused on the on-board digital linearization of satellites. Chapter 1 introduced the problem statement, i.e., the on-board compensation of the linear and non-linear distortions caused by the transponder's non-linear HPAs and filters. In addition, the motivation behind the implementation of the on-board bandlimited DPD was provided as well. Lastly, Chapter 1 also summarized the main contributions of this research work. Chapter 2 detailed a transparent HTS transponder equipped with on-board processing capabilities. Different blocks of the transponder were discussed in the context of the aforementioned linear and non-linear distortions. In addition, the conventional HPA models such as the Volterra and memory polynomial were also presented to analyze the non-linear HPA effects. These models later served as a basis for predistortion. Chapter 3 introduced predistortion as a concept. The chapter also provided an overview of different predistortion methods existing in the literature, and proposed the class and type of predistortion best suited to HTS. The mathematical framework for the proposed bandlimited MP DLA-based and IDLA-based DPD methods was also detailed in the chapter. Moreover, the chapter also covered the application of the novel iterative DLA-based DPD to MPAs and 5G waveforms. Chapter 4 presented the numerical analysis for the proposed DPD methods. A summary of the main findings of this thesis is provided in the next section. Chapter 5 concludes this work and presents an insight into future works.

5.1 Summary: Main findings

The primary focus of this thesis was to identify the most critical parameters which effect the performance of DPD. In addition, a detailed analysis of bandlimitation in the feedback and forward path was also presented to answer the question of how low the sampling bandwidths can be to still achieve a DPD gain. Lastly, two applications of predistortion incorporating the novel DLA-based DPD were also discussed. The main findings are summarized in the following.

5.1.1 System parameters identification analysis

Three sets of system parameters were investigated to study the trends in DPD gain. The first set included the uplink signal parameters, i.e., the ModCods and number of carriers. It was found out that DPD leads to a larger gain in BER performance when a higher number of carriers are packed within the signal BW, and when higher ModCods are applied. Moreover, DPD leads to a rise in OBO especially when multicarrier operation and higher ModCods are employed. A higher OBO implies a reduced power efficiency. Therefore, a trade-off exists between the number of packed carriers, ModCods and OBO.

The second set of parameters studied in the system parameter identification analysis were the transponder parameters, i.e., the IBO and OMUX guardband. It was found out that that a smaller IBO and a tighter guardband of the OMUX leads to a higher DPD gain. Note that a tighter guardband also leads to more efficient bandwidth transponders, but it also adds more severe linear distortions, especially to the edge carrier. As a result, a higher memory depth of the predistorter is needed to achieve a comparable performance to a more relaxed guardband scenario. Hence, there exists a trade-off between the BER performance and bandwidth efficiency too. The total degradation (TD) helps to optimize the BER performance and power efficiency. Therefore, TD analysis should be performed to optimize the two aforementioned trade-offs.

The third set of parameters studied in this thesis were the predistortion algorithm specific parameters. For the proposed MP-based DPD methods, this involved only

two parameters, i.e., memory (Q) and order (K). The best DPD performance was observed when the memory and order of the predistorter match the order and the memory of the non-linearities in the system. Moreover, increasing the memory and order beyond a certain point can lead to a loss in performance due to the associated numerical instability issues. Furthermore, it was observed that DPD may prefer some carriers over the others, especially for uplink signals with different carrier powers and bandwidths. Lastly, the presented results highlighted the fact that the memory plays a more crucial role in determining the DPD performance. Therefore, its optimal setting should be kept in mind, especially with regard to the carrier fairness and complexity aspects, when developing and implementing DPD algorithms.

5.1.2 Bandlimitation analysis

This work only focused on bandlimited DPD methods for HTS. The presented bandlimitation analysis gave an insight into how the sampling bandwidths of DACs and ADCs affect the DPD performance. The forward path DPD filter $h(t)$ determines the band in which predistortion occurs. Therefore, the bandwidth of $h(t)$ cannot be reduced below the signal bandwidth, irrespective of the DPD algorithm employed. The effects of bandlimitation in the feedback path are of more interest. It was observed that when implementing the state-of-the-art IDLA-based bandlimited DPD [17], the bandwidth of the feedback path filter $g(t)$ cannot be reduced below the signal bandwidth, i.e., no additional bandlimitation should be considered. This work also presented a novel iterative DLA-based DPD. The novel technique outperformed the state-of-the-art IDLA-based DPD. More importantly, it provided a more robust performance when the feedback path bandwidth was reduced below the signal bandwidth. For the presented scenario, the feedback path bandwidth could be reduced to half of the signal bandwidth. This leads to the employment of much slower ADCs in the feedback path which will ultimately reduce the power consumption.

5.1.3 Parameter adjustment and design

For a better understanding of the application of DPD in satellite payloads, it is equally important to understand where the identified parameters can be set or changed. The key performance parameters can be either adjusted during the normal

operation of the satellite, or they have to be set optimally during the payload design phase. To cope with the data traffic demand, the uplink signal parameters such as the ModCods and number of carriers are often changed during the run-time of the satellite. The adaptive DPD can track the changes in the uplink signal characteristics, and perform predistortion optimally. In addition, the parameters like the bandwidth of the forward path bandlimiting filter $h(n)$, memory (Q) and order (K) of the DPD, HPA's operating point (IBO), and sampling rates of ADCs/DACs can be adjusted during the normal satellite operation. A quick offline analysis can be performed for these parameters, for example during the service or downtime of the satellite. Once an optimal performance is achieved, the parameters can be adjusted on-board the satellite using the control commands from the ground station. On the other hand, parameters like the bandwidth of OMUX and feedback path filter $g(t)$ have to be set during the design phase, i.e., pre-launch. Furthermore, the bit-resolution of the converters is also set during the design phase. However, the upcoming digital payload designs also offer reconfigurable ADCs, DACs, and FPGAs [127].

5.1.4 DPD for MPAs and 5G waveforms

Apart from the system parameter identification and bandlimitation analysis, this work also presented two applications of the proposed DLA-based DPD in HTS. The first application involved the MPAs. A novel two-step compensation method for the hardware imperfections existing in MPAs was presented, and its performance was analyzed. MPAs are a key technology for future HTS, especially in terms of achieving power flexibility. Linearization of MPAs has recently gained a lot of attention. Moreover, the proposed novel two-step compensation approach serves as a stepping stone for further research in improving the MPA performance.

Another application of DPD presented in this work was in the context of 5G and HTS. 5G waveforms exhibit high PAPR which can saturate the on-board HPAs, leading to severe non-linear distortions in the downlink signal. As a result, linearization of on-board HPAs is of utmost importance when employing 5G waveforms in HTS. This work proposed the DLA-based DPD for predistortion of 5G waveforms in conjunction with PAPR reduction through signal clipping. It was observed that the proposed

DPD not only linearizes the HPAs but also removes the distortions introduced by signal clipping. The presented applications stress on the fact that the on-board DPD has future applications in HTS. As a result, the thorough system parameter identification and bandlimitation analysis conducted in this thesis is of vital importance for designing future DPD algorithms.

5.2 Concluding remarks and future perspectives

This work focused on the digital linearization of HPAs. The non-linear operation of HPAs limits the performance of HTS. The analog solutions employed in channel amplifiers of on-board HPAs are non-adaptive and offer limited gain. At the same time, the digital solutions applied on-ground are either not applicable in many HTS scenarios or drastically increase the complexity of the receiver terminal. However, with the advent of OBPs, we can mitigate the distortions introduced by the transponder filters and HPAs using on-board DPD. The presented numerical analysis also revealed that adaptive linearization is vital for future HTS. In addition, this work also provided a general insight into the on-board signal processing capabilities of HTS, especially in terms of the available processing power and the sampling rates. Even though the signal processing capabilities have significantly improved lately, they are still limited on-board the satellite. Therefore, it is vital to process the most relevant data and only involve the operations which lead to the desired result. The presented system parameter identification and bandlimitation analysis provided an insight into which parameters and trade-offs are the most beneficial in terms of predistortion, provided sufficient resources are available to implement a complete on-board predistortion solution.

From a future work perspective, the presented low-effort DPD algorithms and the system parameter identification analysis serve as a basis for further research in on-board DPD and its related applications. The optimization of the identified parameters is the key to maximize the benefits of DPD. As a result, further research should be conducted to develop algorithms to optimize the identified parameters. In addition, a more thorough analysis of the presented DPD algorithms needs to be performed

under more complex HPA models and true HPAs in hardware, while keeping the key performance parameters in mind. A true HPA may require a more complex DPD model e.g., GMP model. Furthermore, in order to completely asses the gains of DPD, quantization effects and the fixed-point-arithmetic (FPA) design of the digital components should be considered when transferring the DPD algorithms to FPGAs. Lastly, a cost analysis for the additional hardware needed to implement on-board DPD should be performed, and the costs must be compared to the terrestrial solutions. Such an analysis can provide a better insight into the gain of on-board DPD to a satellite manufacturer or the operator.

Appendix A

Expanded matrices for MP DPD and HPA model

The following provides the expanded form of the matrix $\hat{\mathbf{X}}_f$ and $\hat{\mathbf{Z}}_f$ defined in Eq. 3.16.

$$\hat{\mathbf{X}}_f = \begin{bmatrix} \hat{x}_{BL}(0,1,0) & \hat{x}_{BL}(1,1,0) & \cdots & \hat{x}_{BL}(N-1,1,0) \\ \hat{x}_{BL}(0,1,1) & \hat{x}_{BL}(1,1,1) & \cdots & \hat{x}_{BL}(N-1,1,1) \\ \vdots & \vdots & \cdots & \\ \hat{x}_{BL}(0,1,Q) & \hat{x}_{BL}(1,1,Q) & \cdots & \hat{x}_{BL}(N-1,1,Q) \\ \vdots & \vdots & \cdots & \vdots \\ \hat{x}_{BL}(0,K,Q) & \hat{x}_{BL}(1,K,Q) & \cdots & \hat{x}_{BL}(N-1,K,Q) \end{bmatrix}, \tag{A.1a}$$

$$\hat{\mathbf{Z}}_f = \begin{bmatrix} \hat{z}_{BL}(0,1,0) & \hat{z}_{BL}(1,1,0) & \cdots & \hat{z}_{BL}(N-1,1,0) \\ \hat{z}_{BL}(0,1,1) & \hat{z}_{BL}(1,1,1) & \cdots & \hat{x}_{BL}(N-1,1,1) \\ \vdots & \vdots & \cdots & \\ \hat{z}_{BL}(0,1,Q) & \hat{z}_{BL}(1,1,Q) & \cdots & \hat{z}_{BL}(N-1,1,Q) \\ \vdots & \vdots & \cdots & \vdots \\ \hat{z}_{BL}(0,K,Q) & \hat{z}_{BL}(1,K,Q) & \cdots & \hat{z}_{BL}(N-1,K,Q) \end{bmatrix}, \tag{A.1b}$$

where the entries of the matrix in Eq. A.1 are defined in Eq. 3.15. Using Eq. 3.15 in the above equations, we get

$$\hat{\mathbf{X}}_f = \begin{bmatrix} \sum_{i=1}^{L} x(0)h(i) & \sum_{i=1}^{L} x(1)h(i) & \cdots & \sum_{i=1}^{L} x(N-1)h(i) \\ \sum_{i=1}^{L} x(-1)h(i) & \sum_{i=1}^{L} x(0)h(i) & \cdots & \sum_{i=1}^{L} x(N-2)h(i) \\ \vdots & \vdots & \cdots & \\ \sum_{i=1}^{L} x(-Q)h(i) & \sum_{i=1}^{L} x(1-Q)h(i) & \cdots & \sum_{i=1}^{L} x(N-1-Q)h(i) \\ \vdots & \vdots & \cdots & \vdots \\ \sum_{i=1}^{L} x(-Q)\left|x(-Q)\right|^2 h(i) & \sum_{i=1}^{L} x(1-Q)\left|x(1-Q)\right|^2 h(i) & \cdots & \sum_{i=1}^{L} x(N-1-Q)\left|x(N-1-Q)\right|^2 h(i) \\ \vdots & \vdots & \cdots & \vdots \\ \sum_{i=1}^{L} x(-Q)\left|x(-Q)\right|^{K-1} h(i) & \sum_{i=1}^{L} x(1-Q)\left|x(1-Q)\right|^{K-1} h(i) & \cdots & \sum_{i=1}^{L} x(N-1-Q)\left|x(N-1-Q)\right|^{K-1} h(i) \end{bmatrix}, \tag{A.2}$$

$$\hat{\mathbf{Z}}_f = \begin{bmatrix} \sum_{i=1}^{L_g} z_f(0)g(i) & \sum_{i=1}^{L_g} z_f(1)g(i) & \cdots & \sum_{i=1}^{L_g} z_f(N-1)g(i) \\ \sum_{i=1}^{L_g} z_f(-1)g(i) & \sum_{i=1}^{L_g} z_f(0)g(i) & \cdots & \sum_{i=1}^{L_g} z_f(N-2)g(i) \\ \vdots & \vdots & \cdots & \\ \sum_{i=1}^{L_g} z_f(-Q)g(i) & \sum_{i=1}^{L_g} z_f(1-Q)g(i) & \cdots & \sum_{i=1}^{L_g} z_f(N-1-Q)g(i) \\ \vdots & \vdots & \cdots & \vdots \\ \sum_{i=1}^{L_g} z_f(-Q)\left|z_f(-Q)\right|^2 g(i) & \sum_{i=1}^{L_g} z_f(1-Q)\left|z_f(1-Q)\right|^2 g(i) & \cdots & \sum_{i=1}^{L_g} z_f(N-1-Q)\left|z_f(N-1-Q)\right|^2 g(i) \\ \vdots & \vdots & \cdots & \vdots \\ \sum_{i=1}^{L_g} z_f(-Q)\left|z_f(-Q)\right|^{K-1} g(i) & \sum_{i=1}^{L_g} z_f(1-Q)\left|z_f(1-Q)\right|^{K-1} g(i) & \cdots & \sum_{i=1}^{L_g} z_f(N-1-Q)\left|z_f(N-1-Q)\right|^{K-1} g(i) \end{bmatrix}, \tag{A.3}$$

where $x(n)$ is the input to the DPD block, and $z_f(n) \forall\, n = 0 \cdots N-1$ is defined in Eq. 3.14a. The following provides the expanded form of the matrix $\hat{\mathbf{Y}}_f$ and $\tilde{\mathbf{Y}}_f$. In Table 3.3, $\tilde{\mathbf{Y}}$ represents the estimated HPA output and $\hat{\mathbf{Y}}$ represents the measured HPA output in the feedback path.

$$\hat{\mathbf{Y}}_f = \begin{bmatrix} y_f(0,1,0) & y_f(1,1,0) & \cdots & y_f(N-1,1,0) \\ y_f(0,1,1) & y_f(1,1,1) & \cdots & y_f(N-1,1,1) \\ \vdots & \vdots & \cdots & \\ y_f(0,1,Q) & y_f(1,1,Q) & \cdots & y_f(N-1,1,Q) \\ \vdots & \vdots & \cdots & \vdots \\ y_f(0,K,Q) & y_f(1,K,Q) & \cdots & y_f(N-1,K,Q) \end{bmatrix}, \tag{A.4a}$$

$$\tilde{\mathbf{Y}}_f = \begin{bmatrix} \tilde{y}_f(0,1,0) & \tilde{y}_f(1,1,0) & \cdots & \tilde{y}_f(N-1,1,0) \\ \tilde{y}_f(0,1,1) & \tilde{y}_f(1,1,1) & \cdots & \tilde{y}_f(N-1,1,1) \\ \vdots & \vdots & \cdots & \\ \tilde{y}_f(0,1,Q) & \tilde{y}_f(1,1,Q) & \cdots & \tilde{y}_f(N-1,1,Q) \\ \vdots & \vdots & \cdots & \vdots \\ \tilde{y}_f(0,K,Q) & \tilde{y}_f(1,K,Q) & \cdots & \tilde{y}_f(N-1,K,Q) \end{bmatrix}, \tag{A.4b}$$

The matrices in Eq. A.4 can be further expanded as follows

$$\hat{\mathbf{Y}}_f = \begin{bmatrix} y_f(0) & y_f(1) & \cdots & y_f(N-1) \\ y_f(-1) & y_f(0) & \cdots & y_f(N-2) \\ \vdots & \vdots & \cdots & \\ y_f(-Q) & y_f(1-Q) & \cdots & y_f(N-1-Q) \\ \vdots & \vdots & \cdots & \vdots \\ y_f(-Q)\,|y_f(-Q)|^2 & y_f(1-Q)\,|y_f(1-Q)|^2 & \cdots & y_f(N-1-Q)\,|y_f(N-1-Q)|^2 \\ \vdots & \vdots & \cdots & \vdots \\ y_f(-Q)\,|y_f(-Q)|^{K-1} & y_f(1-Q)\,|y_f(1-Q)|^{K-1} & \cdots & y_f(N-1-Q)\,|y_f(N-1-Q)|^{K-1} \end{bmatrix}, \tag{A.5}$$

$$\tilde{\mathbf{Y}}_f = \begin{bmatrix} \tilde{y}_f(0) & \tilde{y}_f(1) & \cdots & \tilde{y}_f(N-1) \\ \tilde{y}_f(-1) & \tilde{y}_f(0) & \cdots & \tilde{y}_f(N-2) \\ \vdots & \vdots & \cdots & \\ \tilde{y}_f(-Q) & \tilde{y}_f(1-Q) & \cdots & \tilde{y}_f(N-1-Q) \\ \vdots & \vdots & \cdots & \vdots \\ \tilde{y}_f(-Q)\,|\tilde{y}_f(-Q)|^2 & \tilde{y}_f(1-Q)\,|\tilde{y}_f(1-Q)|^2 & \cdots & \tilde{y}_f(N-1-Q)\,|\tilde{y}_f(N-1-Q)|^2 \\ \vdots & \vdots & \cdots & \vdots \\ \tilde{y}_f(-Q)\,|\tilde{y}_f(-Q)|^{K-1} & \tilde{y}_f(1-Q)\,|\tilde{y}_f(1-Q)|^{K-1} & \cdots & \tilde{y}_f(N-1-Q)\,|\tilde{y}_f(N-1-Q)|^{K-1} \end{bmatrix}, \tag{A.6}$$

where $y_f(n)$ is the actual measured signal in the feedback path and $\tilde{y}_f(n) \forall\ n = 0 \cdots N-1$ is defined in Eq. 3.14b.

Bibliography

[1] B. G. Evans, "The role of satellites in 5g," in *2014 7th Advanced Satellite Multimedia Systems Conference and the 13th Signal Processing for Space Communications Workshop (ASMS/SPSC)*, 2014, pp. 197–202.

[2] O. Kodheli, A. Guidotti, and A. Vanelli-Coralli, "Integration of satellites in 5g through leo constellations," in *GLOBECOM 2017 - 2017 IEEE Global Communications Conference*, 2017, pp. 1–6.

[3] G. Giambene, S. Kota, and P. Pillai, "Satellite-5g integration: A network perspective," *IEEE Network*, vol. 32, no. 5, pp. 25–31, 2018.

[4] joint consortium 5G-PPP, "5g: challenges, research priorities, and recommendations," Tech. Rep., sep 2014.

[5] A. Kyrgiazos, B. Evans, P. Thompson, P. Mathiopoulos, and S. Papaharalabos, "A terabit/second satellite system for european broadband access: a feasibility study," *International Journal of Satellite Communications and Networking*, 2014. [Online]. Available: http://epubs.surrey.ac.uk/838158/

[6] G. Maral and M. Bousquet, *Satellite communications systems : systems, techniques and technology*, 5th ed. Wiley India, 2014.

[7] P. Angeletti, R. De Gaudenzi, and M. Lisi, "From "bent pipes" to "software defined payloads": evolution and trends of satellite communications systems," 06 2008, pp. 1–10.

[8] G. Maral, *VSAT Networks*. USA: John Wiley and Sons, Inc., 2003.

[9] D. Roddy, *Satellite Communications, Fourth Edition*, ser. Professional Engineering. McGraw-Hill Education, 2006. [Online]. Available: https://books.google.de/books?id=HGrf8B_uiVMC

[10] G. E. Corazza, *Digital Satellite Communication*. Springer, 2007.

[11] L. Ding, G. T. Zhou, D. R. Morgan, Z. Ma, J. S. Kenney, J. Kim, and C. R. Giardina, "A robust digital baseband predistorter constructed using memory polynomials," *IEEE Transactions on Communications*, vol. 52, no. 1, pp. 159–165, Jan 2004.

[12] Y. Liu, W. Pan, S. Shao, and Y. Tang, "A general digital predistortion architecture using constrained feedback bandwidth for wideband power amplifiers," *IEEE Transactions on Microwave Theory and Techniques*, vol. 63, no. 5, pp. 1544–1555, May 2015.

[13] C. Cripps, *RF power amplifers for wireless communications*. Norwood: MA: Artech House, 1999.

[14] S. Pupolin and L. Greenstein, "Performance analysis of digital radio links with nonlinear transmit amplifiers," *IEEE Journal on Selected Areas in Communications*, vol. 5, no. 3, pp. 534–546, Apr 1987.

[15] C. Yu, L. Guan, and A. Zhu, "Band-limited Volterra series-based behavioral modeling of RF power amplifiers," in *2012 IEEE/MTT-S International Microwave Symposium Digest*, June 2012, pp. 1–3.

[16] S. Lim and C. Eun, "Predistorter design for a memory-less nonlinear high power amplifier using the pth-order inverse method for OFDM systems," in *2005 International Symposium on Intelligent Signal Processing and Communication Systems*, Dec 2005, pp. 217–220.

[17] N. Kelly, M. Allegue-Martínez, P.-D. M. Arapoglou, and A. Zhu, "Bandwidth-constrained digital pre-compensation technique for multi-carrier satellite com-

munications," *Int. J. Satellite Communications Networking*, vol. 34, pp. 171–194, 2016.

[18] H. Fenech, A. Tomatis, S. Amos, V. Soumpholphakdy, and D. Serrano-Velarde, "Future high throughput satellite systems," in *2012 IEEE First AESS European Conference on Satellite Telecommunications (ESTEL)*, 2012, pp. 1–7.

[19] H. Fenech, S. Amos, A. Tomatis, and V. Soumpholphakdy, "High throughput satellite systems: An analytical approach," *IEEE Transactions on Aerospace and Electronic Systems*, vol. 51, no. 1, pp. 192–202, 2015.

[20] A. A. M. Saleh, "Intermodulation analysis of FDMA satellite systems employing compensated and uncompensated TWT's," *IEEE Transactions on Communications*, vol. 30, no. 5, pp. 1233–1242, May 1982.

[21] M. Aloisio, E. Casini, and A. Ginesi, "Evolution of space traveling-wave tube amplifier requirements and specifications for modern communication satellites," *IEEE Transactions on Electron Devices*, vol. 54, no. 7, pp. 1587–1596, July 2007.

[22] A. Katz, J. Wood, and D. Chokola, "The evolution of pa linearization: From classic feedforward and feedback through analog and digital predistortion," *IEEE Microwave Magazine*, vol. 17, no. 2, pp. 32–40, 2016.

[23] D. Zhou and V. E. DeBrunner, "Novel adaptive nonlinear predistorters based on the direct learning algorithm," *IEEE Transactions on Signal Processing*, vol. 55, no. 1, pp. 120–133, Jan 2007.

[24] J. Wood, "Digital pre-distortion of rf power amplifiers," in *2017 IEEE Topical Conference on RF/Microwave Power Amplifiers for Radio and Wireless Applications (PAWR)*, 2017, pp. 1–3.

[25] B. F. Beidas, R. I. Seshadri, and N. Becker, "Multicarrier successive predistortion for nonlinear satellite systems," *IEEE Transactions on Communications*, vol. 63, no. 4, pp. 1373–1382, April 2015.

[26] B. F. Beidas, "Adaptive digital signal predistortion for nonlinear communication systems using successive methods," *IEEE Transactions on Communications*, vol. 64, no. 5, pp. 2166–2175, May 2016.

[27] B. F. Beidas, H. El Gamal, and S. Kay, "Iterative interference cancellation for high spectral efficiency satellite communications," *IEEE Transactions on Communications*, vol. 50, no. 1, pp. 31–36, Jan 2002.

[28] B. F. Beidas, "Intermodulation distortion in multicarrier satellite systems: Analysis and turbo volterra equalization," *IEEE Transactions on Communications*, vol. 59, no. 6, pp. 1580–1590, June 2011.

[29] X. Maufroid, F. Coromina, B.-M. Folio, H. G. Goeckler, H. Kopmann, and M. N. Abdulazim, "High throughput bent-pipe processor for future broadband satellite access networks," European Space Agency ; Digital Signal Processing: Group Ruhr-Universitaet Bochum, Germany, Tech. Rep., 2011.

[30] O. Usman, G. Staude, and A. Knopp, "Onboard compensation of linear and non-linear hardware imperfections in multiport amplifiers," 12 2018, pp. 1–6.

[31] J. Liu and V. Mukundagiri, "Study of ADC resolution and bandwidth requirement tradeoffs for high-speed data communications," in *2013 IEEE 56th International Midwest Symposium on Circuits and Systems (MWSCAS)*, Aug 2013, pp. 864–867.

[32] G. Su, W. Chen, S. Zhang, and F. M. Ghannouchi, "A robust and low sampling rate digital predistortion algorithm for broadband PA modeling and predistortion," in *WAMICON 2014*, June 2014, pp. 1–4.

[33] G. Karam and H. Sari, "A data predistortion technique with memory for QAM radio systems," *IEEE Transactions on Communications*, vol. 39, no. 2, pp. 336–344, Feb 1991.

[34] A. Molina, K. Rajamani, and K. Azadet, "Digital predistortion using lookup tables with linear interpolation and extrapolation: Direct least squares coeffi-

cient adaptation," *IEEE Transactions on Microwave Theory and Techniques*, vol. 65, no. 3, pp. 980–987, March 2017.

[35] N. Naskas and Y. Papananos, "Neural-network-based adaptive baseband predistortion method for RF power amplifiers," *IEEE Transactions on Circuits and Systems II: Express Briefs*, vol. 51, no. 11, pp. 619–623, Nov 2004.

[36] M. Rawat, K. Rawat, and F. M. Ghannouchi, "Adaptive digital predistortion of wireless power amplifiers/transmitters using dynamic real-valued focused time-delay line neural networks," *IEEE Transactions on Microwave Theory and Techniques*, vol. 58, no. 1, pp. 95–104, Jan 2010.

[37] R. Hongyo, Y. Egashira, T. M. Hone, and K. Yamaguchi, "Deep neural network-based digital predistorter for doherty power amplifiers," *IEEE Microwave and Wireless Components Letters*, vol. 29, no. 2, pp. 146–148, Feb 2019.

[38] M. Schetzen, "Theory of pth-order inverses of nonlinear systems," *IEEE Transactions on Circuits and Systems*, vol. 23, no. 5, pp. 285–291, May 1976.

[39] E. Biglieri, S. Barberis, and M. Catena, "Analysis and compensation of nonlinearities in digital transmission systems," *IEEE Journal on Selected Areas in Communications*, vol. 6, no. 1, pp. 42–51, Jan 1988.

[40] Sunmin Lim and Changsoo Eun, "Predistorter design for a memory-less nonlinear high power amplifier using the pth-order inverse method for OFDM systems," in *2005 International Symposium on Intelligent Signal Processing and Communication Systems*, Dec 2005, pp. 217–220.

[41] S. Dimitrov, "Non-linear distortion cancellation and symbol-based equalization in satellite forward links," *IEEE Transactions on Wireless Communications*, vol. 16, no. 7, pp. 4489–4502, July 2017.

[42] M. O'Droma, E. Bertran, M. Gadringer, S. Donati, A. Zhu, P. L. Gilabert, and J. Portilla, "Developments in predistortion and feedforward adaptive power

amplifier linearisers," in *European Gallium Arsenide and Other Semiconductor Application Symposium, GAAS 2005*, 2005, pp. 337–340.

[43] Changsoo Eun and E. J. Powers, "A new volterra predistorter based on the indirect learning architecture," *IEEE Transactions on Signal Processing*, vol. 45, no. 1, pp. 223–227, Jan 1997.

[44] Y. Liu, J. J. Yan, H. T. Dabag, and P. M. Asbeck, "Novel technique for wideband digital predistortion of power amplifiers with an under-Sampling ADC," *IEEE Transactions on Microwave Theory and Techniques*, vol. 62, no. 11, pp. 2604–2617, Nov 2014.

[45] H. Fenech, L. Roux, A. Hirsch, and V. Soumpholphakdy, "Satellite antennas and digital payloads for future communication satellites: The quest for efficiencies and greater flexibility," *IEEE Antennas and Propagation Magazine*, vol. 61, no. 5, pp. 20–28, 2019.

[46] S. D. Marinella Aloisio, Piero Angeletti, "Accurate modeling and analysis of isolation performance in multiport amplifiers," *Active and Passive Electronic Components*, 2012.

[47] S. Egami and M. Kawai, "An adaptive multiple beam system concept," *IEEE Journal on Selected Areas in Communications*, vol. 5, no. 4, pp. 630–636, May 1987.

[48] A. Mallet, A. Anakabe, J. Sombrin, and R. Rodriguez, "Multiport-amplifier-based architecture versus classical architecture for space telecommunication payloads," *IEEE Transactions on Microwave Theory and Techniques*, vol. 54, no. 12, pp. 4353–4361, Dec 2006.

[49] M.-Q. Lee, H. Lim Lee, and J. Won Yu, "Reconfigurable 4x4 multi-port amplifier with switchable input and output matrices," vol. 10, 05 2016.

[50] M. Tanaka and S. Egami, "Reconfigurable multiport amplifiers for in-orbit use," *IEEE Transactions on Aerospace and Electronic Systems*, vol. 42, pp. 228–236, 2006.

[51] Xiaodong Li and L. J. Cimini, "Effects of clipping and filtering on the performance of ofdm," *IEEE Communications Letters*, vol. 2, no. 5, pp. 131–133, May 1998.

[52] R. Piazza, B. S. M. R., and B. Ottersten, "Generalized direct predistortion with adaptive crest factor reduction control," in *2015 IEEE International Conference on Acoustics, Speech and Signal Processing (ICASSP)*, April 2015, pp. 3242–3246.

[53] R. Salmeh, "A novel high gain and low noise figure cmos mixer with fully integrated ESD protection," in *2012 IEEE 55th International Midwest Symposium on Circuits and Systems (MWSCAS)*, Aug 2012, pp. 41–44.

[54] A. Azizan, S. A. Z. Murad, R. C. Ismail, and M. N. M. Yasin, "A review of LNA topologies for wireless applications," in *2014 2nd International Conference on Electronic Design (ICED)*, Aug 2014, pp. 320–324.

[55] D. K. Linkhart, *Microwave Circulator Design*, 2nd ed. Artech House, 2014.

[56] R. W. Daniels, "Approximation methods for electronic filter design; with applications to passive, active, and digital networks," pp. xvii, 388p. [Online]. Available: http://caltech.tind.io/record/495610

[57] E. T. S. Institute, "Digital video broadcasting (dvb); second generation framing structure, channel coding and modulation systems for broadcasting, interactive services, news gathering and other broadband satellite applications. technical report part ii: S2-extensions (dvb-s2x)," Tech. Rep., 2014.

[58] ——, "Digital video broadcasting (dvb); implementation guidelines for the second generation system for broadcasting, interactive services, news gathering

and other broadband satellite applications; part 2: S2 extensions (dvb-s2x)," Tech. Rep., 2015.

[59] ITU, *Handbook on Satellite Communications (HSC)*, 3rd ed. Wiley-Intersceince, 2002.

[60] L. Rockett, D. Patel, S. Danziger, B. Cronquist, and J. J. Wang, "Radiation hardened fpga technology for space applications," in *2007 IEEE Aerospace Conference*, March 2007, pp. 1–7.

[61] Xilinx. (2015) Radiation-hardened, space-grade virtex-5qv family data sheet: Overview. [Online]. Available: https://www.xilinx.com/support/documentation/data_sheets/ds192_V5QV_Device_Overview.pdf

[62] Xilinx. (2020) 7 series fpgas data sheet: Overview. [Online]. Available: https://www.xilinx.com/support/documentation/data_sheets/ds180_7Series_Overview.pdf

[63] B. R. Elbert, *Satellite Communication Applications Handbook*, 2nd ed. Artech House, 2004.

[64] C. Shannon, "Communication in the presence of noise," *Proceedings of the IRE*, vol. 37, no. 1, pp. 10–21, jan 1949. [Online]. Available: https://doi.org/10.1109/jrproc.1949.232969

[65] C. Cripps, *RF power amplifers for wireless communications*. Artech House, 1999.

[66] B. R. Elbert, *The Satellite Communication Ground Segment and Earth Station Handbook*. Artech House, 2001.

[67] Li Zhuoming, "A high performance automatic level control circuit design," in *Proceedings 2013 International Conference on Mechatronic Sciences, Electric Engineering and Computer (MEC)*, Dec 2013, pp. 654–657.

[68] J. Vuolevi and T. Rahkonen, *Distortion in RF Power Amplifiers*. Artech House, 2003.

[69] P. Kenington, *High-Linearity RF Amplifier Design*. Artech House, 2000.

[70] D. Agahi, W. Domino, and N. Vakilian, "Two-tone vs. single-tone measurement of second-order nonlinearity," *Microwave Journal*, vol. 45, pp. 82–94, 03 2002.

[71] A. A. M. Saleh, "Frequency-independent and frequency-dependent nonlinear models of TWT amplifiers," *IEEE Transactions on Communications*, vol. 29, no. 11, pp. 1715–1720, November 1981.

[72] E. Costa, M. Midrio, and S. Pupolin, "Impact of amplifier nonlinearities on ofdm transmission system performance," *IEEE Communications Letters*, vol. 3, no. 2, pp. 37–39, February 1999.

[73] E. Aschbacher and M. Rupp, "Modelling and identification of a nonlinear power-amplifier with memory for nonlinear digital adaptive pre-distortion," in *2003 4th IEEE Workshop on Signal Processing Advances in Wireless Communications - SPAWC 2003 (IEEE Cat. No.03EX689)*, June 2003, pp. 658–662.

[74] D. Dardari, V. Tralli, and A. Vaccari, "A theoretical characterization of nonlinear distortion effects in OFDM systems," *IEEE Transactions on Communications*, vol. 48, no. 10, pp. 1755–1764, Oct 2000.

[75] A. Ghorbani and M. Sheikhan, "The effect of solid state power amplifiers (SSPAs) nonlinearities on mpsk and m-qam signal transmission," in *1991 Sixth International Conference on Digital Processing of Signals in Communications*, Sep. 1991, pp. 193–197.

[76] M. J. Cañavate Sánchez, A. Segneri, A. Georgiadis, S. Kosmopoulos, G. Goussetis, and Y. Ding, "System performance evaluation of power amplifier behavioural models," 04 2018.

[77] G. P. White, A. G. Burr, and T. Javornik, "Modelling of nonlinear distortion in broadband fixed wireless access systems," *Electronics Letters*, vol. 39, no. 8, pp. 686–687, April 2003.

[78] J. C. Pedro and S. A. Maas, "A comparative overview of microwave and wireless power-amplifier behavioral modeling approaches," *IEEE Transactions on Microwave Theory and Techniques*, vol. 53, no. 4, pp. 1150–1163, April 2005.

[79] M. Isaksson, D. Wisell, and D. Ronnow, "A comparative analysis of behavioral models for rf power amplifiers," *IEEE Transactions on Microwave Theory and Techniques*, vol. 54, no. 1, pp. 348–359, Jan 2006.

[80] J. P. Martins, P. M. Cabral, N. Borges Carvalho, and J. C. Pedro, "A metric for the quantification of memory effects in power amplifiers," *IEEE Transactions on Microwave Theory and Techniques*, vol. 54, no. 12, pp. 4432–4439, Dec 2006.

[81] X. YU, "Contributions to digital predistortion of radio-frequency power amplifiers for wireless applications," Ph.D. dissertation, Universität Erlangen-Nürnberg, 2012.

[82] R. E. Santos, N. B. Carvalho, and K. Gard, "The impact of long term memory effects in wireless QPSK modulated signals," in *2007 IEEE/MTT-S International Microwave Symposium*, June 2007, pp. 961–964.

[83] S. Benedetti, E. Biglieri, and V. Castellani, *Digital Transmission Theory*. Prentice-Hall , INC., 1987.

[84] A. Zhu, J. Pedro, and T. Brazil, "Dynamic deviation reduction-based volterra behavioral modeling of RF power amplifiers," *Microwave Theory and Techniques, IEEE Transactions on*, vol. 54, pp. 4323 – 4332, 01 2007.

[85] D. R. Morgan, Z. Ma, J. Kim, M. G. Zierdt, and J. Pastalan, "A generalized memory polynomial model for digital predistortion of RF power amplifiers," *IEEE Transactions on Signal Processing*, vol. 54, no. 10, pp. 3852–3860, Oct 2006.

[86] P. Angeletti and M. Lisi, "A survey of multiport power amplifiers applications for flexible satellite antennas and payloads," 01 2008.

[87] C. Chang, R. Lee, and T. Shih, "Design of a beam switching/steering butler matrix for phased array system," *IEEE Transactions on Antennas and Propagation*, vol. 58, no. 2, pp. 367–374, Feb 2010.

[88] H. L. Lee, M. Q. Lee, and J. W. Yu, "Analysis of multi-port amplifier calibration for optimal magnitude and phase error detection," *IET Microwaves, Antennas Propagation*, vol. 10, no. 1, pp. 102–110, 2016.

[89] O. Leulescu and T. Petrescu, "Nonlinear predistortion for dynamic power amplifiers linearization," in *2005 European Microwave Conference*, vol. 3, 2005, pp. 4 pp.–1794.

[90] Yuanming Ding, Lianming Sun, and A. Sano, "Adaptive nonlinearity predistortion schemes with application to OFDM system," in *Proceedings of 2003 IEEE Conference on Control Applications, 2003. CCA 2003.*, vol. 2, 2003, pp. 1130–1135 vol.2.

[91] E. Bertran, P. L. Gilabert, G. Montoro, and J. Berenguer, "Overview of power amplifier linearization based on predistorsion techniques," in *Proceedings of the 8th Conference on Simulation, Modelling and Optimization*, ser. SMO'08. Stevens Point, Wisconsin, USA: World Scientific and Engineering Academy and Society (WSEAS), 2008, p. 309–314.

[92] X. Yu, "Digital predistortion using feedback signal with incomplete spectral information," in *2012 Asia Pacific Microwave Conference Proceedings*, 2012, pp. 950–952.

[93] G. Karam and H. Sari, "Data predistortion techniques using intersymbol interpolation," *IEEE Transactions on Communications*, vol. 38, no. 10, pp. 1716–1723, Oct 1990.

[94] N. Benvenuto, F. Piazza, and A. Uncini, "A neural network approach to data predistortion with memory in digital radio systems," in *Proceedings of ICC '93 - IEEE International Conference on Communications*, vol. 1, 1993, pp. 232–236 vol.1.

[95] Yi Liao, Donglin Su, Yi Wang, and Wenqing Chen, "A design of analog predistortion linearizer for RF power amplifier to reduce IMD," in *2008 8th International Symposium on Antennas, Propagation and EM Theory*, 2008, pp. 1154–1157.

[96] O. B. Usman, G. Staude, and A. Knopp, "Onboard compensation of linear and non-linear hardware imperfections in multiport amplifiers," *2018 IEEE Global Communications Conference (GLOBECOM)*, pp. 1–6, 2018.

[97] Y. Liu, W. Pan, S. Shao, and Y. Tang, "A general digital predistortion architecture using constrained feedback bandwidth for wideband power amplifiers," *IEEE Transactions on Microwave Theory and Techniques*, vol. 63, no. 5, pp. 1544–1555, May 2015.

[98] A. Kaye, D. George, and M. Eric, "Analysis and compensation of bandpass nonlinearities for communications," *IEEE Transactions on Communications*, vol. 20, no. 5, pp. 965–972, 1972.

[99] Feipeng Wang, A. Ojo, D. Kimball, P. Asbeck, and L. Larson, "Envelope tracking power amplifier with pre-distortion linearization for wlan 802.11g," in *2004 IEEE MTT-S International Microwave Symposium Digest (IEEE Cat. No.04CH37535)*, vol. 3, 2004, pp. 1543–1546 Vol.3.

[100] O. B. Usman, T. Delamotte, and A. Knopp, "Low-effort on-Board memoryless predistortion techniques for SATCOM," in *SCC 2017; 11th International ITG Conference on Systems, Communications and Coding*, Feb 2017, pp. 1–6.

[101] E. Zenteno, M. Isaksson, and P. Händel, "Output impedance mismatch effects on the linearity performance of digitally predistorted power amplifiers," *IEEE*

Transactions on Microwave Theory and Techniques, vol. 63, no. 2, pp. 754–765, Feb 2015.

[102] X. Hu, Z. Liu, W. Wang, M. Helaoui, and F. M. Ghannouchi, "Low-feedback sampling rate digital predistortion using deep neural network for wideband wireless transmitters," *IEEE Transactions on Communications*, vol. 68, no. 4, pp. 2621–2633, 2020.

[103] N. Pothecary, *Feedforward Linear Power Amplifiers*, 1st ed. Artech house, 1999.

[104] H. Paaso and A. Mammela, "Comparison of direct learning and indirect learning predistortion architectures," in *2008 IEEE International Symposium on Wireless Communication Systems*, 2008, pp. 309–313.

[105] X. Li, W. Lv, and F. Li, "High order inverse polynomial predistortion for memoryless RF power amplifiers," in *5th IET International Conference on Wireless, Mobile and Multimedia Networks (ICWMMN 2013)*, 2013, pp. 335–338.

[106] R. Raich and G. T. Zhou, "Orthogonal polynomials for complex gaussian processes," *IEEE Transactions on Signal Processing*, vol. 52, no. 10, pp. 2788–2797, Oct 2004.

[107] G. H. Golub and C. F. Van Loan, *Matrix Computations*, 3rd ed. Johns Hopkins, 1996.

[108] J. Abdoli, M. Jia, and J. Ma, "Filtered OFDM: A new waveform for future wireless systems," in *2015 IEEE 16th International Workshop on Signal Processing Advances in Wireless Communications (SPAWC)*, 2015, pp. 66–70.

[109] H. Kim, I. Jung, Y. Park, W. Chung, S. Choi, and D. Hong, "Time spread-windowed OFDM for spectral efficiency improvement," *IEEE Wireless Communications Letters*, vol. PP, pp. 1–1, 03 2018.

[110] B. Farhang-Boroujeny, "Filter bank multicarrier modulation: A waveform candidate for 5g and beyond," *Advances in Electrical Engineering*, vol. 2014, 12 2014.

[111] V. Vakilian, T. Wild, F. Schaich, S. ten Brink, and J. Frigon, "Universal-filtered multi-carrier technique for wireless systems beyond LTE," in *2013 IEEE Globecom Workshops (GC Wkshps)*, 2013, pp. 223–228.

[112] A. Ijaz, L. Zhang, P. Xiao, and R. Tafazolli. Analysis of candidate waveforms for 5g cellular systems, towards 5g wireless networks - a physical layer perspective. [Online]. Available: https://www.intechopen.com/books/towards-5g-wireless-networks-a-physical-layer-perspective/analysis-of-candidate-waveforms-for-5g-cellular-systems

[113] X. Zhang, M. Jia, L. Chen, J. Ma, and J. Qiu, "Filtered-OFDM - enabler for flexible waveform in the 5th generation cellular networks," in *2015 IEEE Global Communications Conference (GLOBECOM)*, Dec 2015, pp. 1–6.

[114] Z. Kollar, L. Varga, and K. Czimer, "Clipping-based iterative PAPR-reduction techniques for FBMC," in *OFDM 2012; 17th International OFDM Workshop 2012 (InOWo'12)*, Aug 2012, pp. 1–7.

[115] M. Chafii, J. Palicot, and R. Gribonval, "Closed-form approximations of the PAPR distribution for multi-carrier modulation systems," in *2014 22nd European Signal Processing Conference (EUSIPCO)*, Sep. 2014, pp. 1920–1924.

[116] R. W. Bauml, R. F. H. Fischer, and J. B. Huber, "Reducing the peak-to-average power ratio of multicarrier modulation by selected mapping," *Electronics Letters*, vol. 32, no. 22, pp. 2056–2057, Oct 1996.

[117] S. H. Muller and J. B. Huber, "Ofdm with reduced peak-to-average power ratio by optimum combination of partial transmit sequences," *Electronics Letters*, vol. 33, no. 5, pp. 368–369, Feb 1997.

[118] C. Tellambura, "Multicarrier transmission peak-to-average power reduction using simple block code," *Electronics Letters*, vol. 34, no. 17, pp. 1646–, Aug 1998.

[119] Seung Hee Han and Jae Hong Lee, "An overview of peak-to-average power ratio reduction techniques for multicarrier transmission," *IEEE Wireless Communications*, vol. 12, no. 2, pp. 56–65, April 2005.

[120] P. P. Ann and R. Jose, "Comparison of PAPR reduction techniques in OFDM systems," in *2016 International Conference on Communication and Electronics Systems (ICCES)*, Oct 2016, pp. 1–5.

[121] O. B. Usman, A. Knopp, and S. Dimitrov, "Onboard papr reduction and digital predistortion for 5g waveforms in high throughput satellites," in *2020 IEEE 3rd 5G World Forum (5GWF)*, 2020, pp. 174–179.

[122] E. Casini, R. D. Gaudenzi, and A. Ginesi, "DVB-S2 modem algorithms design and performance over typical satellite channels," *International Journal of Satellite Communications and Networking*, vol. 22, no. 3, pp. 281–318, 2004. [Online]. Available: https://onlinelibrary.wiley.com/doi/abs/10.1002/sat.791

[123] S. Boumard, M. Lasanen, O. Apilo, A. Hekkala, C. Cassan, J. Verdeil, J. David, and L. Pichon, "Power consumption trade-off between power amplifier OBO, DPD, and clipping and filtering," in *2014 26th International Teletraffic Congress (ITC)*, 2014, pp. 1–5.

[124] P. Kasliwal, B. P. Patil, and D. Gautam, "Performance evaluation of squaring operation by Vedic mathematics," *IETE Journal of Research*, vol. 57, p. 39, 01 2011.

[125] R. K. Barik and M. Pradhan, "Efficient ASIC and FPGA implementation of cube architecture," *IET Computers Digital Techniques*, vol. 11, no. 1, pp. 43–49, 2017.

[126] J. Castillo, A. Castillo Atoche, R. Carrasco-Alvarez, O. Longoria-Gandara, and J. Ortegón-Aguilar, "FPGA-based hardware matrix inversion architecture using hybrid piecewise polynomial approximation systolic cells," *Electronics*, vol. 9, p. 182, 01 2020.

[127] Xilinx. (2020) Radiation tolerant kintex ultrascale xqrku060 fpga data sheet. [Online]. Available: https://www.xilinx.com/support/documentation/data_sheets/ds882-xqr-kintex-ultrascale.pdf